A Computational Study of Post-Infarct Mechanical Effects of Injected Biomaterial into Ischaemic Myocardium

Department of Human Biology

Biomedical Engineering

presented for the degree of

MSc (Med) in Biomedical Engineering

Author: Renee Miller (Student No: MLLREN003)

Supervisor: Assoc. Prof. Thomas Franz

Co-Supervisor: Dr. Neil Davies

Cardiovascular Research Unit, University of Cape Town

September 2012

DECLARATION

I, Renee Miller, hereby declare that the work on which this dissertation is based is my original work (except where acknowledgements indicate otherwise) and that neither the whole work nor any part of it has been, is being, or is to be submitted for another degree in this or any other university. I empower the university to reproduce for the purpose of research either the whole or any portion of the contents in any manner whatsoever.

Signed by candidate

Signature: ……

Date: September 28, 2012

Abstract

Cardiovascular diseases account for one third of all deaths worldwide, more than 33% of which are related to ischaemic heart disease, involving a myocardial infarction (MI). Emerging MI therapies involving biomaterial injections have shown some benefits; the underlying mechanisms of which remain unclear. Computational models offer considerable potential to study the biomechanics of a myocardial infarction and novel therapies.

Geometrical data of a healthy human left ventricle (LV) obtained from magnetic resonance images (MRI) was used to create a finite element (FE) mesh of the LV at the end-systolic time point using Continuity® 6.3 (University of California in San Diego, US). A mesh of 96 hexahedral elements with high order basis functions was employed to adequately describe the geometry of the LV. Simulations of diastolic filling and systolic contraction were performed using a transversely isotropic exponential strain energy function and a model for active stress based on contraction at the cellular level. An anterior apical, transmural MI was modelled in the LV encompassing 16% of the LV wall volume. The infarct was modelled at acute and fibrotic stages of post-infarct LV remodelling by altering the constitutive and active stress models to best describe passive and active behaviour of the ischaemic myocardium at each time point. The geometry of the LV with the fibrotic infarct was adjusted to represent the wall thinning that occurs during LV post-MI remodelling. Hydrogel injection was modelled as layers with material properties differing from those of the surrounding myocardium while accounting for thickening of the LV wall at the injection site. The study design comprised a healthy case and two infarcted cases with and without hydrogel injection.

The end-diastolic volume (EDV) increased in the acute infarct model compared to the healthy case due to the reduced stiffness in the infarct wall. An EDV increase was not observed in the fibrotic infarct model compared to the healthy case. This was partially attributed to the increase in infarct stiffness and partially due to the fact that remodelling-related dilation of the LV was not implemented in the model. Inclusion of hydrogel lowered EDV in both the acute and fibrotic models. The predicted ejection fraction (EF) decreased from 41.2% for the healthy case to 28.5% and 33.0% for the acute and fibrotic infarct models, respectively. Inclusion of hydrogel layers caused an improvement in EF in the acute model only.

Elevated myofibre stress in the remote and border zone (BZ) regions in a post-MI LV undergoing remodelling leads to hypertrophy and eventual heart failure. Therefore, myofibre stresses were compared at both end-diastolic (ED) and end-systolic (ES)

points in the cardiac cycle. The acute infarct, less stiff than healthy myocardium, resulted in lower myofibre stresses in the infarct region at both end-diastole and end-systole. However, remote and BZ myofibre stresses increased. The stiff fibrotic infarct, with a thinned wall, exhibited higher myofibre stresses in the infarct, remote and BZ regions than in the healthy case. Simulated injection of hydrogel reduced overall LV ED myofibre stresses in both the acute and fibrotic infarct cases. At end-systole, the acute and fibrotic infarcts caused an increase in myofibre stress in the BZ and entire LV. Addition of hydrogel layers reduced LV myofibre stress in the acute and fibrotic infarct model. Inclusion of hydrogel lowered ES myofibre stress in the BZ in both infarct models. Thinning of the LV wall leads to excessive distension (or bulging), limiting LV myocardial function. ED and ES strains from the non-treated and treated infarct models were compared with the healthy case to determine whether the inclusion of hydrogel has an impact on infarct stretching. ED strain increased from the healthy to the acute case in the infarct region. There was, however, negligible change in myofibre strain in the remote and BZ regions. The stiff fibrotic infarct caused a decrease in myofibre strain in the infarct region. ES myofibre strain in the healthy model was negative since active myocardium is contracting. However, the infarct regions in the acute and fibrotic models resulted in positive strain values since the ischaemic tissue can no longer contract. The acute infarct exhibited greater strain or distension of the infarct region than the fibrotic infarct. Inclusion of hydrogel lowered ED myofibre strain in each infarct model throughout the entire LV. Similarly, hydrogel layers considerably lowered ES myofibre strain, not only in the infarct region, but throughout the LV.

Addition of the hydrogel into infarcted myocardial tissue does not have a substantial positive effect when only considering the cardiac functional parameters. There is no benefit in contractility of the LV and only a slight improvement in ejection fraction with hydrogel injection at the acute time point. However, the addition of hydrogel shows a clear improvement on myofibre stresses and strains throughout the LV. Hydrogel layers lower myofibre stresses in the infarct and border zone regions at both ED and ES time points, potentially reducing hypertrophy of remote and BZ regions. In addition, hydrogel layers reduce strain or distension of the infarcted and border zone tissue, retaining efficiency of the LV and preventing wall thinning. Therefore, hydrogel injection should be researched further as a possible treatment post-MI as a means of deterring LV remodelling and heart failure.

Contents

List of Figures

List of Tables

Abbreviations

AI	Acute infarct
BG	Bulk gel
CVD	Cardiovascular disease
ED	End-diastolic
EDPVR	End-diastolic pressure volume relationship
EDV	End-diastolic volume
EF	Ejection fraction
ES	End-systolic
ESPVR	End-systolic pressure volume relationship
FE	Finite element
FEA	Finite element analysis
FEM	Finite element method
FI	Fibrotic infarct
HF	Heart failure
LG	Layered gel
LV	Left ventricle
MI	Myocardial infarction
MRI	Magnetic resonance imaging
SV	Stroke volume

1. *Introduction*

1.1. Background

In 2004, there were 17.1 million deaths from cardiovascular diseases (CVD) worldwide, of which 7.2 million were attributed to coronary heart disease. 82% of CVD deaths take place in low- and middle-income countries, including South Africa. Lower- and middle-income countries are affected most due to the lack of preventive healthcare and solutions when catastrophic CVD related events occur (WHO, 2008). CVD is expected to become the leading cause of death worldwide by 2020, superseding infectious diseases such as HIV, TB and Malaria due to a growing epidemic of obesity, diabetes and uncontrolled hypertension (Lloyd-Jones et al., 2010). Currently, CVD account for approximately one third of all deaths in the world. More than 33% of these deaths are related to ischaemic heart disease, involving a myocardial infarction (MI)(AHA, 2008). Consequently, alternative therapies are urgently needed.

In a healthy heart, the left ventricle (LV) expands passively during diastole as oxygenated blood from the lungs enters from the left atrium. During systole, the LV actively contracts, expelling blood through the systemic circulatory system to meet the body's nutrient needs. During an MI, the blockage of a coronary artery restricts oxygen delivery to the cardiac tissue, causing cardiomyocyte death and loss of contractility in the region of the LV supplied by the blocked blood vessel. Immediately after infarction in non-fatal cases, in the acute phase, ischaemic tissue maintains the same passive properties as healthy myocardium throughout passive filling. However, systolic function of active ejection of blood is greatly impaired. While the healthy tissue continues to contract, the ischaemic tissue bulges out, increasing LV volume, absorbing some of the contractile mechanical energy and decreasing the efficiency of the heart. The enlarged LV volume causes an elevation of ventricular wall stress in an attempt to maintain the stroke volume to ensure adequate organ perfusion (Whelan et al., 2007). The healthy myocardium then contracts harder to compensate for the decreased mechanical output, leading to remodelling and hypertrophy of the healthy tissue in later phases. The increased volume and pressure load on healthy tissue can eventually lead to heart failure (HF) (Opie et al., 2006). Even small increases in ventricular wall volume post-MI, indicating hypertrophy and cardiac remodelling, point towards a poor prognosis and eventual HF (Konstam, 2005). Therefore, any innovative treatments or therapies to prevent HF must target harmful ventricular remodelling.

1.2. Problem Identification

Despite advances in therapies for HF, the only definite treatment currently known is heart transplantation which suffers from a chronic shortage of organ donations. After early reperfusion, first line medical treatment usually consists of angiotensin-converting enzyme inhibitors, angiotensin receptor blockers and beta-blockers. The reduction of morbidity and mortality after MI with these treatments has been credited, at least in part, to the attenuation and partial reversal of the remodelling of the injured heart (Pfeffer et al., 1992, Kober et al., 1995, Hall et al., 1995, Cohn and Tognoni, 2001, McMurray et al., 2003).

With the high prevalence of HF, substantial research has been devoted towards developing new treatments with an emphasis on cell delivery post infarction (Fuchs et al., 2001, Mangi et al., 2003, Zisch et al., 2003, Kraehenbuehl et al., 2008). Results have demonstrated an improvement of the LV pump function. It is, however, not well understood whether this beneficial effect has been a result of cellular signalling, mechanics of the increased LV wall thickness (Grossman et al., 1975, Wall et al., 2006) or a combination of the two. Therefore, the potential of biomaterial delivery without stem cells into the ischaemic heart to tackle post-infarct remodelling have begun to be explored. Initial results of biomaterial injection have given reason for cautious optimism: Increased wall thickness (Kofidis et al., 2005, Dai et al., 2005, Landa et al., 2008), attenuation of adverse LV remodelling (Landa et al., 2008), decreased infarct size (Christman et al., 2004) and improvement of functional parameters (Kofidis et al., 2005, Dai et al., 2005, Landa et al., 2008) have all been demonstrated. It has been proposed that a non-degradable injectable polymer may be required for long-term beneficial effects on heart remodelling (Christman and Lee, 2006) while a degradable injectable polymer has been shown to reduce the inflammatory response caused by the injectate (Kadner et al., 2012).

This recent research into biomaterial delivery for treatment of MI and prevention of HF has predominantly been based on pre-clinical small animal models. However, *in vivo* models are associated with challenges such as high costs of the equipment for cardiac physiology assessment, difficulties reproducing favourable results in clinical studies (Patten and Hall-Porter, 2009) and limitations in isolating causative factors. Computational modelling in cardiac biomechanics can provide a meaningful method for obtaining complementary information on mechanical mechanisms involved in a myocardial infarction and improve the understanding of patho-physiological processes involved in MI. Consequently, computational biomechanics has a considerable

potential to contribute to the advancement of therapies for MI and the prevention of heart failure.

1.3. Aim and Objectives

The goal of the research into myocardial infarction currently undertaken at the Cardiovascular Research Unit was to contribute to the understanding and advancement of one emerging therapy for acute MI, the injection of a polymeric biomaterial into the ischaemic myocardium through studying the biomechanical mechanisms associated with this treatment.

Based on past *in vivo* studies investigating the use of injectable biomaterials as a post-MI therapy to prevent the progression towards HF, the hypothesis for the research of this thesis is that a) biomaterial injectates in the infarct region lead to a reduction in wall stress and strain in the infarct region and the functional border zone as well as an increase in ventricular function compared to the infarcted case without injectate, b) layered injectates and bulk injectates show difference in the effects mentioned under (a), and c) the mechanical effects of the biomaterial injectates on ventricular mechanics and function differ between the ischemic and the scarred infarct stage.

The aim of this Master's thesis was to develop computational models, using freely available software, of the injection of a polymeric biomaterial into infarcted myocardium in a human LV and to study the effects of the injectate on myocardial stresses, strains and cardiac function of an infarcted LV.

The objectives of the research were to:

- Model an a) healthy LV, b) infarcted LV at two time points post infarction, and c) infarcted LV at two time points post infarction with injected biomaterial.
- Simulate diastole and systole for each model using linear pressure/volume increase models.
- Analyse resulting stresses, strains, and cardiac parameters such as ejection fraction and contractility to interpret the effect of injected biomaterial on the ischaemic heart.

2. *Theory and Literature Review*

2.1. Anatomy and Physiology of the Heart

2.1.1. Anatomy

The human heart, a myogenic organ, circulates blood throughout the body through repeated, rhythmic contractions. It is located in the chest between the lungs and is encased in the pericardium, a sac that prevents friction between the heart tissue and surrounding organs. It is composed of the right and left atria, which receive blood from the body, and the right and left ventricles (RV and LV, respectively), which pump blood throughout the body, see Figure 2-1. The cardiac muscle is striated and involuntary, completely unique to this organ, and receives its blood supply through coronary arteries.

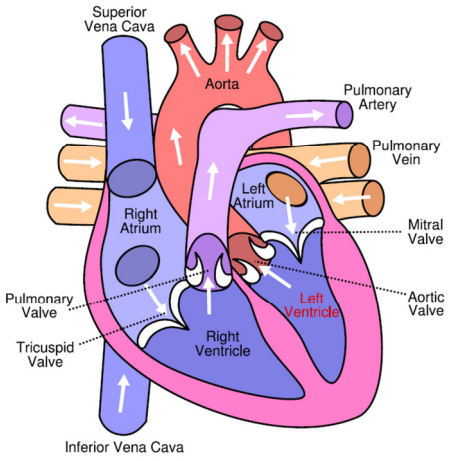

Figure 2-1: Heart diagram outlining the major cavities, arteries, and veins of the heart

The LV approximately resembles a truncated prolate spheroid with the mitral valve at the base (superior end) and apex at the inferior end. Papillary muscles connect the inner surface of the LV wall to the cusps of the mitral valve via the chordae tendinae and contract to prevent inversion of the valve. The LV wall is composed of three layers: endocardium (inner layer), myocardium (middle layer), and epicardium (outer layer); the myocardium itself consists of sheets of cardiomyocytes (70% of volume) and interstitial components (30% of volume).

Passive and active LV biomechanics are inherently dependent on the myocardial fibre orientation since myofibres contract and stretch along the fibre direction. Viewed from the apex, the fibres wrap the LV in a helical pattern and vary approximately linearly from epicardium (right handed helix) to endocardium (left handed helix). Although

assumed in literature, the fibres are generally not parallel to the LV wall (Holzapfel and Ogden, 2009). The fibre angle with respect to the LV wall is known as the transverse angle and the angle with respect to the circumferential plane is known as the helical angle. Helical fibre angles vary from approximately +60° to -60° from endocardium to epicardium (Streeter Jr et al., 1969) and transverse angles from -10° to +10° from apex to base. Transverse angles, however, are 0° at the epicardial and endocardial surfaces (Bovendeerd, 2008).

a) b)

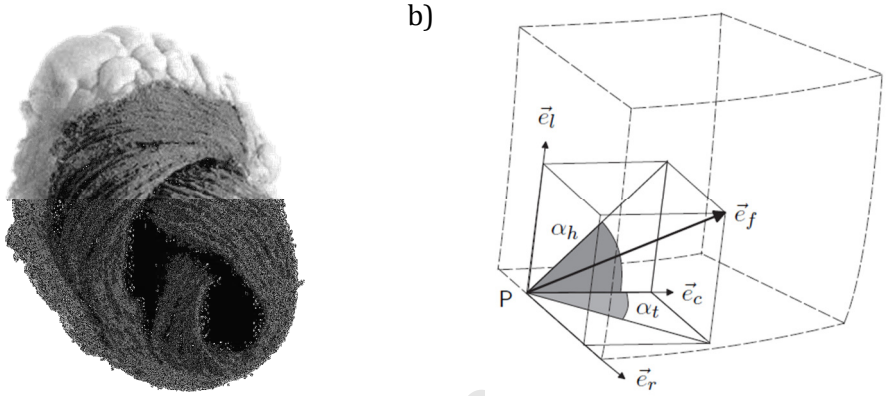

Figure 2-2: a) Blunt dissected LV showing helical myofibres and b) Cross-section of myocardium with helical (α_h) and transverse (α_t) angles depicted (Bovendeerd, 2008)

2.1.2. Physiology

The heart functions as a mechanical pump, circulating blood through the pulmonary and systemic circulatory systems. The average human heart beats 72 times per minute and will beat approximately 2.5 billion times during one's lifetime. Blood flows in through the inferior and superior vena cava and is collected in the right atrium. It then moves through the tricuspid valve into the RV. Blood is ejected from the RV through the pulmonary valve and circulated to the lungs for oxygenation. It returns to the heart passing through the left atrium. During passive filling, the blood enters the LV through the mitral valve. And finally, the blood is pumped out of the LV through the aortic valve where it circulates throughout the body. The LV needs to support a higher pressure than the RV in order to pump the blood throughout the entire body, as opposed to the pulmonary circulation, and is therefore, the largest chamber and has the thickest walls.

Knowledge of the four distinct phases to the LV cardiac cycle is pertinent to effective analysis of the mechanical function to be studied. During isovolumetric contraction, which marks the beginning of systole, the muscle contracts due to ventricular depolarization beginning at the sinoatrial node. The pressure increases while volume within the ventricle remains constant until the LV pressure exceeds aortic pressure and the aortic valve opens. In the second phase, the pressure then remains constant

while blood is expelled from the LV into the aorta during ejection. In the third phase, termed isovolumetric relaxation, pressure decreases and volume remains constant until LV pressure falls below left atrial pressure. Starting at that time point, blood flows from the atrium to the ventricle during filling, i.e. the fourth phase. At the completion of which, the next cardiac cycle begins. The first two phases, isovolumetric contraction and ejection, make up systole while isovolumetric relaxation and filling phases compose diastole (Suga and Sagawa, 1974, Burkhoff et al., 2005).The pressure-volume loop shown in Figure 2-3 outlines the four phases of the LV cycle.

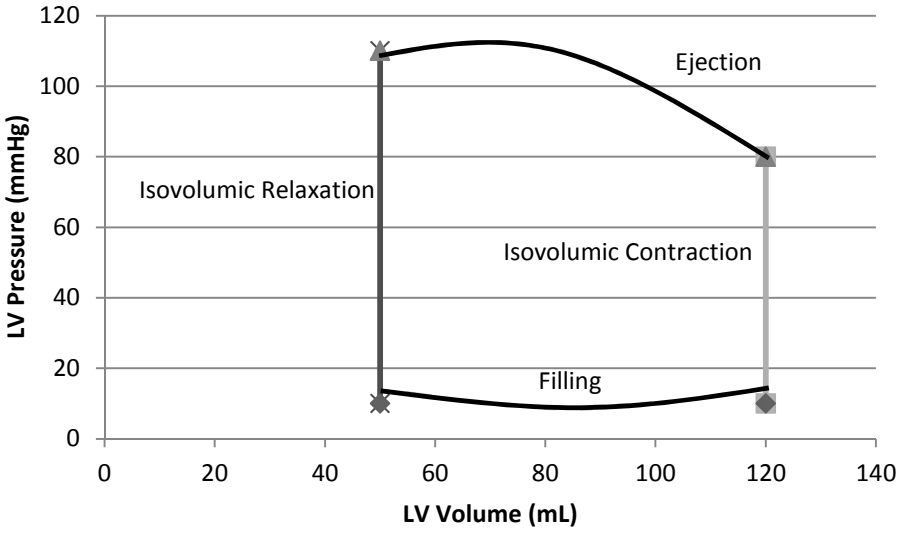

Figure 2-3: LV Pressure-Volume Loop

2.1.3. Cardiac Functional Parameters

Measurable cardiac parameters used in clinical as well as research settings include blood pressure, volume and flow rate, particularly in the four cardiac chambers. LV end-diastolic (ED) and end-systolic (ES) volumes, LV mass, and ejection fraction (EF) are often used to gauge functional cardiac performance on a macro scale. For example, an inflated end-diastolic volume (EDV) can signify LV dilation (Holmes et al., 2005) and a depressed EF can be indicative of increased systolic stress and LV hypertrophy (Nagy, 2001), both present in post-infarction remodelling. EF, see Eq. 2.1, is considered to be one of the most meaningful measures of LV pump function and can be determined from data obtained using non-invasive imaging techniques:

$$EF = \frac{SV}{EDV} = \frac{EDV - ESV}{EDV} \tag{2.1}$$

where SV is stroke volume and ESV is end-systolic volume. Effective arterial elastance (E_a), the ratio of end-systolic pressure (P_{ES}) to stroke volume (SV), expressed as:

$$E_a = \frac{P_{ES}}{SV} \tag{2.2}$$

is a useful method of assessing arterial load and its impact on the LV. In particular, E_a can highlight pulsatile loading due to hypertension or aging (Kelly et al., 1992). The end-diastolic and end-systolic pressure volume relationships (EDPVR and ESPVR, respectively) are visualised by plotting the left ventricular pressure versus volume for the diastolic and systolic phases. The EDPVR describes the passive filling and thus the passive properties of the LV. The slope of the EDPVR at any point is the reciprocal of the ventricular compliance. The ESPVR describes the maximum pressure that can be developed in the LV for any given LV volume. The slope of the ESPVR represents the elastance (E_a), described above.

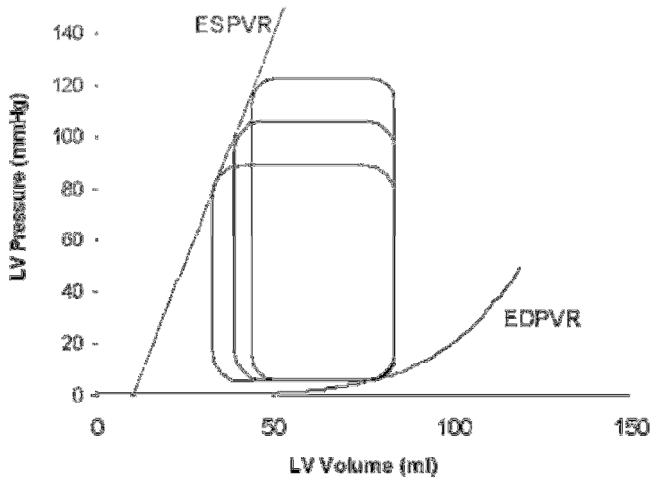

Figure 2-4: Graph of LV pressure versus LV volume showing pressure-volume (PV) loops, end-systolic pressure volume relationship (ESPVR) and end-diastolic pressure volume relationship (Burkhoff et al., 2005)

Fractional shortening (FS), measuring the change in diameter of the LV between the contracted and relaxed states, can provide detailed micro scale information about the contractile abilities of local myocardium. FS is calculated as:

$$FS = \frac{d_{ED} - d_{ES}}{d_{ED}} \tag{2.3}$$

where d_{ED} and d_{ES} are the ED and ES LV diameters, respectively. Patients with LV hypertrophy may exhibit normal cardiac function based on EF-systolic stress relations and macro scale functional parameters, but an abnormal or diminished FS (Aurigemma et al., 1995). Measuring local FS gives a more detailed image of cardiac function in various areas of the heart.

In addition to functional parameters, myocardial mechanics such as wall motion, thickening and strain can provide useful information on the dynamic system of the heart and LV (Frangi, 2001).

2.2. Myocardial Infarction of the Left Ventricle

An MI is caused by restriction of blood supply to a particular region of the myocardium usually caused by plaque build-up in the coronary arteries. Atherosclerosis, thickening and hardening of the arterial walls, is the progressive accumulation of lipids and fibrous elements typically protected by a fibrous cap. Atherosclerotic regions in a coronary artery can grow large enough to restrict blood flow to myocardium. Sudden rupture of the fibrous cap causes platelet aggregation and thrombus formation leading to a rapid occlusion of the artery (Hirai et al., 1989).

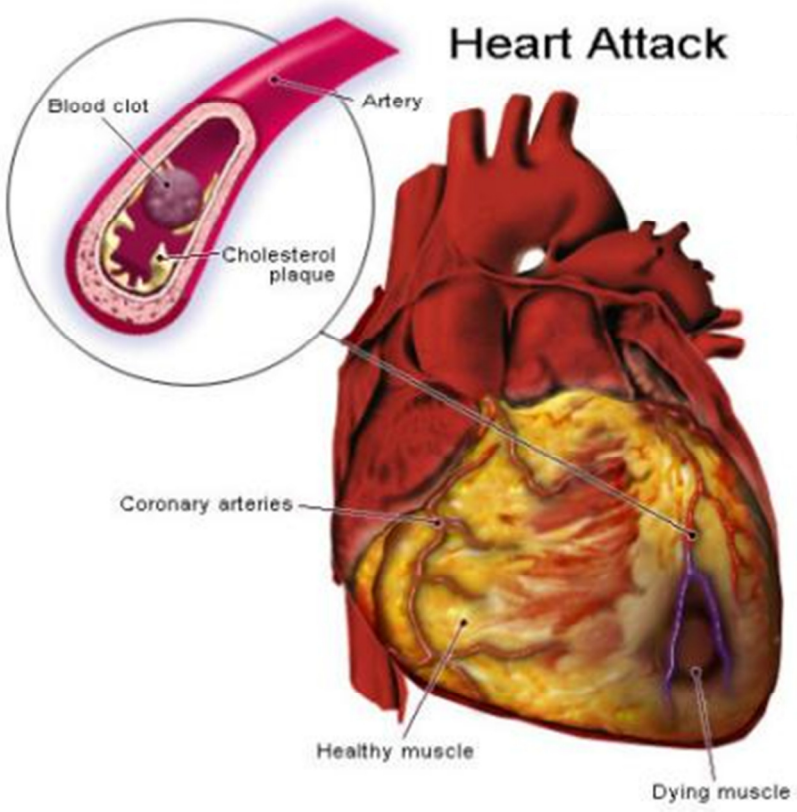

Figure 2-5: Occluded coronary artery causing a myocardial infarction (MedicineNet, 2004)

A blocked coronary artery prohibits the perfusion of oxygen and causes transformation of the myocardium from an active to a passive material. The loss in contractility of the ischaemic myocardium immediately affects the heart's ability to pump an adequate amount of blood to the systemic circulatory system. Consequently, various molecular, cellular and interstitial changes occur in the healthy as well as infarcted myocardium resulting in changes in shape, size and function in an attempt to maintain homeostasis.

There are four primary phases of change after a single, non-reperfused myocardial infarction: 1) acute ischaemia, 2) necrosis, 3) fibrosis and 4) remodelling. Table 2-1 highlights the major ventricular changes that occur during each of the four phases post-infarction (Holmes et al., 2005).

Table 2-1: Four phases of ventricular healing post-infarction (Holmes et al., 2005)

Phase of Healing	**Onset**	**End**	**Time Frame (Humans)**	**Structural Changes**	**Infarct Mechanics**	**Ventricular Function**
Acute Ischaemia	Occlusion of coronary artery	Infarct stiffening	Infarction – hours	Disruption of structural proteins	Passive myocardium	Impaired systolic function
Necrosis	Infarct stiffening	Collagen formation	hours - 7 days (Fishbein et al., 1978)	Edema, necrosis, and degradation	Increased stiffness and strength; infarct expansion	Impaired systolic function
Fibrosis	Collagen formation	Decreased collagen formation	7 - 28 days	Increase in collagen content (scar formation)	Maximum stiffness	Impaired diastolic function
Remodelling	Decreased collagen formation		28 days -	Scar shrinkage and collagen cross-linking	Decrease in stiffness; scar an/isotropy	Improved LV function

In the acute phase post-MI, loss of blood supply causes infarcted myocardium to become passive, losing contractility and impairing systolic function. Necrosis, or cell death, occurs when the infarct begins to stiffen. During this phase, stiffness and strength increase, due to oedema, and the infarct expands. In the third phase post-MI, fibrosis, collagen formation begins to build scar tissue in the infarcted region and the infarct reaches maximum stiffness. At this point, systolic function of the LV is partially restored but diastolic function is impaired due to inhibition of adequate LV filling. And finally, in the remodelling phase, collagen formation decreases (but does not cease), decreasing infarct stiffness and causing scar shrinkage. LV function improves overall during the remodelling phase (Holmes et al., 2005). Despite this fact, ventricular remodelling is accepted to be a critical determinant in the progression towards heart

failure as the infarcted wall becomes thinner and LV dilation continues (Cohn et al., 2000, Pfeffer and Braunwald, 1990).

The effects of infarct mechanical properties on ventricular performance differ not only during each phase of healing but also during systole and diastole: A compliant infarct, during the acute and necrotic phases, impairs systolic ejection. The myocardium stretches during systole thereby dissipating work of the non-infarcted myocardium and reducing the ventricular pump function. Following a MI, LV dilation increases through a positive feedback loop with LV wall stress (Pfeffer and Braunwald, 1990). As stress in the infarct region increases due to dilation, cardiomyocytes lose the ability to shorten effectively, leading to further stretching. Conversely, a stiff infarct region may impair the diastolic filling by reducing the overall ventricular compliance. The complex nature of accommodating systolic as well as diastolic function throughout the phases of remodelling make development of new therapies and treatments a difficult task.

Myocardial infarctions vary drastically from patient to patient and the severity of an MI is often classified according to size – microscopic, small (<10% of the LV wall volume), medium (10 – 30% of the LV wall volume) or large (>30% of the LV wall volume) – as well as location (anterior, lateral, inferior, etc.) (Antman et al., 2000). It is suggested that mortality and morbidity increase drastically when more than 20% of the LV is infarcted (Miura and Miki, 2008).

2.3. Current Post-Infarction Therapies

2.3.1. Pharmaceuticals

Various pharmaceuticals, often the first form of treatment, are administered to patients post-MI include angiotensin-converting enzyme (ACE) inhibitors and beta-adrenergic blockers. ACE inhibitors block the conversion of angiotensin I to angiotensin II, a vasoconstricting agent which also stimulates ventricular remodelling of the heart post-MI among other things. Therefore, ACE inhibitors act as vasodilators, lowering arterial resistance and increasing venous capacity, as well as limit hypertrophy and slow the progression towards HF. In a systematic overview of patient data after administration of ACE inhibitors, Flather et al. (2000) showed that ACE inhibitors reduce the risk of heart failure and recurrent infarctions post-MI.

Beta-blockers reduce the effects of epinephrine and other stress hormones and are administered both as cardioprotection after an MI and as a treatment for hypotension. Beta-blockers reduce mortality in post-MI patients by up to 40% (Gottlieb et al., 1998).

These results are not, however, associated with a reduction in ventricular remodelling or any long-term effects of cardiac mechanics.

Aldosterone receptor antagonists (ARAs) have been proposed as a replacement for ACE inhibitors which lose their effect 8 months after administration. In two studies, ARAs displayed positive results in reducing ventricular hypertrophy as well as reducing morbidity and mortality in patients post-MI (van der Horst et al., 2007, Rocha and Stier, 2001).

As with any drugs, patients can experience adverse reactions such as hypotension, headache, dizziness, fatigue, nausea and renal impairment with all three treatments. In addition, some patients still exhibit signs and symptoms of heart failure after achieving optimal doses of pharmacotherapy.

2.3.2. Mechanical Stabilization

Another alternative for post-infarction therapy is mechanical stabilization of the LV using a heart splint or Acorn cap. The heart splint is designed to decrease LV wall stress by changing LV shape, improving contractile function in dilated hearts, common in post-infarction remodelling. Specifically, the shape is changed by placing three splints perpendicular to the LV long axis, pulling the LV walls inward and creating a symmetric bilobular shape (see Figure 2-6).

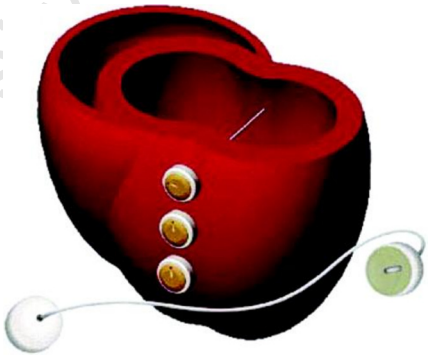

Figure 2-6: LV splint (Large, 2007)

After successful placement of the splints into canine hearts with induced dilated cardiomyopathy, a 30% reduction in ED wall stress and 39% reduction in ES wall stress were observed (Takagaki et al., 2001). Another canine study also showed a significant increase in EF from 19% to 36% acutely and 39% after one month of splint implantation (McCarthy et al., 2001). A second form of mechanical stabilization is the Acorn Cardiac Support Device (Figure 2-7) which fits snugly around both ventricles and is sutured to the atrioventricular groove (Sabbah, 2003). It is designed to reduce ventricular dilation and LV stress. Although a more invasive approach than

pharmaceutical therapy, cardiac support devices directly address the ventricular changes that occur as a result of post-infarction remodelling.

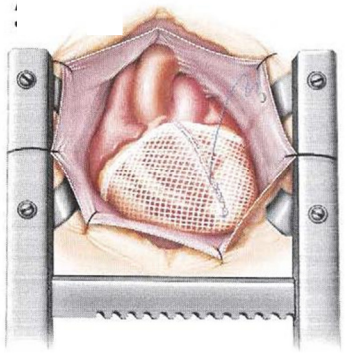

Figure 2-7: Acorn cardiac support device (CorCap)

2.3.3. Cell Therapy

A third therapy option is injection of myoblasts, embryonic progenitor cells that give rise to myocytes, into the infarcted myocardium to promote re-growth of muscle tissue. In a study comparing rats with non-infarcted hearts, infarcted hearts plus sham injection, and infarcted hearts plus skeletal myoblast cell injection, infarctions were induced by one hour coronary ligations followed by reperfusion and cells were injected into the infarct one week following MI. Hearts with cell injections exhibited attenuation of ventricular dilation compared with MI hearts that did not receive cell therapy. Post-MI *in vivo* exercise capacity and *ex vivo* LV systolic pressures improved for the cell injected group (Jain et al., 2001). In a clinical trial, an intracoronary injection with either placebo or bone marrow-derived stem cells was given to patients post-MI. As a result, LV EF increased for patients with cell therapy. In addition, cell infusion reduced infarct size by 28% and aided a better recovery of regional systolic function (Janssens et al., 2006).

In other studies, stem cells were combined with an extracellular matrix including growth factors prior to injection into infarcted mouse hearts. Histological results from Kofidis et al. (2005) showed that the liquid injectable tissue solidified at body temperature, preserving ventricular geometry and function. Despite positive results on LV function, cardiomyocyte differentiation is extremely inefficient and is highly dependent on the microenvironment. Beyond differentiation, cell death and immune rejection remain obstacles to tissue regeneration (Laflamme et al., 2007). Therefore, it is uncertain whether these positive results are due to the injected cells and cellular activity or the supportive mechanical and material properties of carrier medium.

Therefore, recent research, including this study, is aimed at determining the mechanical effect of the injected medium on LV mechanics.

2.3.4. Biomaterial Injectates

Biomaterial injection aimed at preventing heart failure involves incorporating the material completely within the heart wall where it acts as a bulking agent. Materials are delivered through injection into strategic points in and around the infarct. Both biological and synthetic materials have been investigated for post-infarct injection therapy. Biological materials, such as alginate, fibrin, gelatin and collagen, are innately biocompatible and readily accessible to clinicians. Synthetic materials, such as self-assembling peptides and synthetic hydrogels, however, can be designed to meet specific material objectives such as stiffness, porosity and degradation (Nelson et al., 2011).

Positive *in vivo* results have been seen using biological injectates such as alginate, fibrin and gel derived from porcine small intestinal submucosa (SIS). Injecting alginate augmented LV wall thickness resulting in improvement of LV FS and prevention of LV dilation over 5 weeks. Although fibrin injected infarcted hearts displayed a similar initial improvement in cardiac performance and restoration of LV wall thickness, there was deterioration in fractional shortening observed at 10 weeks post infarction. Both alginate and fibrin, however, stimulated neovascularisation in the infarct region (Yu et al., 2009). Injection of SIS gel, commonly used to promote accelerated wound healing, into infarcted mice hearts led to preservation of ES LV geometry and an improvement of cardiac contractility, determined by echocardiography at 2 and 6 weeks (Okada et al., 2010). Research on injection of self-assembling peptides has shown that the fibrous structure encourages host cell infiltration which could be beneficial for myocardial repair post-infarction. However, its immediate effect is a decline in FS (Davis et al., 2005).

Using an *in vivo* MI rat model, researchers in the Cardiovascular Research Unit have studied the effect of injecting a synthetic biomaterial into the ischaemic myocardium. In the initial study, the left anterior descending coronary artery was ligated and non-degradable polyethylene glycol (PEG) hydrogel was immediately injected into the infarcted region. After four weeks, the increase in LV ED diameter normally seen in post-infarction remodelling was drastically reduced (43%, $P < 0.05$) and wall thinning was prevented completely. Therefore, the injection of the hydrogel lessened

pathological remodelling in the immediate post-infarction healing stage (Dobner et al., 2009).

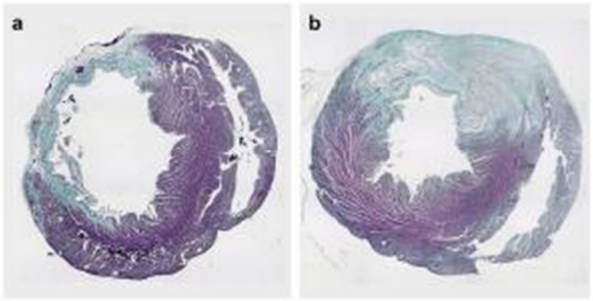

Figure 2-8: Micrograph of Masson's trichrome stained infarct at 4 weeks post-infarction for saline (a) and PEG hydrogel injected heart (b) (Dobner et al., 2009)

A similar study was conducted injecting an enzymatically-degradable PEG hydrogel seven days after infarction, following necrosis of the ischaemic myocardium, in order to compare results to the initial study using non-degradable PEG hydrogel. Results of delayed delivery showed an increase in scar thickness and FS as well as less dilatation of the infarct region during systolic contraction compared with the saline control and immediate injection cases (Kadner et al., 2012).

Although positive results have been observed with numerous biomaterials, a PEG hydrogel is ideally suited for post-infarct injection because its material characteristics such as elasticity, bulk modulus, permeability and degradation rate can be altered relatively easily during the gelation process (Lin and Anseth, 2009). Subsequently, it can be adapted to provide the best structural support for the infarct area during the integral stages of remodelling.

2.4. Cardiac Imaging

Cardiac imaging is essential for diagnosing and monitoring the progression of heart disease post-MI as well as analysing results of various therapies on the heart. Current widely used cardiac imaging modalities include echocardiography, magnetic resonance imaging (MRI) and computed tomography (CT). These imaging techniques are not only used as diagnostic tools but also for qualitative and quantitative analysis of ventricular and cardiac performance. Echocardiography, utilizing traditional ultrasound, is a common form of cardiac imaging. Although a traditional echocardiogram is performed on the surface of the chest, a transesophageal echocardiogram, unobstructed by the ribs and lungs, can provide a more detailed image of the heart. Real-time 3D echocardiography can give an immediate indication of relative cardiac function by measuring ratio between the ventricles in systole and diastole, provide quantitative

information such as LV volume and mass and allow for wall motion analysis (Frangi, 2001). Real-time 3D transesophageal echocardiography can identify various cardiac diseases including mitral stenosis, hypertrophic cardiomyopathy and endocarditis (Pothineni et al., 2007).

MRI, an established form of cardiac imaging, supplies anatomical and functional information about the heart without the use of invasive techniques. Due to the large imaging window and high resolution, its cardiac clinical and research applications are numerous and diverse. In two studies by Heiberg et al., an automated method to quantify myocardial infarction area using MR images was developed. The first utilised contrast enhanced MRI while the latter additionally accounted for partial volume effects (i.e. thinning of the myocardium) (Heiberg et al., 2005a, Heiberg et al., 2008). MRI is also used for cardiac reconstruction which involves segmenting the endo- and epicardial surfaces from short axis slices and reconstructing them in finite element (FE) software.

CT, an imaging technique that compiles a large series of 2D x-ray images, can provide extremely detailed 3D images of myocardium and the vasculature but loses resolution as a patient's heart rate increases due to motion artefacts (Hong et al., 2001). Therefore, it is less commonly used in patients with arrhythmias and fast heart rates. In a study by Ohnesorge et al. (2000), however, electrocardiographically (ECG) gated multi-section spiral scanning CT was used to image patients' hearts with severe fibrillations. In addition, dual-source CT has also been proven to offer a more robust diagnostic image quality over a wide range of heart rates (Johnson et al., 2006). These studies have shown that CT can be a viable modality for cardiac imaging and diagnosis of CVD in patients with irregular heart rhythms.

2.5. Finite Element Method

The mechanics of complex structures and materials often cannot be described using purely analytic methods. In these cases, numerical methods using a computer become useful. Numerical modelling is the process of solving the equations describing a physical process using a step-wise approximation. The equations are designed to represent the inputs, outputs, internal states of the process and the interaction between each. Solutions are obtained by performing iterations at each step until the numerical answer satisfies all the equations being used. Verification is an integral part of numerical modelling since models often use several parameters to describe a

physical process. Previously observed results should be used to verify the accuracy of numerical models and tune the parameters against the observed results.

FE, finite difference, boundary element and finite volume are a few methods of numerical modelling which involve subdividing the physical area of interest into smaller fragments and treating these in a simplified manner. The FE method, used in this thesis, will be described further.

The finite element method (FEM) can be traced back to a paper by Courant (Courant, 1943) and since then, it has become one of the most widely used techniques in computational biomechanics. It has greater geometrical flexibility than other numerical methods. Solid mechanics problems generally take the form of systems of partial differential equations (PDE) defined in terms of the spatial coordinates and time. FEM is useful for solving PDEs in cases involving complex geometries, boundary conditions, nonlinear material behaviour and contact. A solution is found by either eliminating the differential equation completely (steady state problems) or rendering the PDEs into an approximation system of ordinary differential equations (ODE) which are then numerically integrated using standard techniques such as Euler's method.

One defining feature of FEM is the discretisation of continuum problems into a mesh of simpler shapes, such as rods for 1D problems, triangles and quadrilaterals for 2D problems and tetrahedrals and hexahedrals for 3D problems. The vertices and specified points of the elements are known as nodes. Another key feature of FEM is that all governing equations are represented in integral form. The integral over the entire domain is equal to the sum of the integral over each subdomain. Therefore, the FEM provides a means for solving and assembling a numerical problem.

The FEM typically involves the following steps (Usyk, 2002):

1. Formulate the weighted residual
2. Integrate by parts or use the Green-Gauss theorem for vector or tensor variables
3. Discretise the problem into elements and the dependent variables using finite expansions of basis functions
4. Derive the FE equations by substituting the dependent variable approximation in the weighted residual integral
5. Compute the element stiffness matrices and load vectors by integrating the equations over each subdomain

6. Assemble the global stiffness matrix and load vector by adding element matrices and load vectors into a global system of equations
7. Apply essential boundary conditions eliminating the rows and columns corresponding to constrained nodal degrees of freedom from the global stiffness matrix to achieve the constrain-reduced global stiffness matrix
8. Solve the global equations for unknown nodal dependent variables using standard algorithms
9. Evaluate element solutions by interpolating dependent variables and computing their derivatives
10. Visualise and post-process the solution graphically
11. Test for convergence, refine the FE mesh and repeat solution

In the general case, a function u satisfies a set of PDE's:

$$A(u) = \begin{Bmatrix} A_1(u) \\ A_2(u) \\ \vdots \end{Bmatrix} = 0 \tag{2.4}$$

Over a domain Ω, subject to appropriate boundary conditions:

$$B(u) = \begin{Bmatrix} B_1(u) \\ B_2(u) \\ \vdots \end{Bmatrix} = 0 \tag{2.5}$$

The FEM approximates the solution $\hat{u}$ in the form:

$$u \simeq \hat{u} = \sum_{1}^{r} \psi_i a_i \tag{2.6}$$

Where ψ_i are basis functions prescribed in terms of independent variables such as spatial coordinates. Some of the parameters a_i are unknown. The FE solution is approximated inside the elements by shape functions which can take on a number of forms, including polynomial expressions such as $u(x) = a + bx + cx^2 + dx^3 + \cdots$where a, b, c, d, ... are estimated to obtain a best approximation of the field variable $u(x)$.

Figure 2-9 illustrates the way a piecewise linear interpolation can approximate an exact continuous solution. Continuity of field variables is usually enforced across neighbouring elements and the accuracy of a solution increases with higher order basis functions.

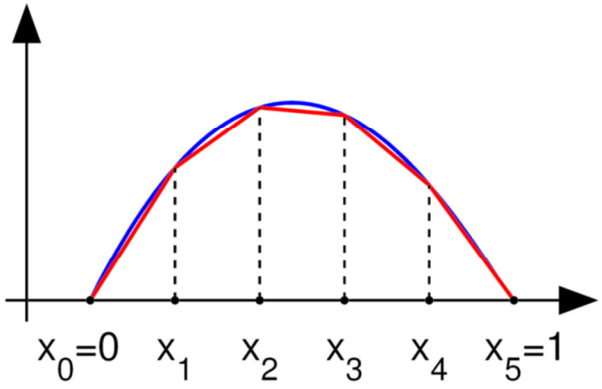

Figure 2-9: Piecewise approximation of a function

Lagrange and Hermite basis functions were both used in the modelling for this thesis. The eight three-dimensional trilinear Lagrange basis functions are constructed from the products of the one-dimensional linear function and correspond to the eight nodes of a trilinear brick element (Figure 2-10). A three-dimensional tricubic Hermite element requires eight derivatives per node, resulting in a large number of basis functions. Although computationally simpler, Lagrange basis functions only provide C^0 continuity of u across element boundaries. Therefore, to preserve continuity of the derivative of u as well, Hermite basis functions are necessary.

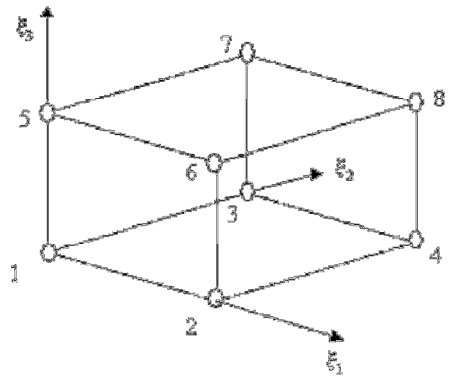

Figure 2-10: 8-noded three-dimensional isoparametric (trilinear brick) finite element

The discretisation of a domain results in a patchwork of elements that interconnect to form the geometry. Selection of element type and number of nodes depends on the complexity of the geometry. The number of elements in the mesh and their size depend on the degree of spatial variation of the field variable in the problem. If large variations are expected, a greater number of small elements should be used to approximate the field variable. In addition, a more refined mesh with more elements can increase the accuracy of the final solution. As the number of nodes and elements increases, results typically converge to the true solution of the problem. However, meshes with a greater

number of nodes and elements are computationally expensive and often not feasible. Therefore, the amount of refinement depends on the computational resources and the acceptable level of numerical accuracy.

2.6. Computational and Numerical Modelling of the Heart

Cardiac modelling can be a purely solid mechanics problem using FEM while some more complex models involve modelling the fluid structure interaction (FSI) between the blood flow and heart walls. FSI combines finite volume methods, often referred to as computational fluid dynamics (CFD) and FEM to investigate the mutual mechanical effects between the heart and blood. For this thesis, the LV was modelled using solid mechanics only and not FSI.

Modelling LV mechanics has four major components: ventricular geometry and structure; pressure and displacement boundary conditions; partial differential equations governing the conservation of mass, momentum and energy; and the constitutive laws that describe mechanical responses of resting and contracting myocardium.

2.6.1. Cardiac Modelling Software

There are many software packages available with capabilities for cardiac modelling. *Abaqus FEA* (D S Simulia. ©DassaultSystemes, Providence, USA, 2007) is a suite of software applications which has four core uses: computer-aided engineering, CFD, nonlinear transient dynamic and quasi-static analysis and general-purpose finite element analysis (FEA). *Abaqus* has been used in a number of studies involving cardiac mechanics. For example, Ratcliffe et al. (1998) researched the effect of ventricular volume reduction surgery in a dilated LV using *Abaqus*'s nonlinear finite element solver to determine deformations in myocardium and ventricular volumes. One limitation is that Abaqus, at present, does not allow for electromechanical coupling necessary for cardiac modelling without the implementation of user-defined subroutines.

FEBio (University of Utah, Salt Lake City, Utah, 2010), an open-source nonlinear FE solver specifically designed for biomechanical applications, offers modelling scenarios, constitutive models and boundary conditions that are relevant to many research areas in biomechanics. Its primary application since development is in the area of musculoskeletal research. However, it has shown promise for application to cardiac FEA since it has the capability of modelling active muscle contraction. In addition, it has porous material models to accurately describe soft tissues such as myocardium. The

only past application of *FEBio* within cardiac mechanics was its use in proving the accuracy of a fast porous visco-hyperelastic soft tissue model (Marchesseau et al., 2010).

Continuity (UCSD, San Diego, California, 2010), a FE software freely available, was developed at the University of California San Diego specifically for the application to cardiac mechanics. Where *FEBio* requires external meshing software, all steps of cardiac modelling can be carried out in *Continuity* including image segmentation, model generation and FE analysis. It is particularly useful for solving problems in biomechanics, biotransport and electrophysiology. *Continuity* has been used to solve multiple multi-scale models for cardiac applications including a study on biventricular pacing and scar size on LV regional and global function (Kerckhoffs et al., 2009). *Abaqus*, *FEBio* and *Continuity* provide various constitutive models that can be applied to myocardium. However, *Continuity* also has pre-established circulatory and electrophysiology load models. *Continuity* was chosen as the primary candidate FEA software for this thesis due to its comprehensive capabilities and relevancy to the area of cardiac biomechanics.

2.6.2. Reconstruction of Cardiac Geometries

MRI and CT data have both been used for cardiac reconstruction due to their high resolution. Most often, cardiac geometry is obtained by segmenting the epi- and endocardial surfaces from a series of short-axis images and assigning spatial coordinates to points along the contours. These coordinates are then imported to FE software to create a mesh model of the heart. Various automated and semi-automated segmentation algorithms have been developed to create efficiency and precision when defining contours. Common algorithms utilise user and pre-defined threshold values as well as level set methods (Paragios, 2003). However, signal loss due to blood flow and partial volume effects (González Ballester et al., 2002) and variation of grey values make accurate automated segmentation a difficult task. Kaus et al. (2004), following similar studies, incorporated multiple a priori information sources into a fully automated deformable model segmentation technique. Prior information sources included an inter- and intra-subject shape variation and spatial relationships which were used to define constraints.

There are, however, some drawbacks of MR and CT based cardiac tissue reconstruction including the still somewhat limited spatial resolution. And despite near automation of the process, there are still challenges in accurately segmenting the images. One major

drawback of MR-based cardiac models is that they do not include the atria, papillary muscles, trabeculae or segmentation of tissue for different cell populations. Some studies have investigated incorporating histological validation of MRI and DTMRI to produce a more comprehensive cardiac model based on geometry from MRI and histological information on cell types, intracoronary arteries, papillary muscles, fibre angles, etc. (Burton et al., 2006). However, the majority of FE cardiac models disregard the smaller features of the cardiac tissue as these would increase computation time and are not necessary for many applications.

Segment (Lund University and Medico AB, Lund, Sweden), an open-source software for cardiovascular image analysis, allows for automatic segmentation of the LV based on a fully deformable model. It can be used with various imaging modalities including MRI, CT, positron emission tomography (PET) and single photon emission computed tomography (SPECT). The segmentation method utilises an enhanced edge detection scheme that includes temporal and a priori anatomical information (Heiberg et al., 2005b). The procedure also allows for identification of both endo- and epicardial surfaces as well as disqualification of papillary muscles when identifying the ventricular wall. *ITK-SNAP* (Yoo et al., 2002) another freely available image analysis software package, uses a semi-automated level set method of segmentation for various anatomical structures in the body. Although it has a wider range of applications than *Segment*, *ITK-SNAP* requires the user to accurately specify numerous parameters that affect segmentation (Yushkevich et al., 2005). For this Master's thesis, *Segment* provided a more efficient method of LV segmentation.

After segmentation, spatial coordinates defining contours from each short-axis slice are imported into FE software for volumetric reconstruction. *Continuity* uses a least squares fitting method that applies weights to data points and smoothing weights to minimise the root mean square (RMS) error between the interpolated and original measured coordinate. Past computational studies have modelled the LV as various shapes including a sphere, spheroid (Beyar and Sideman, 1984), thick-walled cylinder (Arts et al., 1979, Arts et al., 1982) and truncated ellipsoid. A prolate spheroid, or truncated ellipsoid, provides the most grossly realistic shape to model the LV. The anatomic geometry of the LV can, therefore, be best described using the prolate spheroidal coordinate system (Vetter and McCulloch, 1998). Cartesian coordinates are shown in Figure 2-11 in terms of the prolate spheroidal coordinates, Λ, M and Θ.

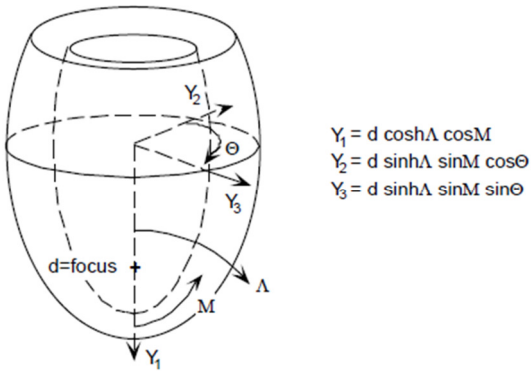

Figure 2-11: LV prolate spheroidal geometry with parameters Λ, M and Θ

With mesh nodes and elements appropriately fit to the cardiac or LV geometry, FEA can be performed in FE software such as *Abaqus FEA*, *FEBio* and *Continuity6.3* to determine stresses and strains within the myocardium.

2.6.3. Modelling Myofibre Orientation

Since the greatest stress generally occurs along fibre direction, a one-fibre model that wraps around the entire LV can be used to describe fibre orientation when modelling cardiac biomechanics (Arts et al., 2003). Other fibre models from *in vitro* measurements in animals such as rabbits, pigs and dogs provide more insight into the transmural and longitudinal fibre orientation gradients through the LV (Omens et al., 1991). More recent patient-specific cardiac modelling applies fibre angles measured from human diffusion tensor MRI (DTMRI) images (Rohmer et al., 2007) which give a much more accurate representation of fibre orientations in the human LV. Although the trend in fibre variation throughout the LV is similar for animals and humans, there are slight variations in fibre angle magnitude which can affect the resulting model. There is still room for improvement in fibre angle measurement from DTMRI since trabecular and papillary muscles cause low resolution of DTMRI on the endocardial surface. Depending on the constitutive and active models applied, LV fibre angles in a FEM can greatly affect the behaviour of both diastolic filling and systolic contraction.

2.6.4. Cardiac Constitutive Models

Passive myocardial material properties and constitutive models have been mainly described by a) stress-strain relationships from experimental tests of myocardium under prescribed loading conditions and b) estimation of material properties by matching the model deformation solution and experimentally measured myocardial deformation under prescribed loading conditions (semi-inverse method) (Watanabe et al., 2004).

The structure and organisation of cardiac muscle fibres and extracellular matrix result in the macroscopic symmetry and mechanical properties and function of heart tissue. Some researchers have attempted to deduce material properties from the EDPVR and wall geometry. While this method of analysis can provide some information on overall stiffness, it is not useful for studying regional cardiac mechanics or relating material behaviour to the three-dimensional structure of the wall.

Biaxial tensile tests of excised tissue showed that passive myocardium is anisotropic and stiffest in the fibre direction, and hence, can be modelled as transversely isotropic (i.e. isotropic in the plane normal to the fibre direction). Results from biaxial testing also illustrated that the nonlinear, viscoelastic properties of myocardium are approximately pseudo-elastic (Demer and Yin, 1983). Myocardium, therefore, is often modelled as a finite hyperelastic material, where the components of the second Piola-Kirchhoff stress are related to the Lagrangian Green's strain through the pseudo-strain energy, W. The functional form of the W is often estimated by curve-fitting experimental measurements which complicates the interpretation of parameters and limits the model to one condition. However, determining W directly from the data using a specifically designed biaxial test resulted in the following polynomial function:

$$W = c_1(\alpha-1)^2 + c_2(\alpha-1)^3 + c_3(I_1-3) + c_4(I_1-3)(\alpha-1) + c_5(I_1-3)^2 \tag{2.7}$$

This study also revealed an interaction between the isotropic and anisotropic terms (Humphrey et al., 1990).

However, with biaxial testing alone, there is uncertainty as to how the properties of isolated tissue are related to properties of the intact ventricular wall. To address this issue, Guccione et al. (Guccione et al., 1991) determined material parameters through a semi-inverse method by simultaneously inflating, stretching and twisting a FE thick-walled cylinder to obtain epicardial strains measured in isolated arrested canine hearts. A transversely isotropic strain energy function was chosen based on the fibrous structure of the myocardium:

$$W = \frac{1}{2}C(exp(Q)-1) \tag{2.8}$$

where

$$Q = b_{ff}{E_{ff}}^2 + b_{xx}\left({E_{cc}}^2 + {E_{ss}}^2 + {E_{cs}}^2 + {E_{sc}}^2\right) + b_{fx}\left({E_{fc}}^2 + {E_{cf}}^2 + {E_{fs}}^2 + {E_{sf}}^2\right) \tag{2.9}$$

The transversely isotropic exponential strain energy function with new material parameters was a vast improvement from previous models (Guccione et al., 1991).

Despite the success of the transversely isotropic model in predicting LV strain and stresses, there is evidence from simple shear tests (Dokos et al., 2002) to suggest that ventricular myocardium is locally orthotropic since there is a distinct stiffness in the cross-fibre as well as fibre direction. Under tension, muscle fibres are elongated and the primary load lies in the fibre direction. During compression, fibres buckle and the collagen network extends laterally to bear the load as illustrated in Figure 2-12.

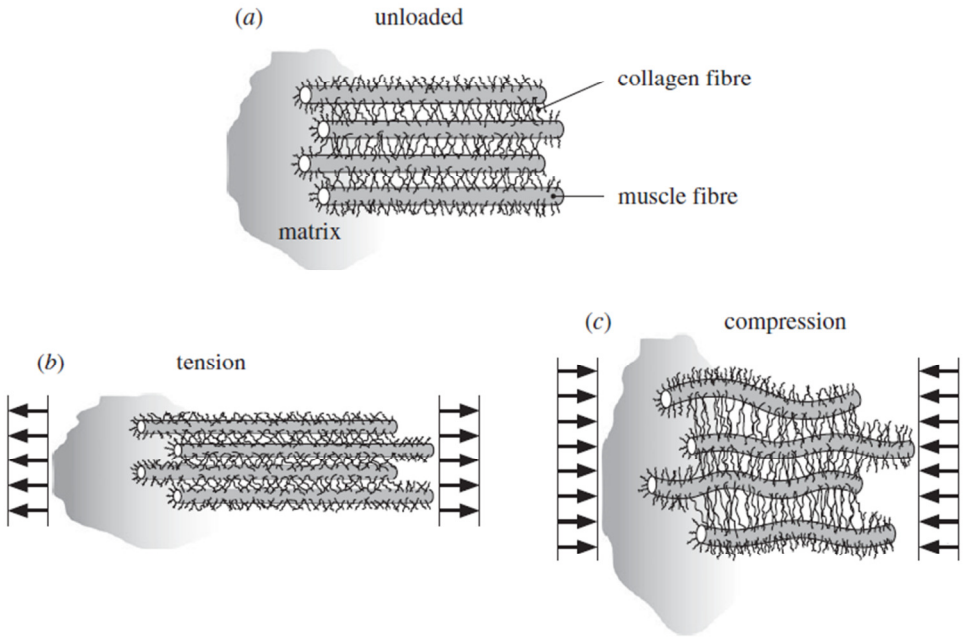

Figure 2-12: Myofibre and collagen arrangement in the a) unloaded state, b) tensile state (fibre extension) and c) compressive state (collagen elongation)

The following orthotropic strain energy function has been proposed which takes into account the cross-fibre stiffness (Holzapfel and Ogden, 2009):

$$\psi = \frac{a}{2b} exp[b(I_1 - 3)] + \sum_{i=f,s} \frac{a_i}{2b_i} \{exp[b_i(I_{4\,i} - 1)^2] - 1\} + \frac{a_{fs}}{2b_{fs}} \left[exp\left(b_{fs} I_{8\,fs}^2\right) - 1\right] \tag{2.10}$$

where a, b, a_f, a_s, b_f, b_s, a_{fs} and b_{fs} are positive material constants. The equation consists of the isotropic term in I_1, the transversely isotropic terms in I_{4f} and I_{4s} and the orthotropic term in I_{8fs}.

The assumption of incompressibility, reasonable for isolated myocardium, is not sufficient for the intact heart which can exhibit considerable tissue redistribution associated with changes in regional coronary blood supply (Usyk and McCulloch,

2003). In addition to physiologic inaccuracy, incompressible material models are difficult to converge. Therefore, in recent cardiac modelling, penalty functions have been added to strain energy functions in order to model the slightly compressible nature of myocardium (Usyk, 2002).

Infarcted myocardium has previously been modelled using the same constitutive equations for passive healthy heart tissue but with varying stiffness depending on the time point after infarction, i.e. acute, necrotic, fibrotic, etc. (Bogen et al., 1980, Wall et al., 2006). Infarcted tissue is modelled as either fully passive (Wall et al., 2006) or with reduced calcium sensitivity (Mazhari, 1998). However, limited and contradictory information is available on anisotropy in healing myocardial infarcts. In one study, isotropic infarcts were observed in rats at 6 weeks post-infarction (Fomovsky and Holmes, 2010) while in another, anisotropy was seen in 6 week old sheep infarctions (Gupta et al., 1994). A DTMRI study of rat hearts 4 weeks post-infarction showed that relative anisotropy (RA) decreased by 37% in infarcted compared to healthy myocardium. However, the infarcted myocardium was still far from isotropic (Chen et al., 2003).

2.6.5. Cardiac Mechanics

When modelling cardiac mechanics, the LV pressure throughout a cardiac cycle is typically described either in relation to the aortic pressure (i.e. LV afterload) or as a ventricular pressure-volume relationship. Afterload models, including the two- and three-element Windekessel models (Stergiopulos et al., 1999), have received more attention and are more widely used in cardiac biomechanics than LV preload (i.e. ventricular filling pressure) models (Kerckhoffs et al., 2006). For contractile myocardial properties, variable elastance formulating the active cardiac force as function of muscle length and time (McCulloch, 2005), Hill-type models in which the active fibre stress varies with shortening or lengthening (Kerckhoffs et al., 2007, Suga, 1990), and fully history-dependent models generally based on Huxley's cross-bridge theory have been suggested (Arts et al., 1982, Nevo and Lanir, 1989).

Cardiac electromechanics has been simulated with structurally and functionally integrated approaches combining cellular system models and anatomical multi-scale simulations (Hunter et al., 1998). At cellular level, the FitzHugh-Nagumo action potential equations (Kerckhoffs et al., 2006, Belik et al., 2004) and transmembrane ionic current models (FitzHugh, 1961, Nagumo et al., 1962), generally based on Hodgkin and Huxley (Hodgkin and Huxley, 1990) have been used as well as advanced

models considering transmural heterogeneity in electrophysiological properties (Belik et al., 2004, Noble and Rudy, 2001).

2.6.6. Modelling an Infarct

As discussed in Section 2.2, the ischaemic myocardium undergoes considerable changes during the four stages of remodelling following an infarction. Many groups have used FEA to model these changes in order to study the mechanical effects of a MI on LV and myocardial mechanics. In multiple models, the fibre angles in the infarct area were set to 0°, in line with the circumferential direction, in order to apply experimentally measured material properties relative to this direction (Walker et al., 2008, Wenk et al., 2011b). In others, the fibre angles as well as fibre, cross-fibre and shear strain coefficients were kept constant throughout the healthy, border zone (BZ) and infarct regions (Kortsmit et al., 2012a, Guccione et al., 2001, Wenk et al., 2010).

Ischaemic tissue becomes passive; therefore, in all previous studies, the infarct was modelled as either partially or fully non-contractile. In some models, contraction was limited in the BZ region surrounding the infarct. In others, the BZ was modelled identically to the remote healthy tissue. Very few FE models have incorporated geometric changes such as wall thinning and LV dilation, most prominent in later stages of post-MI remodelling. Some models that do account for geometric remodelling of the LV have created FE models based on MRI, CT or echocardiographic images of an infarcted heart (Wenk et al., 2011b). Most, however, use a similar LV geometry for healthy and infarcted cases.

2.6.7. Biomaterial Injection

Only three computational studies have been done on the mechanical effect of biomaterial injection (without stem cells) post-MI. In one study, single injection into anterior BZ, multiple BZ injections and single injection into the infarct zone were investigated with various injection volumes and a range of mechanical properties of the injectable biomaterial (Wall et al., 2006). A 3D FEM for large elastic deformation of ventricular myocardium (Costa et al., 1996) and a constitutive model representing passive and contractile anisotropic mechanical properties of healthy and impaired myocardium (Guccione et al., 1995) were implemented in a validated FE model of the LV previously proposed by Walker et al. (2005). Material injections were represented by local adjustment of the FE mesh (Figure 2-13). Contractility of the simulated injection site was reduced to account for the passive injected material. The latter was only required for injections in the functional BZ whereas the infarct zone did not

exhibit any active contractility. The effects of the injected material on the LV mechanics was assessed by predicting myocardial fibre stress and cardiac performance metrics such as ESPVR, EDPVR, EF, SV – end-diastolic pressure (EDP) relationships, and SV – EDV relationships. This study had important conclusions for acellular and cellular MI therapy approaches:

- Small amounts of injected biomaterial (0.5-5% of total myocardial volume) can alter cardiac mechanics, reduce wall stress and affect cardiac performance measures.
- Improvement in long-term ventricular mechanics may be achieved by passive reduction in local stress rather than adding contractile elements in the infarct zone.

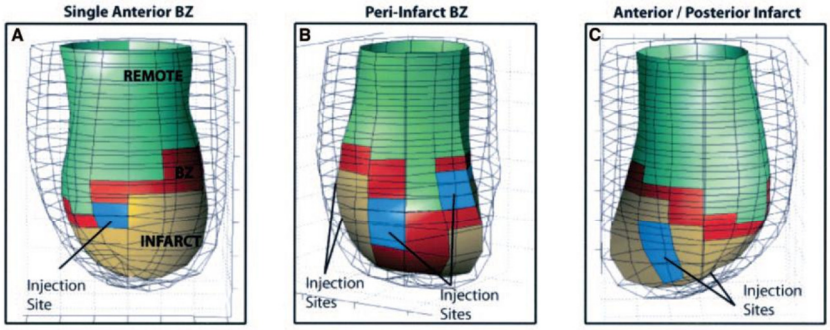

Figure 2-13: FE studies visualised: A) Single injection into the anterior border zone, B) Multiple injection sites into the peri-infarct border zone, and C) Multiple injection sites into the anterior and posterior sides of the infarct. Yellow regions are infarct; red regions are border zone, and green regions are remote (healthy) myocardium (Wall et al., 2006)

The second computational study was concerned with the optimisation of the number and placement of hydrogel injections within the LV myocardium by minimising mean ED and ES myofibre stress and maximising LV SV. The LV was modelled as an axisymmetric truncated ellipsoid and the polymeric injections were represented as bolus spheres within the myocardium. The results were somewhat inconclusive and non-intuitive. When optimising for stress/strain and SV separately, minimising the mean ED and ES myofibre stress resulted in a 3 x 10 matrix of bolus injections (see Figure 2-14) while maximising the LV SV indicated a 2 x 1 matrix (not shown). However, changing the weighting factors and simultaneously optimising for both myofibre stress and LV SV resulted in a 3 x 6 matrix (not shown) of bolus injections totalling 3.24 mL of injected material (Wenk et al., 2009).

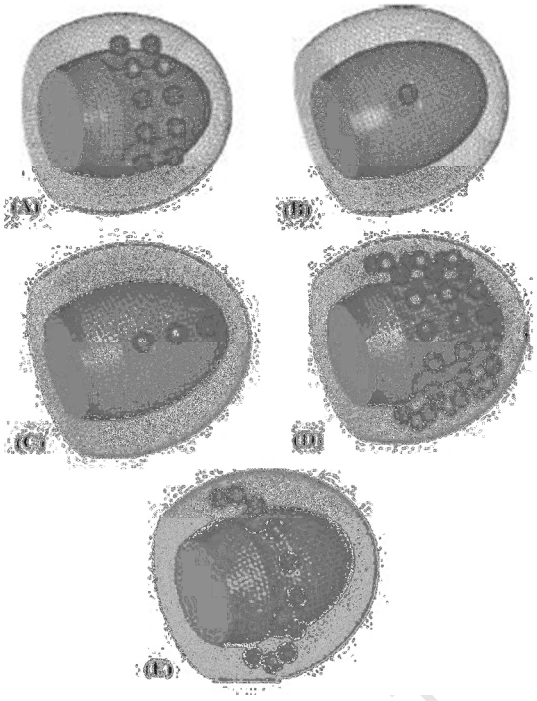

Figure 2-14: Example of five injection patterns generated during polymeric injection optimisation: (A) 2 x 5, (B) 1 x 1 (C) 3 x 1, (D) 3 x 10 and (E) 1 x 10 (Wenk et al., 2009)

In a third computational study, Wenk et al. (Wenk et al., 2011b) developed two LV ovine FE models to compare the *in vivo* mechanical effect of treating an anterioapical infarct with the injection of a calcium hydroxyapatite-based tissue filler. The models were fit to echocardiographic data from a non-treated and treated sheep heart. The injection was geometrically modelled as an increase in wall thickness. The stiffness of the treated infarct region was then optimised until the infarct region was entirely akinetic. Diastolic filling and systolic contraction were simulated and FE analysis was used to measure fibre stress in the infarct and remote regions of the LV.

The EF increased from 35% in the untreated infarcted case to 53% in the akinetic (treated) LV. In addition, the treated case exhibited lower ED and ES fibre stresses in the remote and infarct regions, as seen in Figure 2-15, compared to the untreated case (Wenk et al., 2011b).

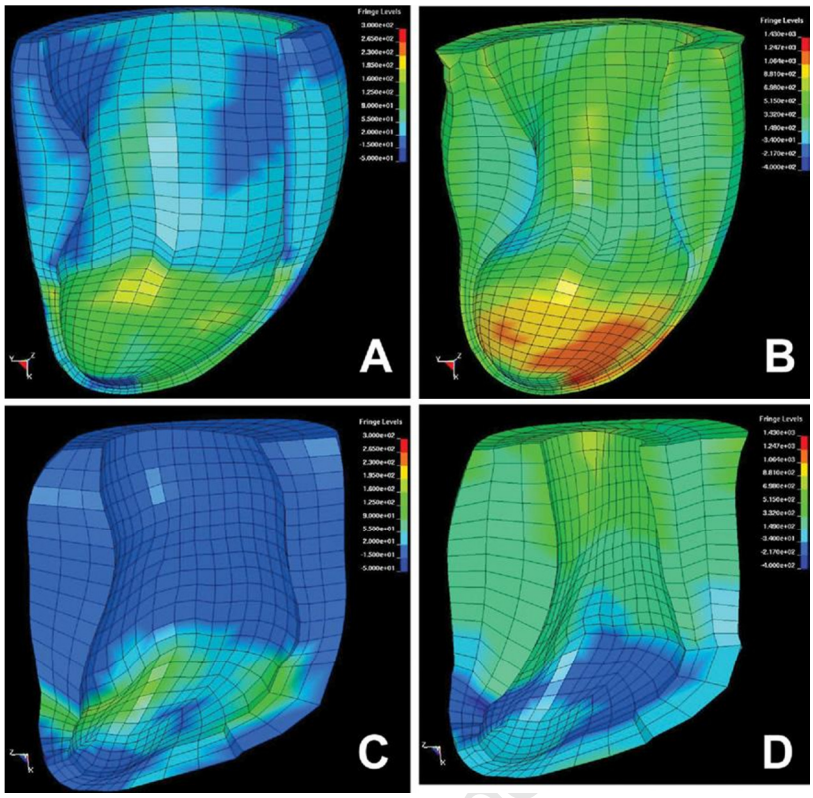

Figure 2-15: Fibre stress distribution in the lateral wall of the dyskinetic left ventricle at (A) ED and (B) end systole. Fibre stress distribution in the lateral wall of the akinetic (treated) left ventricle at (C) ED and (D) ES. (Wenk et al., 2011b)

The few computational studies that were done allow space for further research using computational mechanics to understand the effects of biomaterial injection into infarcted myocardial tissue. The first study (Wall et al., 2006) only took into account the geometrical changes of the LV and disregarded any changes in the material properties of the myocardium as a result of biomaterial injection. The second study (Wenk et al., 2009) sought to optimise the amount of injections but led to inconclusive results. The third study (Wenk et al., 2011b), although obtaining clear and positive results, assumed a treated infarct stiffness of more than 300 times that of the remote region of myocardium. This stiffness may or may not be realistic depending on the polymer being injected. This Masters research sought to complement and expand on these previous computational studies.

3. Methods

3.1. Reconstruction of Human Left Ventricular Geometry

Research-dedicated human cardiac MRI was available through Prof Ernesta Meintjes (UCT Division of Biomedical Engineering, Department of Human Biology) and Dr B Spottiswoode (Cape Universities Brain Imaging Centre, Stellenbosch University, Tygerberg). The MRI dataset (from a 36 year old male, 67 kg) consisted of 11 cine short-axis slices of a healthy human heart. The images were high resolution and represent the heart from base to apex at 17 time points over the full cardiac cycle. From these images, the endo- and epicardial contours were easily segmented to obtain ideal coordinates for LV reconstruction.

Segment (Heiberg et al. 2010, http://segment.heiberg.se/) was used to segment the cardiac MRI dataset received from the UCT Division of Biomedical Engineering. The short-axis cardiac images were loaded as a 4D cine view and the contours of the endo- and epicardium were defined for each individual slice and time point using an automatic segmentation method based on an edge detection algorithm (Heiberg et al., 2005a). The method, however, necessitated minor manual adjustment of the contours to omit valve openings and papillary muscles so that an accurate representation of the LV was obtained. Manual adjustment was done based on prior knowledge of LV geometry. By default, *Segment* selected 80 equidistant points along each contour to plot the geometry. With 11 slices per time point and 17 time points, *Segment* exported 14,960 x-y coordinates representing the entire cardiac model in an image pixel-based coordinate system. The exported coordinates did not include z-axis values. However, the slice thickness (7 mm) and spacing (3 mm) were obtained from MRI header information of the DICOM image files and *Segment* indicated a scaling factor of 1.875 mm/pixel. Therefore, the appropriate z coordinates were computed. For model creation, only the ES time point was selected as the reference time point representing the reference cardiac geometry for this study.

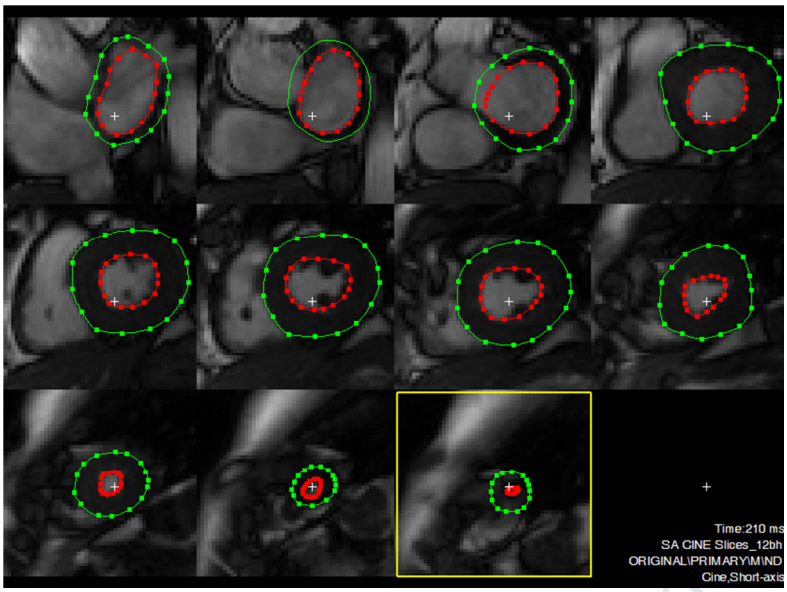

Figure 3-1: Example Patient MRI images from end-systolic time point with epicardial (green) and endocardial (red) contours of the LV segmented using *Segment*

An algorithm was implemented in *Octave* (www.gnu.org/software/octave/), an open-source high-level programming environment, to scale and shift the data to centre it on the apex and place the origin approximately 1/3 down from the base of the LV. The original MRI images weren't aligned precisely along the short axis. To solve this problem, an additional program was implemented to rotate the data until the z-axis was approximately aligned down the midline of the LV. The scaled, shifted and rotated data was then loaded into *Continuity*.

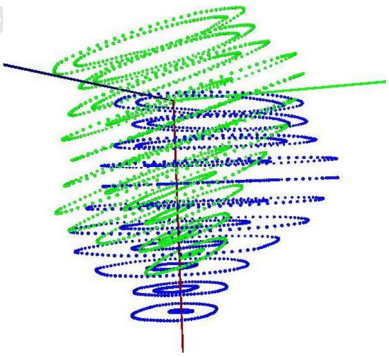

Figure 3-2: LV epicardial and endocardial contour data before (blue) and after (green) alignment with the cardiac longitudinal axis

With the final set of ES contour coordinates, a prolate spheroidal mesh was fit to the endo- and epicardial data separately in *Continuity* to obtain two separate mesh layers. *Continuity* utilises a least-squares mesh fitting method to fit the nodes of an undeformed mesh to the original data. Then, weights were applied to data points and smoothing weights were used. Multiple fittings were performed to eliminate any large curvatures estimated by the software. Each final fitting produced a mesh with less than

3% root mean square (RMS) error between the mesh and the original data set. A small hole was included to eliminate redundant nodes at the apex. The endo- and epicardial layers were then incorporated into one 3D mesh model of the LV. Once the 3D mesh was obtained, the data was converted to Cartesian coordinates described with a combination of tri-cubic and bi-cubic Hermite and Lagrange basis functions. The mesh was refined once radially to obtain and endo- and epicardial layers of elements. This preliminary model was a coarse mesh composed of 32 hexahedral elements.

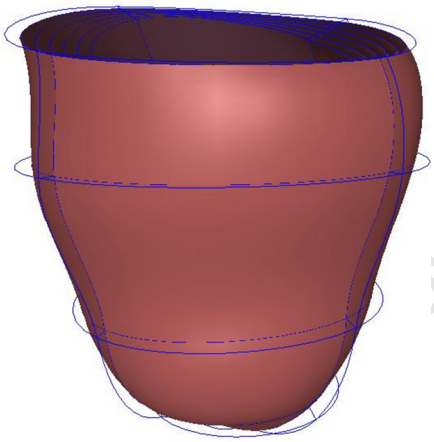

Figure 3-3: Patient-specific LV geometry

To determine the geometric accuracy of the models, the Cartesian coordinates were converted into centimetres and the endocardial, epicardial and wall volumes were compared to those computed from the original contour data set by *Segment*. Table 3-1 displays the respective volumes as well as the error between the MRI LV and model volumes. The error between each volume did not exceed 2%. The LV cavity volume at ES state (53.41 mL) closely aligns with measured LV cavity volume for healthy human hearts (Lorenz et al., 1999).

Table 3-1: MRI and model volume comparison

	Epicardial Volume	**Cavity Volume**	**Wall Volume**
MRI	181.13	53.85	127.28
Model	182.7	53.41	129.29
Error	0.87%	-0.82%	1.58%

Once the model geometry was verified, fibre angles obtained from human *ex vivo* diffusion tensor magnetic resonance imaging (DTMRI) were applied to the model (Rohmer et al., 2007). Fibre angles, applied at each node, varied depending on

longitudinal (apex, equator, base) and radial (endocardium, midwall, epicardium) location (see Table 3-2 and Figure 3-4 for graphical representation).

Table 3-2: LV myofibre angles applied to the reconstructed geometry (Rohmer et al., 2007)

	Basal	**Equatorial**	**Apical**
Epicardium	-30.45°	-28.16°	-25.88°
Midwall	9.55°	10.11°	10.67°
Endocardium	49.55°	48.38°	47.21°

Constitutive and active stress models were applied and the mesh was refined three times radially to produce a final 96 element mesh with six radial layers. *Continuity* automatically interpolated fibre angles at new nodes during radial mesh refinement to produce a linear gradient transmurally and longitudinally through the LV wall. Six radial layers were strategically chosen to adequately represent the infarct area with injected hydrogel in two different distributions. Additional radial layers would have greatly increased computation time. As well, fewer elements are needed to appropriately describe the LV when high order basis functions are used. Other cardiac and LV models created in *Continuity* have similarly used coarse meshes with high order basis functions (Kortsmit et al., 2012a, Costa et al., 1996, Vetter and McCulloch, 1998).

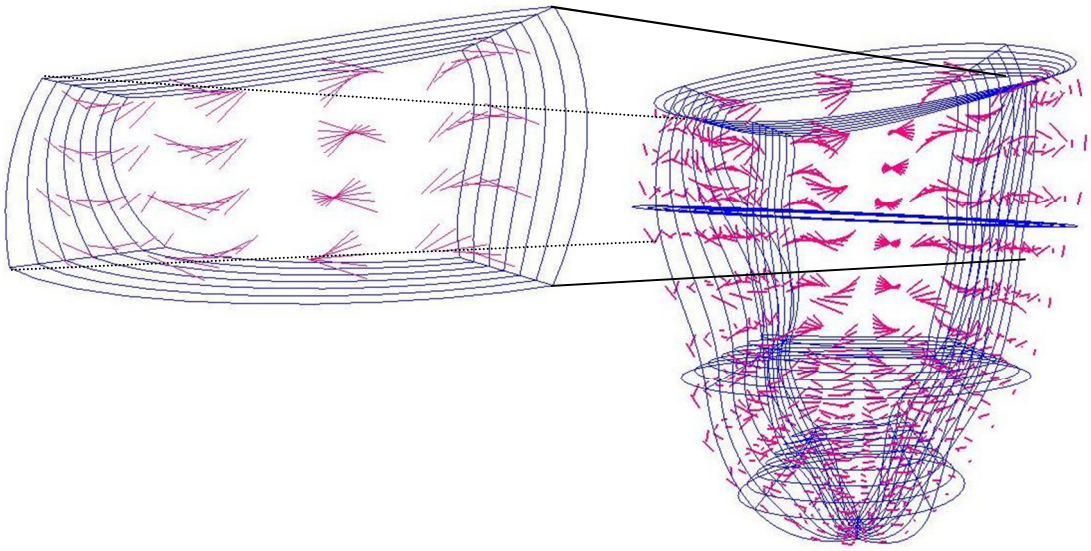

Figure 3-4: DTMRI fibre angles applied to 96-element LV mesh

3.2. Constitutive Models

Passive filling of the LV was described using a transversely isotropic exponential function of Lagrangian strains that models the material as nearly incompressible (Liu

et al., 1994). The assumption that myocardium is nearly incompressible requires the decoupling of the strain energy function into dilatational and deviatoric components:

$$W = U(J) + \widetilde{W}(\tilde{C}) \tag{3.1}$$

in which U is the volumetric contribution (Weiss et al., 1996). The more specific form of the strain energy function can be represented by the following:

$$W = \frac{1}{2}C(e^{Q} - 1) + C_{compr}(JlnJ - J + 1) \tag{3.2}$$

with

$$\begin{aligned} Q = {} & b_{ff}{E_{ff}}^2 + b_{xx}\left({E_{cc}}^2 + {E_{ss}}^2 + {E_{cs}}^2 + {E_{sc}}^2\right) \\ & + b_{fx}\left({E_{fc}}^2 + {E_{cf}}^2 + {E_{fs}}^2 + {E_{sf}}^2\right) \end{aligned} \tag{3.3}$$

where C is the stress scaling coefficient; K is the bulk modulus; and J is the determinant of the deformation gradient. The second term of the strain energy function W represents the penalty function to model the passive myocardium as nearly incompressible (Doll and Schweizerhof, 2000). In the expression for Q (Eq. 3.2), b_{ff} is the fibre strain coefficient; b_{xx} is the cross-fibre strain coefficient; and b_{fx} is the shear strain coefficient; E_{ff} is the fibre strain; E_{cc} is cross-fibre in-plane strain; E_{ss} is the radial strain transverse to the fibre; E_{cs} is the shear strain in the transverse plane; and E_{fc} and E_{fs} are shear strain in fibre – cross-fibre and fibre – radial coordinate planes, respectively**.**

Active myocardium, during systolic contraction, was modelled as the sum of passive stress derived from the strain energy function (Eq. 3.1), and an active fibre directional component (T_0), which is a function of time (t), peak intracellular calcium concentration (Ca_0), sarcomere length at which no active tension develops (l_0), stress-free sarcomere length (l_R), and maximum isometric tension achieved at the longest sarcomere length (T_{max}):

$$S = pJC^{-1} + 2J^{-2/3}Dev\left(\frac{\partial \widetilde{W}}{\partial C}\right) + T_0\{t, Ca_0, l, T_{max}\} \tag{3.4}$$

in which S is the second Piola–Kirchoff stress tensor, p is the hydrostatic pressure, J indicates the Jacobian of the deformation gradient tensor, C is the right Cauchy–Green deformation tensor, Dev represents the deviatoric projection operator and $\widetilde{W}$ is the isochoric contribution of the strain energy function, W (Wenk et al., 2011a, Weiss et al., 1996).

The active fibre directional stress component is defined by a time-varying elastance model, which, between peak tension and the end of relaxation, can be reduced to:

$$T_0 = \frac{1}{2} T_{max} \frac{{Ca_0}^2}{{Ca_0}^2 + {ECa_{50}}^2} \left(1 - cos\left(\left(\frac{t - t_0}{m l_r \sqrt{2E_{11} + 1} + b} + 1 \right) \pi \right) \right) \quad (3.5)$$

where m and b, the slope and time-intercept, respectively, of the linear relaxation duration-sarcomere length relation, are constants (m = 1.0489 s/μm and b = -1.429 s) and t_0 is the time to peak tension (Guccione et al., 1993).

In addition, the calcium sensitivity, ECa_{50}, dependent on the sarcomere length, is formulated as:

$$ECa_{50} = \frac{(Ca_0)_{max}}{\sqrt{exp\left[B\left(l_R \sqrt{2E_{11} + 1} - l_0\right)\right] - 1}} \quad (3.6)$$

where B (4.75 μm^{-1}) is a constant that governs the shape of the peak isometric tension-sarcomere length relation, $(Ca_0)_{max}$ is the maximum peak intracellular calcium concentration, l_R is the stress-free sarcomere length and l_0 is the sarcomere length at which no tension is developed (Guccione et al., 1993).

The material constants for active contraction were set to the following values: Ca_0 = $(Ca_0)_{max}$ = 4.35 μmol/ l (Ter Keurs, 1983), l_0 = 1.58 μm (Ter Keurs et al., 1980), l_R = 1.85 μm, and T_{max}= 135.7 kPa (Guccione et al., 1993).

Table 3-3: Constitutive model parameters for healthy LV model (Guccione et al., 1993)

Parameter	Variable	Value	Unit
Fibre strain coefficient	b_{ff}	18.5	
Cross-fibre strain coefficient	b_{xx}	3.58	
Shear strain coefficient	b_{fx}	1.63	
Stress scaling coefficient	C	0.52	
Bulk modulus	B	100	kPa

3.2.1. Boundary Conditions

For systolic and diastolic simulations, axisymmetric boundary conditions were applied at the epicardial basal and apical nodes. Nodal coordinates at the epicardial base as well as their circumferential and transmural derivatives were fixed. In this way, expansion of the epicardial basal contour was restricted in order to simulate the effects of stiff annuli of the valves. At the apex, nodal derivatives in the longitudinal and circumferential direction were fixed to prevent unrealistic deformations around the

small apical hole (Guccione et al., 1995, Vetter and McCulloch, 2000a). Apical nodes were not, however, fixed in space.

Referring to the schematic diagram in Figure 3-5, the mathematical expressions of boundary conditions and their locations are summarised in Table 3-4.

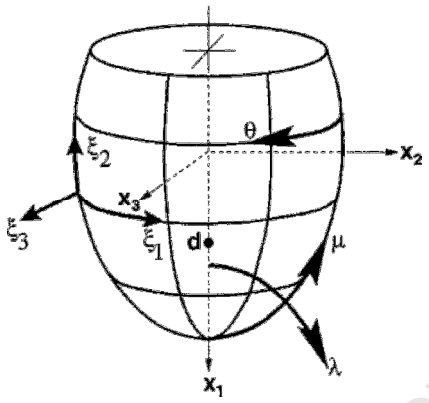

Figure 3-5: The rectangular Cartesian model coordinate system (x_1, x_2, x_3) is co-linear with the long axis of the LV. The prolate spheroidal coordinate system (λ, μ, θ) is convenient for modelling cardiac geometry. The curvilinear coordinates (ξ_1, ξ_2, ξ_3) are local finite element coordinates.

Table 3-4: Boundary conditions applied to LV models for diastolic and systolic simulations

Constraint	Location
$\delta x_i = 0$	Epicardial base
$\delta \frac{\partial x_i}{\partial S_1} = 0$	Epicardial base and apex
$\delta \frac{\partial x_i}{\partial S_3} = 0$	Epicardial base
$\delta \frac{\partial x_i}{\partial S_2} = 0$	Apex
$\delta \frac{\partial^2 x_i}{\partial S_1 \partial S_2} = 0$	Apex
$\delta \frac{\partial^2 x_i}{\partial S_1 \partial S_3} = 0$	Epicardial base and apex
$\delta \frac{\partial^2 x_i}{\partial S_2 \partial S_3} = 0$	Apex
$\delta \frac{\partial^2 x_i}{\partial S_1 \partial S_2 \partial S_3} = 0$	Apex

In these expressions, *i* represents one of the spatial coordinates: 1, 2 or 3. Constrained nodes are highlighted in Figure 3-6.

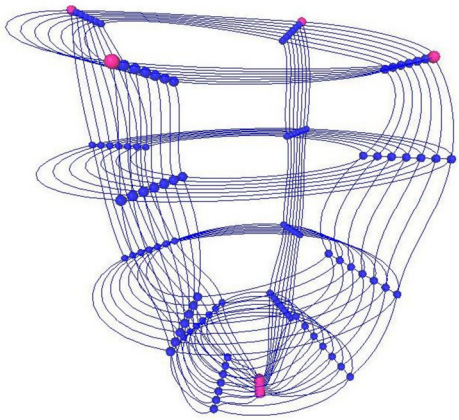

Figure 3-6: LV model with constrained nodes highlighted in pink

3.2.2. Building the ESPVR and EDPVR

Diastole was simulated by applying a pressure to the endocardial surface of the end-systolic state model. The pressure was increased linearly from 0 – 1.35 kPa (10.1 mmHg). The stress scaling coefficient (C) of the strain energy function (Eq. 3.1) was optimised until the EDV after inflation approximately matched the measured EDV from the MRI dataset. Once the EDPVR was obtained, the ESPVR was built by adding active contraction to the passive model. Systolic simulations were performed with a prescribed initial LV cavity pressure and volume, using the nodal file from the geometry corresponding to the initial pressure obtained from the EDPVR. Active contraction was applied and the volume was held constant until a peak pressure was reached. Similar simulations with differing initial conditions were run until a peak pressure of approximately 13.5 kPa (100 mmHg) and two pressure values bracketing the peak value were achieved. The peak pressures were plotted against the corresponding volumes to build the ESPVR. The number and size of time steps varied for each model in order to achieve convergence in minimal computational time. Python scripts were used to run all simulations. For each model, the EDPVR script was executed only once but the ESPVR script was run enough times to reach the desired peak pressure.

3.3. Modelling an Infarction

In the final mesh, an array of 24 elements (6 radial x 2 longitudinal x 2 circumferential) in the anterior apical region, were defined as infarction, accounting for 16% of the total LV wall volume in the ES state (see Figure 3-7). An infarct covering 20% is critical, beyond which, morbidity and mortality drastically increase (Miura and Miki, 2008).

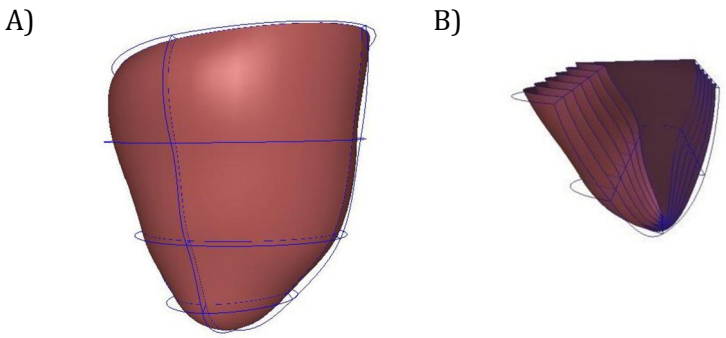

Figure 3-7: A) 96 element mesh of entire LV and B) Isolated 24 element mesh of infarct region

The effects of MI on ventricular pump function were investigated at two time points during LV remodelling, acute ischaemia and fibrosis. The stress scaling coefficient and infarct geometry were adapted for the infarcted area to mimic the changes in stiffness and wall thickness through the remodelling process.

Due to cell death and degradation of the structural proteins in the infarcted myocardium, passive stiffness decreases in the acute infarct stage (Holmes et al., 2005). For this post-infarct time point, the infarct stiffness was modelled as 50% of the healthy myocardium. As the collagen replaces the necrotic cardiomyocytes and the scar forms in the infarct region, the tissue increases in stiffness approximately 10 fold (Sun et al., 2009). Table 3-5 shows the exact values used for the stress scaling coefficients at each post-infarct time point.

Table 3-5: Stress scaling coefficients for healthy and infarcted myocardium at acute and fibrotic phases

Model	Stress Scaling Coefficient (infarct) - C	Stress Scaling Coefficient (healthy) - C
Healthy	n/a	0.52
Acute	0.26	0.52
Fibrotic	5.2	0.52

In order to create a thinned infarct wall, an incremental pressure increase was applied to the internal and external surfaces of the infarct region in order to thin the wall in the isolated region. Nodes surrounding the infarct region were fixed in every direction to restrict thinning of the LV wall outside the infarct region. This thinning procedure was repeated until the desired infarct wall volume was achieved. Active contraction was prohibited in the infarct region in each model by setting the intracellular calcium concentration, Ca_0 of the active tension model (Equation 3.5), to zero.

A) B)

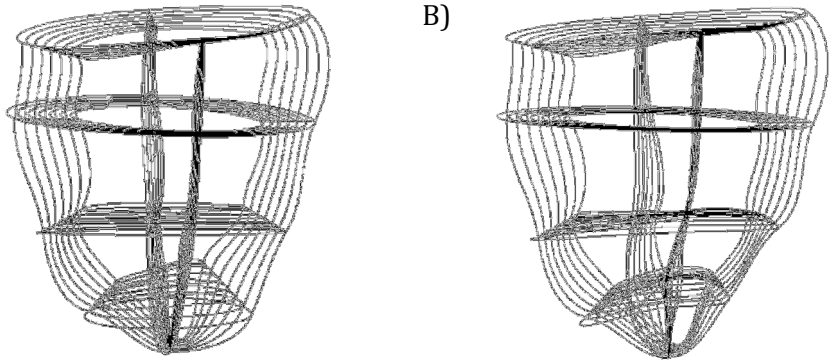

Figure 3-8: A) Healthy and B) Fibrotic mesh with thinned wall

3.4. Modelling Hydrogel Injection

Hydrogel injection was modelled in two ways: A) as bulk and B) layered injection. Histological images gathered post-*in vivo* studies (Dobner et al., 2009, Kadner et al., 2012) showed that the PEG gel resembles a bolus when injected during the fibrotic stage of ventricular remodelling (i.e. C = 5.2) and a multi-layer structure when injected during acute ischaemia (i.e. C = 0.26) (Figure 3-9).

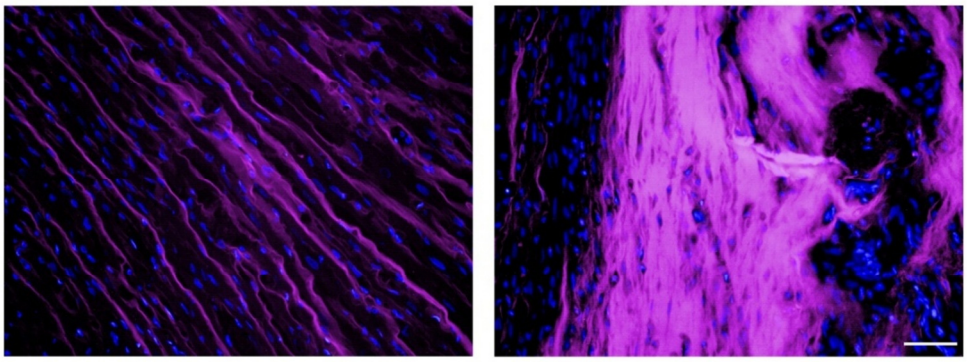

Figure 3-9: Histology images of a layered PEG injectate in infarcted rat myocardium at acute infarct time point (left) and a bulk distribution obtained when injecting 7 days post-infarction (right). PEG gel is shown in purple and cardiomyocytes seen in blue. Scale bare indicates 50 µm (Kadner et al., 2012).

For the layered distribution (Figure 3-10 A and C), layers 2 and 5 were modelled as hydrogel while 1, 3, 4 and 6 were infarcted myocardium. In the bulk distribution (Figure 3-10 B and D), layers 3 and 4 were modelled as hydrogel while 1, 2, 5 and 6 were infarcted myocardium. Both distributions are shown in Figure 3-10 where the red elements represent hydrogel and blue elements represent infarcted myocardium. The gel was modelled as a non-contractile (Ca_0 = 0 µmol/L), isotropic material ($b_{ff} = b_{xx}$ = 18.5, b_{fx} = 1.63). The stiffness of the hydrogel was based on mechanical testing of a non-degradable polyethylene glycol hydrogel which indicated that the stiffness of the gel was 50% of the stiffness of the healthy myocardium [unpublished data].

The gel injection was modelled as a wall-thickening in the infarct region. The original (healthy) geometry was used to represent the fibrotic (thinned) infarct with hydrogel. A new mesh with a thickened infarct region was created to model the acute infarct with injected hydrogel. The LV geometry with a thickened infarct was created in a similar manner to the thinned fibrotic model discussed previously. However, in this case, negative pressures were applied to the internal and external surfaces of the isolated infarct region until the desired wall volume was achieved. Again, strict constraints were applied to the nodes surrounding the infarct to prevent global thickening of the LV wall. The infarct area of the fibrotic model was thinned corresponding to decreases in wall volume of approximately 6.825 mL and the acute plus hydrogel model was thickened by the same amount. This consistency was maintained in order to model each case with approximately the same amount of hydrogel injection. Figure 3-10 illustrates the geometries of the infarct region at acute (C and D) and fibrotic (A and B) time points with both layered (B and D) and bulk (A and C) distributions of hydrogel injection.

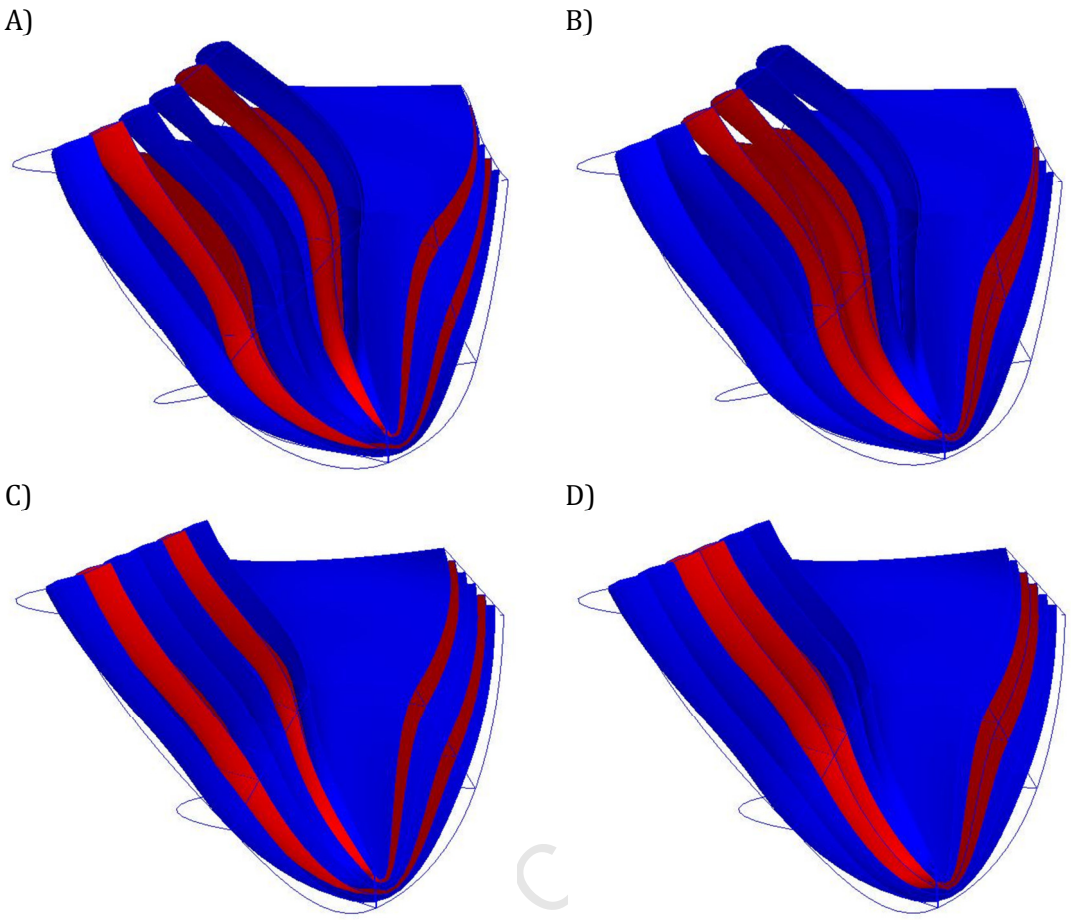

Figure 3-10: Injection scenarios: A) Layered gel injection in acute infarct simulated with hydrogel as transmural layers 2 and 5, B)Bulk injection in acute infarct simulated with hydrogel as transmural layers 3 and 4, C) Layered gel injection in fibrotic infarct simulated with hydrogel as transmural layers 2 and 5, D) Bulk injection in fibrotic infarct simulated with hydrogel as transmural layers 3 and 4

3.5. Data Analysis

The EDPVR and ESPVR were calculated and plotted to obtain cardiac functional parameters such as EF, contractility and EDV, which gave an indication of relative cardiac performance of the healthy LV, infarcted LV and infarcted LV with injected hydrogel. The calculation of these parameters was described in Section 2.1.3.

For the healthy model, the Cauchy stress and Green-Lagrangian strain (Eq. 3.7) values were computed for the Gaussian points within each individual element according to the equations below.

$$E = \frac{1}{2}(F^T \cdot F - I) \tag{3.7}$$

F is the deformation gradient tensor and τ is the stress in the tissue. Stress and strain were calculated in the fibre direction and three principal cardiac directions (circumferential, longitudinal and radial). The cardiac directional stress and strain

values were used to assess the validity of the healthy model. In particular, the averaged stress and strain in the endo- and epicardial layers at the basal, mid-ventricle and apical locations were examined along with the transmural variation of stress and strain through the LV wall. Fibre stress and fibre strain data were obtained for all models. In a post-processing *Octave* script, the stress and strain values at the Gauss points were averaged over each element. For calculations of mean infarct, mean BZ and mean LV fibre stresses and strains, the stress and strain values were then weighted according to the element volume as demonstrated in Eq. 3.8 for the mean LV fibre strain:

$$\bar{E}_{11,LV} = \left(\frac{1}{n} \sum_{i=1}^{n} \left(\left(\frac{1}{m} \sum_{j=1}^{m} E_{11,j} \right) \times \frac{V_i}{\bar{V}_{LV}} \right) \right) \tag{3.8}$$

with n = 96 and m = 27 where $E_{11,j}$ is the strain value at Gauss point j, m is the number of Gauss points per element, V_i is the volume of element i, and $\bar{V}_{LV}$ is the average element volume of the entire LV and n the number of elements in the LV. The maximum stress and strain values for the infarct region were obtained from the non-weighted values. When performing further analysis, i.e. calculating the mean fibre strain in the infarct region, any outlying values outside three standard deviations from the mean were excluded from calculations of the mean.

4. Results

4.1. Model Verification

4.1.1. Model Geometry and Cardiac Functional Parameters

An overview of epicardial, cavity and wall volume for the MRI data and the model of the healthy LV is presented in Table 4-1. After fitting a FE mesh to the MRI contour data of the healthy LV, the error in cavity and wall volume between MRI and model were 0.82% and 1.58%, respectively.

Table 4-1: LV epicardial, cavity and wall volumes for original MRI data and healthy FE mesh

	Epicardial Volume (mL)	Cavity Volume (mL)	Wall Volume (mL)
MRI	181.13	53.85	127.28
Model	182.70	53.41	129.29

Figure 4-1 illustrates the end-diastolic pressure-volume relationship (EDPVR) and the end-systolic pressure-volume relationship (ESPVR) determined for the healthy LV model. The maximal pressure that can be developed by the ventricle at any given LV volume is defined by the ESPVR, which represents the inotropic state of the ventricle. Specifically, the slope of the ESPVR represents the contractility of the LV. The predicted contractility of the healthy LV was 0.236 kPa/mL.

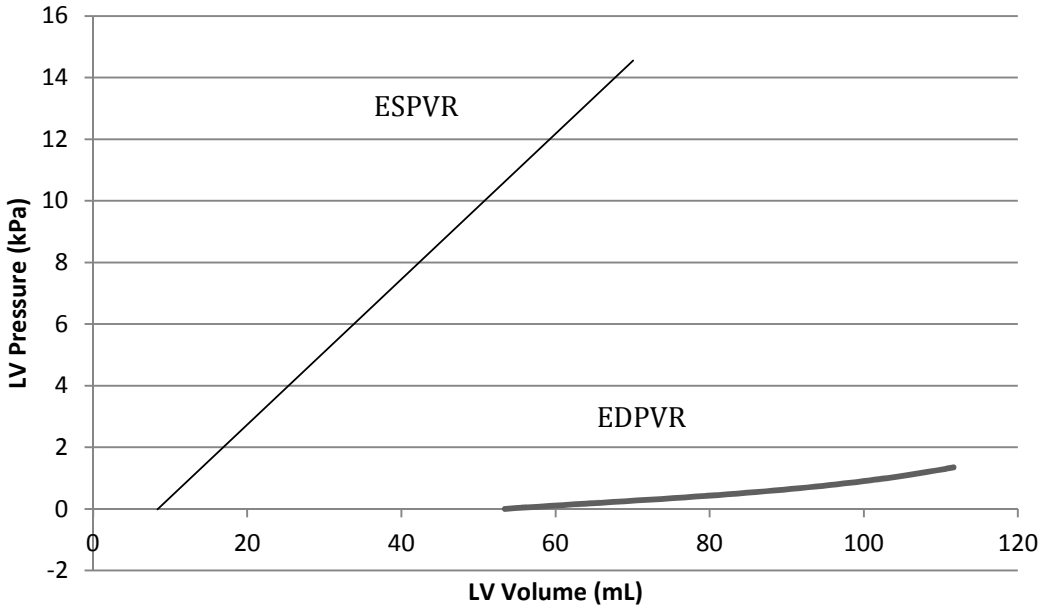

Figure 4-1: Simulated ESPVR and EDPVR for a healthy LV

As shown in Table 4-2, the model-predicted EDV is lower than the average human EDV and the predicted ESV is greater than the average human ESV. However, the model-predicted EDV closely matched the EDV calculated from MRI images (111.05 mL).

Table 4-2: Model-predicted EDV and ESV compared to average human EDV and ESV

	Predicted	**Average** (Schlosser et al., 2005)
End-diastolic Volume (mL)	111.65	120
End-Systolic Volume (mL)	65.60	50

4.1.2. Stress and Strain

The transversely isotropic exponential strain energy function used to describe passive filling of the LV and the Guccione model for active stress which described contraction of the healthy myocardium have previously been compared to *in vivo* animal data in other FE studies and have since been used extensively (Vetter and McCulloch, 2000a, Guccione et al., 1995, Costa et al., 2001, Walker et al., 2005). Predicted stress and strain values for the healthy model generally agreed with previous studies. For example, fibre strain values fell within a similar range compared to those predicted by the Guccione FE LV model (Guccione et al., 1995). Therefore, these constitutive and active stress models were subsequently used for the case study models.

4.2. Stress and Strain Predicted for Healthy Ventricle

For the healthy LV model, stresses and strains predicted in the principal cardiac directions (circumferential, longitudinal and radial) and the fibre direction at end-diastolic and end-systolic time points were assessed for validity. The analysis (described in detail in Section 3.5) focussed on

- the averaged stress and strain in the endo- and epicardial layers at the basal, mid-ventricle, and apical locations, and
- the transmural gradients of stress and strain.

4.2.1. End-diastole

Shown in Table 4-3, endocardial strains at ED were greater than epicardial strains in the fibre, circumferential, longitudinal and radial directions. The greatest stretch occurred in the longitudinal direction.

Table 4-3: Comparison of ED mean fibre, circumferential, longitudinal and radial strain averaged for the base, mid-region and apex of the LV (Endo = endocardium, Epi = epicardium)

	Fibre Strain		Circumferential Strain		Longitudinal Strain		Radial Strain	
	Epi	Endo	Epi	Endo	Epi	Endo	Epi	Endo
Base	0.099	0.137	0.112	0.116	0.213	0.353	-0.185	-0.179
Mid	0.111	0.170	0.105	0.139	0.209	0.186	-0.177	-0.208
Apex	0.041	0.037	0.034	0.027	0.070	0.026	-0.051	-0.034

The transmural gradient of the strain in the principal directions at the longitudinal mid-ventricular level is illustrated in Figure 4-2. The magnitude of circumferential and radial strains increased while longitudinal strain decreased slightly from epicardium to endocardium.

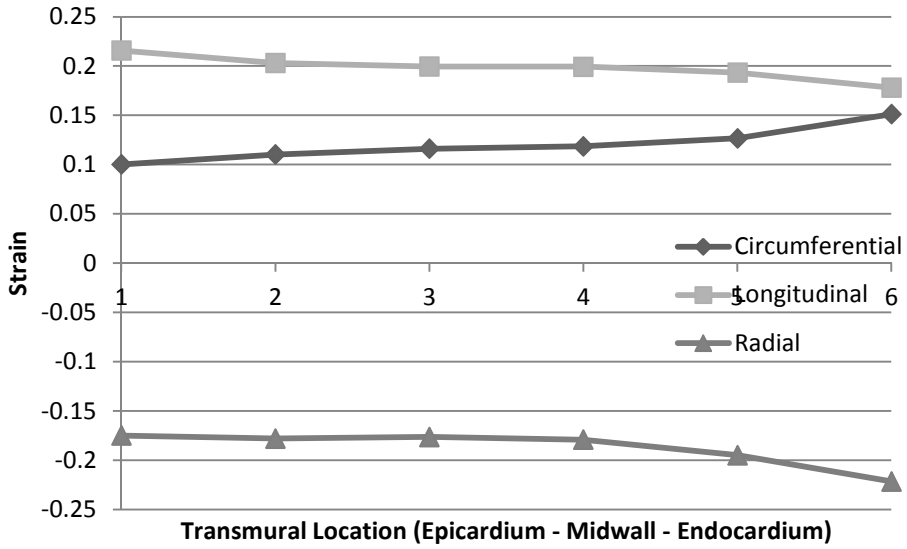

Figure 4-2: Transmural gradient of ED circumferential, longitudinal and radial strain in the mid-ventricular longitudinal location

The averaged endocardial and epicardial ED stress values showed greater basal stress at the endocardial surface than the epicardial surface in all principal cardiac and fibre directions, see Table 4-4. At the apex, circumferential and fibre stress were greater at the epicardium than the endocardium. In addition, endocardial fibre stress was considerably higher than stress in any other direction. Figure 4-3 illustrates the transmural variation of circumferential, longitudinal and radial stress from endocardium to epicardium. Longitudinal and radial stress increased nearly linearly from epicardium to endocardium whereas circumferential stress decreased from

epicardium to a minimum in the mid-wall region and increased thereafter to endocardium although remaining below the epicardial value.

Table 4-4: Comparison of ED fibre, circumferential, longitudinal and radial stress averaged for the base, mid-region and apex of the LV (Endo = endocardium, Epi = epicardium)

	Fibre Stress (kPa)		Circumferential Stress (kPa)		Longitudinal Stress (kPa)		Radial Stress (kPa)	
	Epi	Endo	Epi	Endo	Epi	Endo	Epi	Endo
Base	1.508	4.707	0.692	3.958	-0.424	2.944	-0.260	2.781
Mid	2.707	2.830	1.157	0.989	0.361	0.971	0.323	1.131
Apex	1.128	0.818	0.066	0.011	0.426	0.324	0.537	0.487

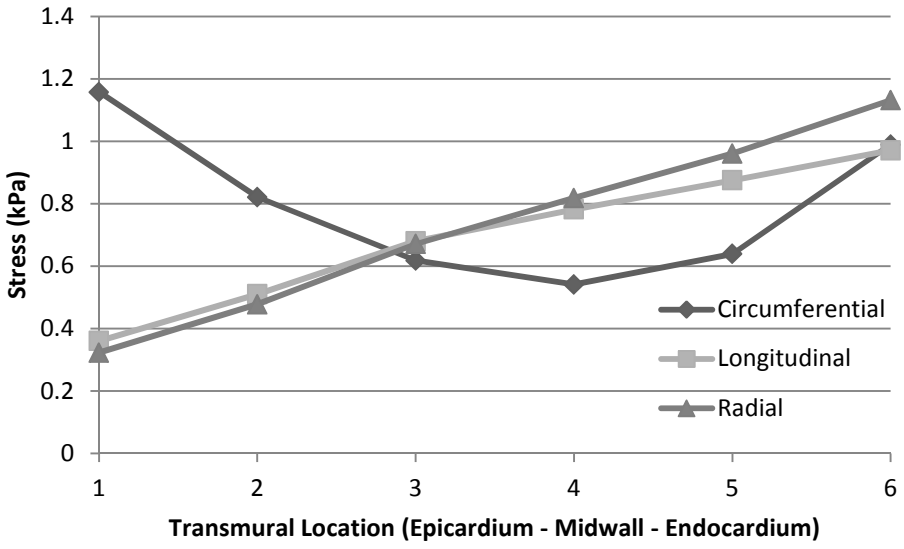

Figure 4-3: Transmural gradient of ED circumferential, longitudinal and radial stress in the mid-ventricle

4.2.2. End-systole

ES strain (Table 4-5) was negative in the fibre, circumferential and radial directions but positive in the longitudinal direction. Circumferential strain generally decreased from the base to apex. Endocardial and midwall circumferential strain was least in the mid-ventricle. Longitudinal strain decreased from the basal to apical layer. Longitudinal strain at the basal endocardium was greater than in the midwall or endocardium. Radial strain increased from base to apex. Figure 4-4 illustrates the transmural variation of ES strain in the longitudinal mid-ventricle. Longitudinal and

radial strain varied very little from epicardium to endocardium. However, the circumferential strain generally decreased from epicardium to endocardium.

Table 4-5: Comparison of ES fibre, circumferential, longitudinal and radial strain averaged for the base, mid-region and apex of the LV (Endo = endocardium, Epi = epicardium)

	Fibre Strain		Circumferential Strain		Longitudinal Strain		Radial Strain	
	Epi	Endo	Epi	Endo	Epi	Endo	Epi	Endo
Base	-0.021	-0.001	-0.021	-0.002	0.073	0.25	-0.158	-0.085
Mid	-0.01	-0.035	-0.006	-0.047	0.038	0.021	-0.14	-0.14
Apex	-0.069	-0.08	-0.022	-0.039	-0.001	-0.012	-0.028	-0.016

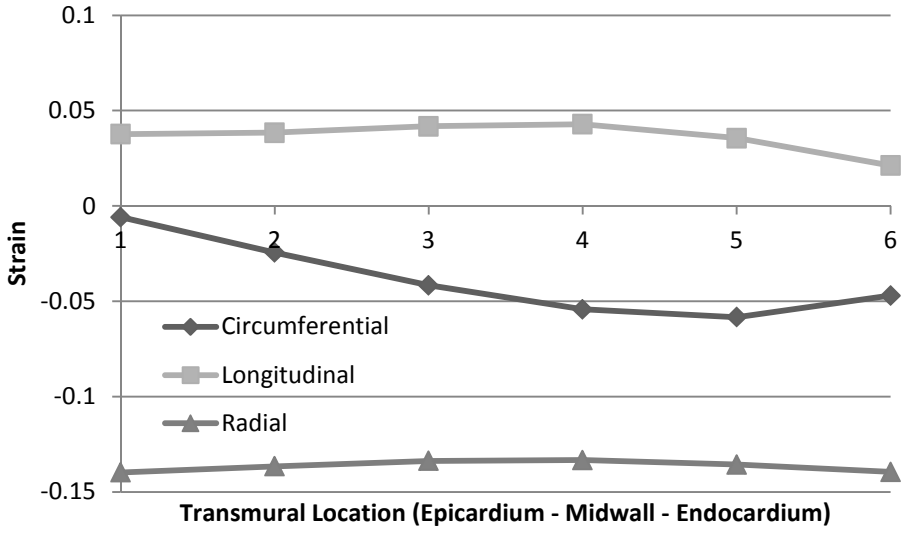

Figure 4-4: Transmural gradient of ES circumferential, longitudinal and radial strain in the mid-ventricle

ES stresses are listed in Table 4-6. Stress in the fibre and all three principal cardiac directions were greater at the endocardium than the epicardium. The magnitude of fibre, circumferential, longitudinal and radial stress each decreased from base to apex. Circumferential and longitudinal stress decreased from base to apex and radial stress increased from base to apex. Stress in all the directions was greatest at the endocardium and least at the epicardium. Figure 4-5 shows that circumferential, longitudinal and radial stress each increased from epicardium to endocardium in the longitudinal mid-ventricle. Longitudinal and radial stress only increased slightly through the LV wall.

Table 4-6: Comparison of ES fibre, circumferential, longitudinal and radial stress averaged for the base, mid-region and apex of the LV (Endo = endocardium, Epi = epicardium)

	Fibre Stress (kPa)		Circumferential Stress (kPa)		Longitudinal Stress (kPa)		Radial Stress (kPa)	
	Epi	Endo	Epi	Endo	Epi	Endo	Epi	Endo
Base	23.094	47.859	16.670	52.691	2.547	24.338	-14.784	6.840
Mid	18.498	33.869	17.594	37.557	1.705	7.261	-11.930	-1.788
Apex	2.278	6.018	1.747	5.720	-2.053	-0.979	-4.122	-1.438

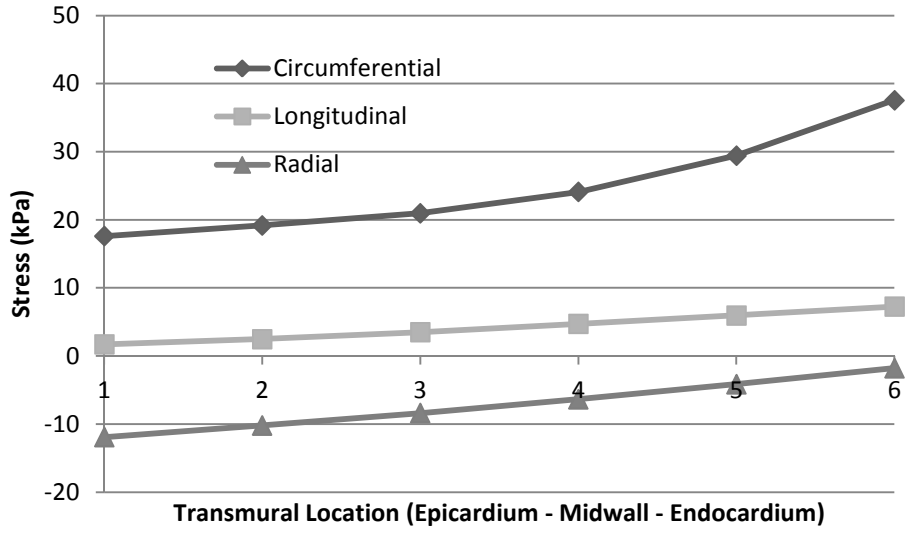

Figure 4-5: Transmural gradient of ES circumferential, longitudinal and radial stress in the mid-ventricle

4.3. Case Study: Effects of Infarction and Therapeutic Hydrogel Injection on Left Ventricular Function and Myocardial Mechanics

4.3.1. Model Geometries

The cavity and wall volume of the healthy and acute infarct models coincided since the same mesh was used for each case. The model for the acutely infarcted LV with injected hydrogel, and hence thickened wall in the infarct region, exhibited a decrease in cavity volume and an increase in wall volume. The thinned fibrotic infarct LV model resulted in a slightly greater cavity volume and a diminished overall wall volume. Since the fibrotic infarct with injected hydrogel was represented with the healthy LV geometry,

the volumes coincide between these models. The epicardial, cavity and wall volumes of each model are presented in Table 4-7.

Table 4-7: LV epicardial, cavity and wall volumes for various models (mL) (H = healthy, AI = acute infarct, FI = fibrotic infarct, LG = layered hydrogel, BG = bulk hydrogel)

	Epicardial Volume (mL)	Cavity Volume (mL)	Wall Volume (mL)
MRI	181.13	53.85	127.28
H	182.70	53.41	129.29
AI	182.70	53.41	129.29
FI	174.04	55.87	118.17
AI + LG	187.52	50.06	137.46
AI + BG	187.52	50.06	137.46
FI + LG	182.70	53.41	129.29
FI + BG	182.70	53.41	129.29

The tissue volume, hydrogel volume and total wall volume in the infarct region is summarised for all infarcted LV geometries in Table 4-8. The infarct area of the fibrotic model was thinned by 6.82 mL and the acute plus hydrogel model was thickened by the same amount. This consistency was maintained in order to model each case with approximately the same amount of hydrogel injection. However, due large curvatures in the LV wall, radial refinement did not result in infarct elements of uniform volume and the volume of hydrogel inclusion for the acute cases was greater than for the fibrotic cases.

Table 4-8: Tissue, hydrogel, and total volumes for LV wall of models for the various infarct cases (AI = acute infarct, FI = fibrotic infarct, LG = layered hydrogel, BG = bulk hydrogel)

	Tissue Volume in Infarct Area (mL)	Hydrogel Volume (mL)	Total Wall Volume in Infarct Area (mL)
AI	20.58	---	20.58
FI	13.76	---	13.76
AI + LG	18.35	9.04	27.38
AI + BG	19.16	8.22	27.38
FI + LG	13.74	6.85	20.58
FI + BG	13.79	6.80	20.58

4.3.2. Cardiac Functional Parameters

Figure 4-6 represents the EDPVR for all models. Diastole was simulated using the same parameters, boundary and loading conditions for each case. Due to the differences in the infarct region, each EDPVR displays differences in end-diastolic volume (EDV).

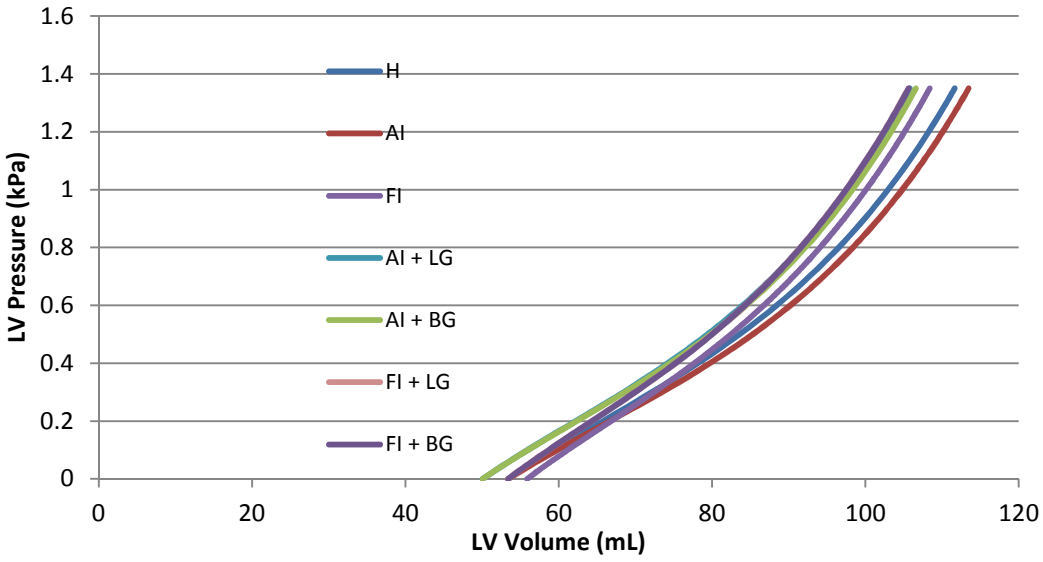

Figure 4-6: EDPVR for healthy and infarcted cases with and without hydrogel injection

The EDV increased from the healthy (111.65 mL) to the acute infarct case (113.46 mL) but decreased in the fibrotic infarct (108.39 mL), illustrated in Figure 4-7. The models of infarcted LV with hydrogel injection exhibited lower EDV values than healthy and infarct model without hydrogel for both the acute and fibrotic case. While a discernibly lower EDV was predicted for the layered gel compared to the bulk gel in the acute infarct, the EDV was nearly the same for both gel distributions in the fibrotic infarct.

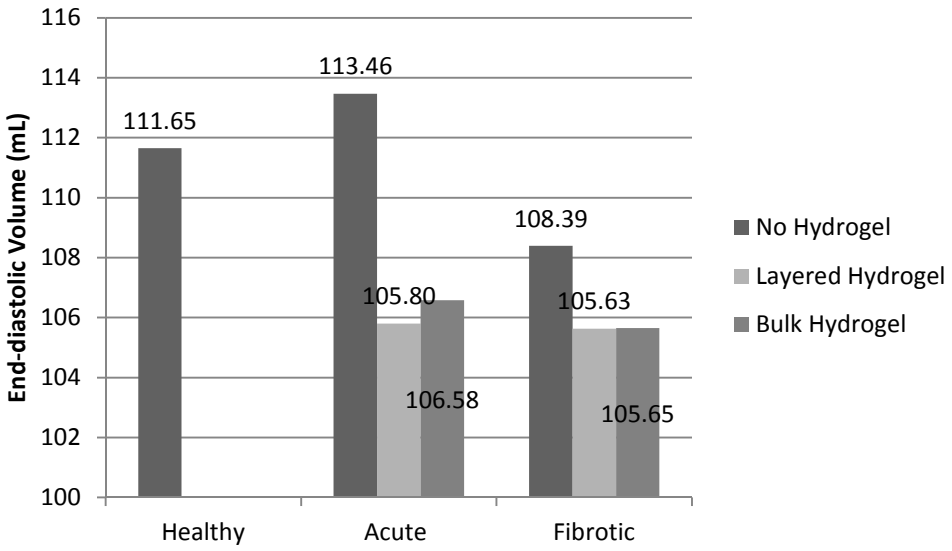

Figure 4-7: End-diastolic LV cavity volumes for healthy, infarcted and infarcted models with injected hydrogel

The ESPVR for each case is shown in Figure 4-8 and the contractility of the LV in each case was computed as the slope of the ESPVR curve.

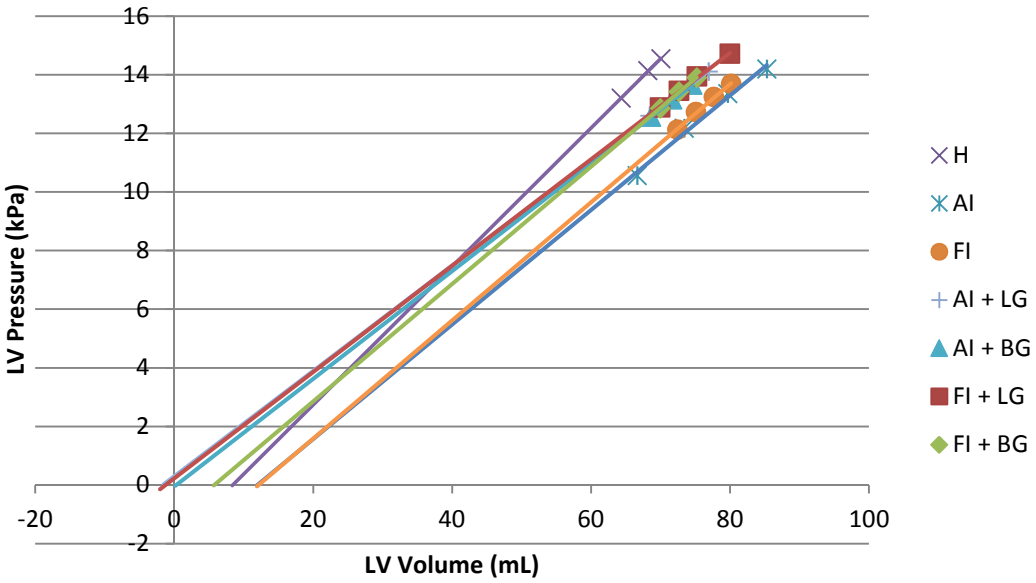

Figure 4-8: End-systolic pressure-volume relationship for each model

The contractility of the healthy model (0.236 kPa/mL) (Figure 4-9) was reduced in both the acute and the fibrotic infarct without gel injectates to 0.195 kPa/mL and 0.202 kPa/mL for the acute and fibrotic infarct models, respectively. Adding the hydrogel material led to a further decrease in contractility of the infarcted LV. This effect was more pronounced for layered injectates compared to the bulk injectates.

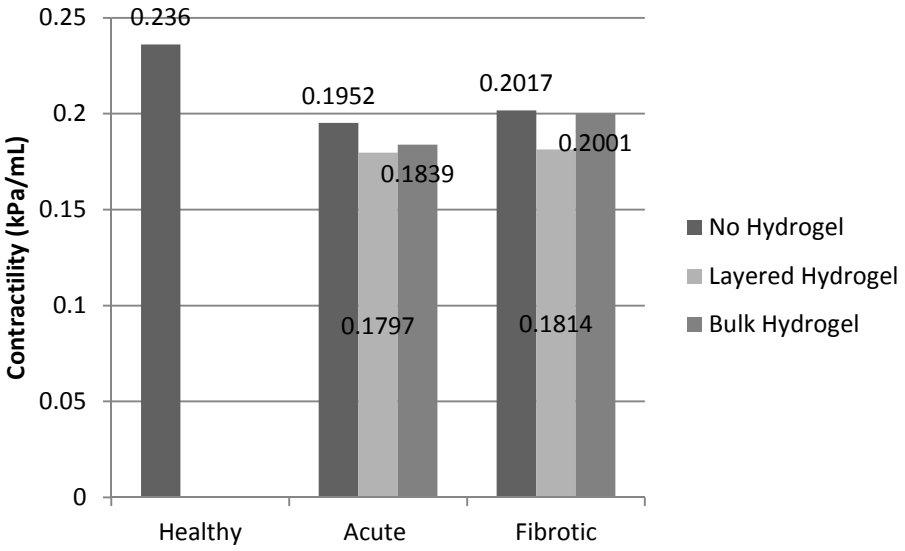

Figure 4-9: Contractility of the LV during systolic phase (calculated as the slope of the ESPVR curve)

The stroke volume (SV = EDV – ESV) decreased from the healthy case (46.04 mL) to the acute and fibrotic cases, 32.37 mL and 35.74 mL, respectively. The SV for each hydrogel case were comparable, only varying slightly between 32.33 mL and 32.88 mL. See Figure 4-10.

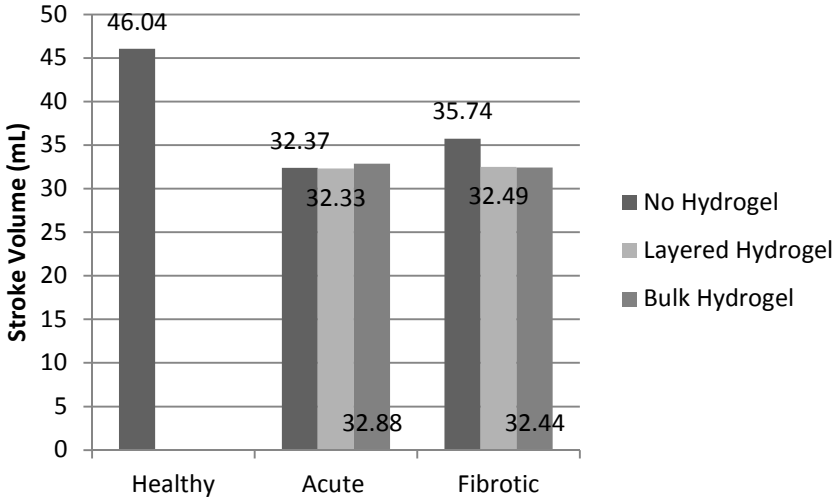

Figure 4-10: Stroke volume for each model

The ejection fraction (EF) resulting from the active contraction in the healthy case was approximately 41.23%, see Figure 4-11. EF decreased for both the acute and fibrotic infarct cases, to 28.53% and 32.97%, respectively. Injection of hydrogel, whether layered or bulk, into the acute infarct caused a slight improvement in EF infarct without hydrogel. However, hydrogel injection into the fibrotic infarct resulted in a lower EF.

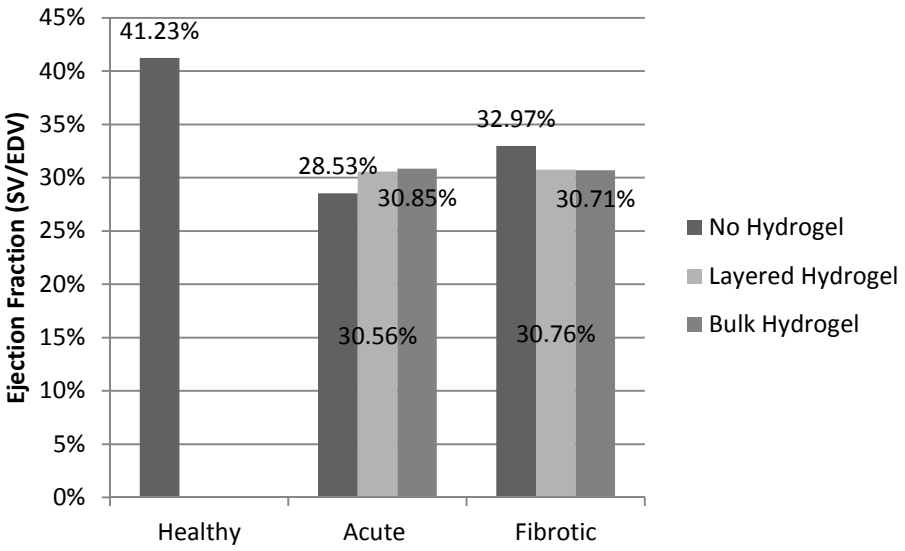

Figure 4-11: Ejection fraction (SV/EDV) for each model

4.3.3. Stress and Strain Analysis

A further part of the FE analysis using the developed models was the evaluation of stresses and strains during both passive diastolic filling of the LV and active contraction as described in Section 3.5. This section presents the Cauchy fibre stress and Green-Lagrangian strain values averaged over the infarct and entire LV for each model.

4.3.3.1. End-diastolic Fibre Stress and Fibre Strain

Figure 4-12(A), illustrates ED fibre stress averaged over the entire LV. The fibre stress increased slightly from the healthy to the acute and fibrotic infarct models. The layered and bulk hydrogel models exhibited lower mean LV fibre stress than the infarcted models without hydrogel. The fibre stress in the fibrotic infarct, shown in Figure 4-12(B), increased by 190% from the healthy case. The fibrotic model with hydrogel included exhibited a lower ED fibre stress in the infarct region. Maximum ED fibre stress in the infarct exhibited similar trends to the mean ED infarct fibre stress, seen in Figure 4-12(C). Apparent in Figure 4-12(D), mean BZ fibre stress increased slightly in the acute infarct but decreased in the fibrotic infarct compared to the healthy model. Decreased BZ stress was predicted in both infarct cases with hydrogel injectates compared to infarcts without hydrogel.

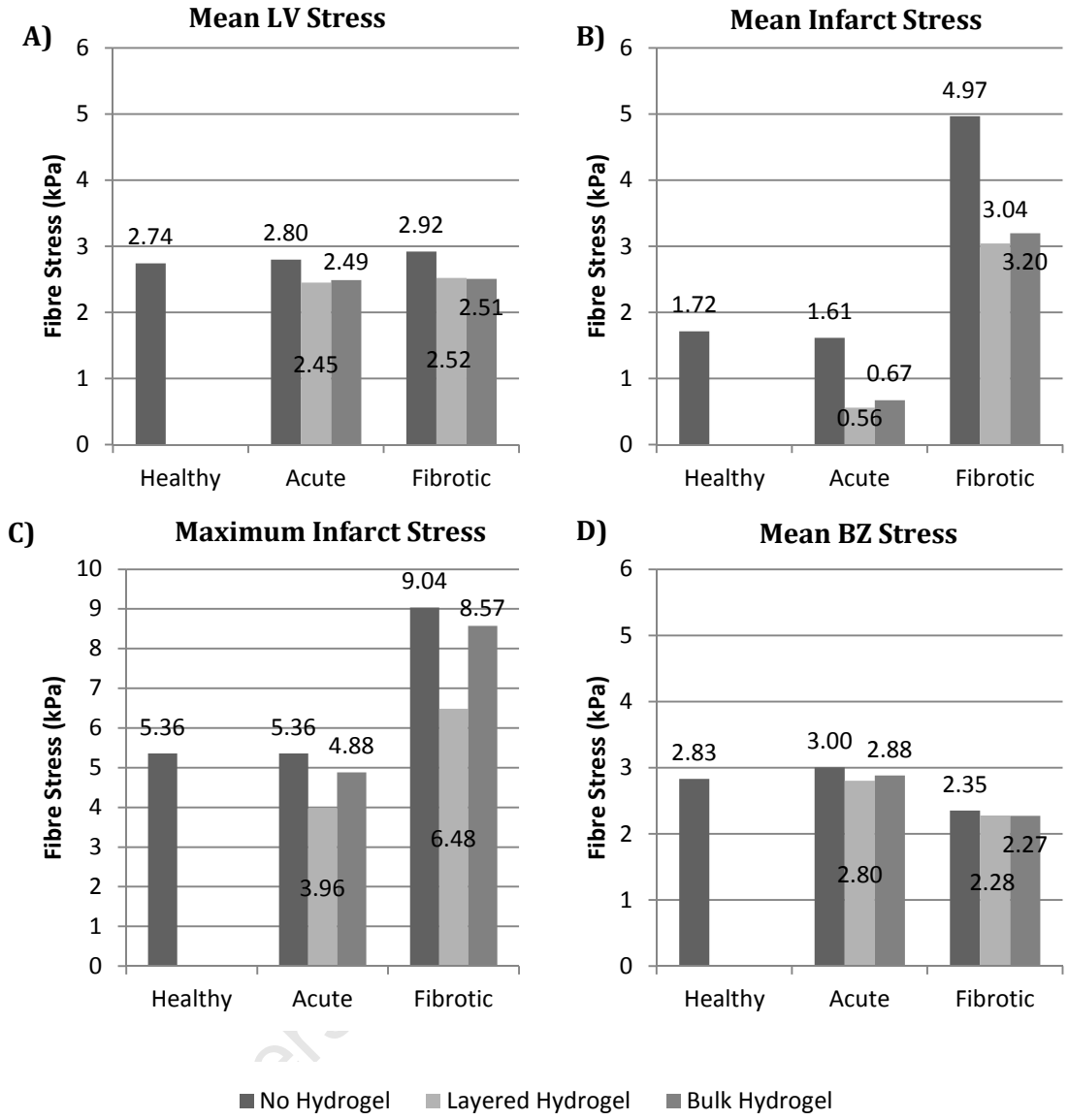

Figure 4-12: A) Mean LV, B) mean infarct, C) maximum infarct and D) mean BZ end-diastolic fibre stress (Note different scale for stress in C)

Evident in Figure 4-13(A), there were only small changes in mean LV ED fibre strain between the healthy LV model and the infarcted cases. Infarct models with hydrogel injection exhibited slightly lower mean LV ED fibre strains. However, larger differences are apparent in the infarct region. As indicated in Figure 4-13(B), mean ED fibre strain in the infarct was greater in the acute infarct than the healthy anterior apical region. Conversely, infarct fibre strain was lower in the fibrotic infarct than in the same region of the healthy case. The infarct cases with hydrogel injection exhibited lower fibre strain than their respective infarct models. Again, maximum ED fibre strain seen in Figure 4-13(C) in the infarct region similarly showed the same trend of an increase in fibre strain in the acute infarct and a decrease in fibre strain in the fibrotic infarct.

Mean ED fibre strain in the BZ surrounding the infarct exhibited only minimal variation between the healthy, acute infarct and fibrotic infarct models (Figure 4-13(D)). Similar to the changes seen in the mean LV ED fire stress, the inclusion of hydrogel in the infarct models showed slightly lower ED fibre strain in the BZ compared to the infarct models.

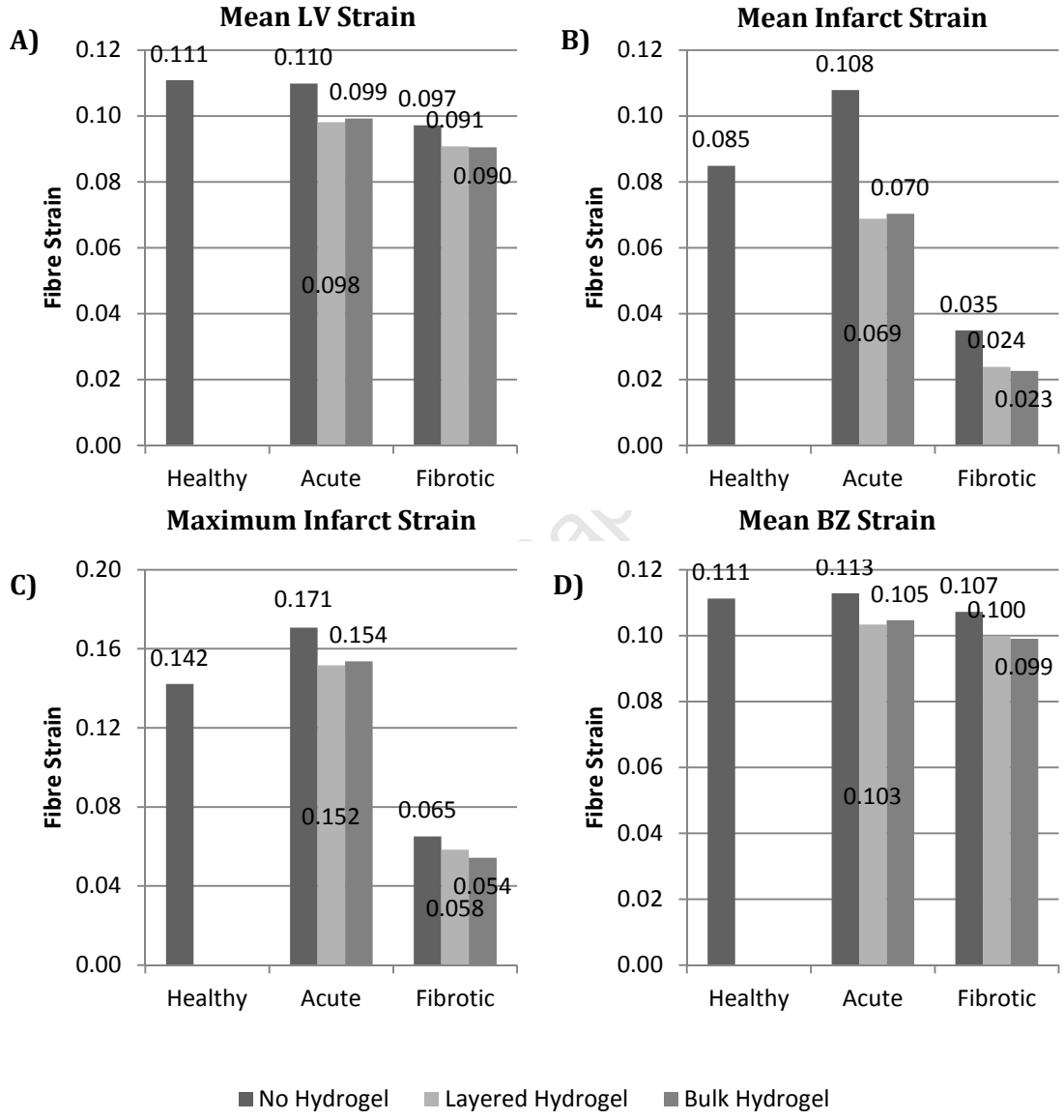

Figure 4-13: A) Mean LV, B) mean infarct, C) maximum infarct and D) mean BZ end-diastolic fibre strain (Note different scale for strain in C)

4.3.3.2. End-systolic Fibre Stress and Fibre Strain

Figure 4-14(A) illustrates a slight increase in overall ES LV fibre stress between the healthy model and acute and fibrotic infarct models. Inclusion of hydrogel showed a decrease in overall ES LV fibre stress in both the acute and fibrotic infarct models. Apparent in Figure 4-14(B), ES mean infarct fibre stress decreased in the acute infarct

model by 9.9% and increased in the fibrotic infarct model by 192% compared to the healthy case. In both the acute and fibrotic cases, hydrogel injection exhibited lower infarct fibre stress values than infarcted models without hydrogel. The maximum infarct fibre stress, shown in Figure 4-14(C), was less in the infarct models with injected hydrogel compared to the acute and fibrotic infarct models without injectate. Figure 4-14(D) illustrates that mean fibre stress in the BZ region was greater in the acute and fibrotic infarct models than in the healthy LV model. Infarct models with hydrogel injection showed slightly lower ES BZ fibre stress than without hydrogel injection at both time points.

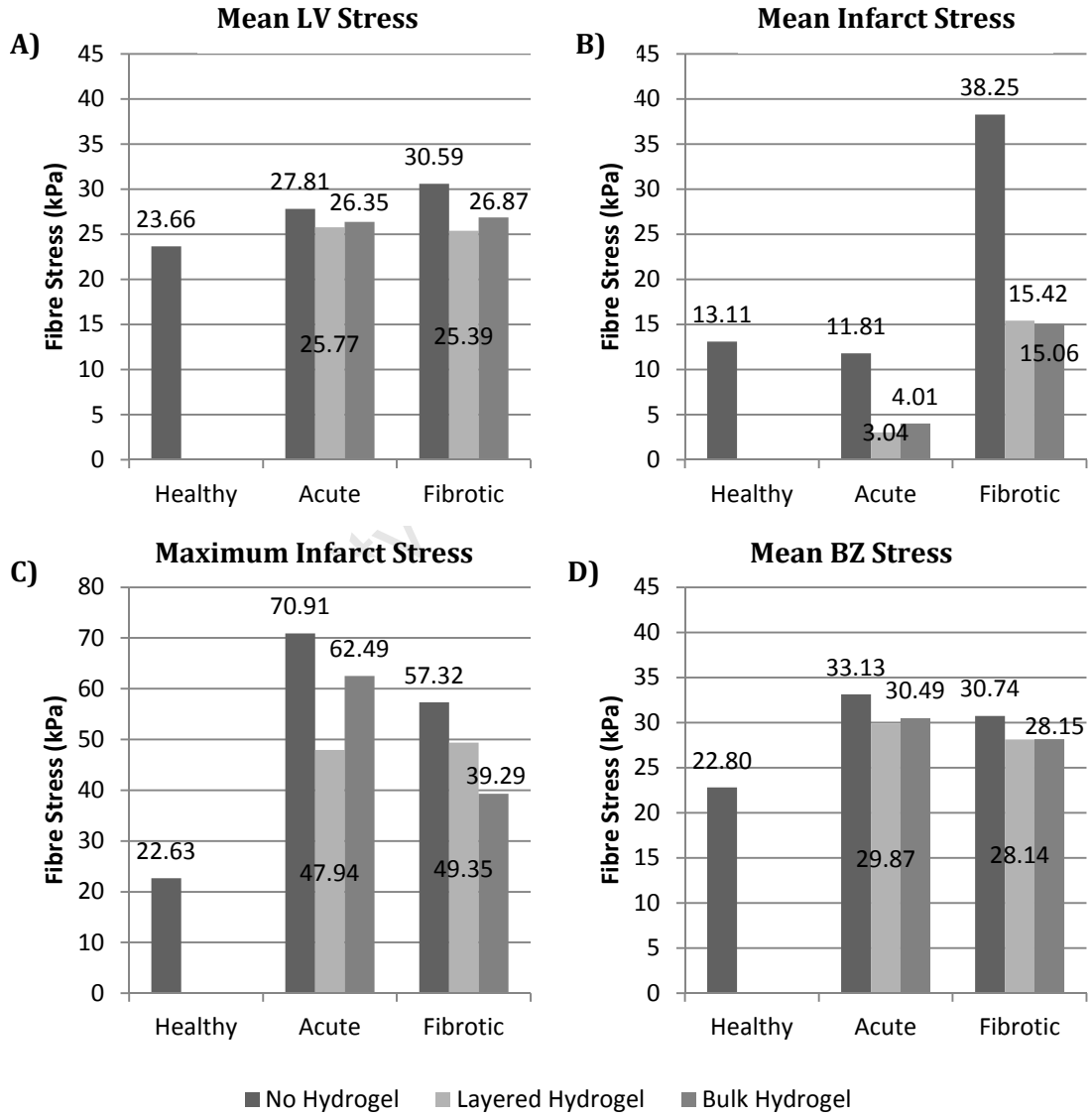

Figure 4-14: A) Mean LV, B) mean infarct, C) maximum infarct and D) mean BZ end-systolic fibre stress (Note different in scale for stress in C)

As shown in Figure 4-15(A), mean ES fibre strain for the healthy LV was negative, representing a shortening or contraction. In the acute and fibrotic infarct models, the fibre strain was positive in the infarct region, associated with fibre extension, shown in

Figure 4-15(B). For the acute and fibrotic infarcts with hydrogel, the mean fibre strain remained positive but with smaller magnitude in overall LV and infarct region. The maximum fibre strain in the infarct (Figure 4-15(C)) displayed a smaller magnitude in the acute and fibrotic infarcts with injected hydrogel than the infarct models without hydrogel. Seen in Figure 4-15(D), mean ES fibre strain was negative in the BZ region for all models except the acute infarct model. The acute and fibrotic infarct models with injected hydrogel displayed lower mean ES BZ fibre strain values compared to the infarct models without hydrogel.

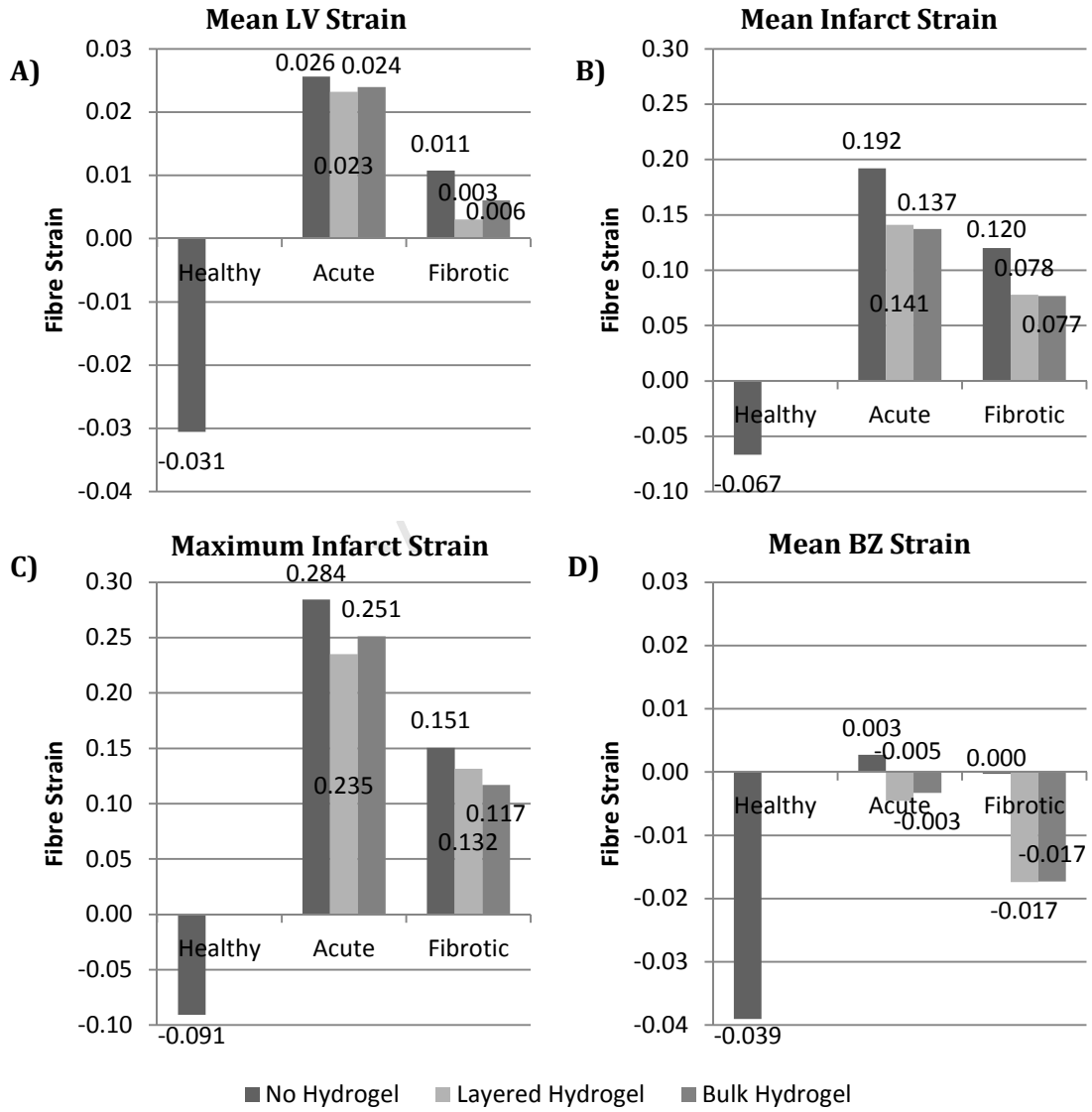

Figure 4-15: A) Mean LV, B) mean infarct, C) maximum infarct and D) mean BZ end-systolic fibre strain (Note that A and C are plotted using the same scale for fibre strain and B and C use the same scale)

5. Discussion

In this study, the FEM was used to investigate the effect of injecting a polymeric biomaterial, polyethylene glycol (PEG), into ischaemic myocardium at two time points post-MI. The LV geometry was reconstructed from human cardiac short-axis MRI and the infarcts were modelled by changing the LV geometry and material parameters of the infarcted region. Seven models were developed representing the following cases: healthy, acute infarct, fibrotic infarct, acute infarct with layered hydrogel injection, acute infarct with bulk hydrogel injection, fibrotic infarct with layered hydrogel injection and fibrotic infarct with bulk hydrogel injection.

Diastole was simulated by applying a linear pressure increase from 0 – 1.35 kPa to the internal surface, inflating the LV passively. Active myocardium was modelled by coupling the passive myocardial constitutive model with the Guccione active stress model at the cellular level. The predicted stresses and strains from diastolic and systolic simulations as well as the cardiac functional parameters were presented in Chapter 4. In this chapter, various aspects of the LV model, including the constitutive model, model parameters and boundary conditions, are discussed. Thereafter, results of the validation of the healthy LV model are examined as well as a comparison of the results between the infarcted and infarcted with hydrogel injection models.

5.1. Development of Finite Element Models

5.1.1. Geometrical Reconstruction

High resolution MR images were segmented automatically using the open-source software *Segment.* The software automatically determined epicardial and endocardial contours using gradients between pixel values to define each myocardial surface contour (Heiberg et al., 2005b). Minor manipulation was necessary in order to disregard papillary muscles and valve openings. After segmentation of the endo- and epicardial LV contours, the data was shifted to place the origin approximately one-third of the longitudinal distance from the base. The data was also rotated so that the longitudinal axis was aligned approximately through the centre of the LV cavity. This was necessary since the original MRI data obtained was not aligned precisely along the short-axis of the LV but at a slight angle. This data rotation, performed using *Matlab*, was subjective as the data was rotated until it appeared to be centred around the z-axis. Translation and rotation of the data were performed in order to have a more accurate fitting of the mesh to the segmented contours in *Continuity 6.3* following the

method developed by Nielsen et al. (Nielsen et al., 1991, Aguado-Sierra et al., 2011). The healthy LV geometry was modelled using prolate spheroidal coordinates. Surface geometry was fit to the contour data using least squares optimisation. Although the fitting was primarily automated, some manual adjustment of nodes was required in order to obtain a smooth mesh. Nodal weights were applied in order to manipulate the mesh where necessary. This method of mesh fitting reduces the number of degrees of freedom compared with interpolation using Cartesian coordinates. 2D meshes of the epicardial and endocardial surfaces were then converted into one 3D mesh described with tricubic and bicubic Hermite and Lagrangian basis functions. With less than 2% difference in LV wall volume and less than 1% difference in LV cavity volume between the model and MRI data, it was concluded that the final mesh accurately represented the geometry of the LV. In addition, the method of mesh generation could be easily repeated with similar results as the majority of the process was automated with minimal user input.

The model utilises human cardiac fibre angles obtained from DTMRI (Rohmer et al., 2007). Fibre angles in the human heart ranged from -25.88° to 49.55° transmurally from epicardium to endocardium. Helical fibre angles were applied to the endocardial, midwall and epicardial nodes. Values also differed depending on the longitudinal location: base, equator or apex. One previous computational study of intracardiac biomaterial injection therapy (Wenk et al., 2011a), despite modelling an ovine heart, used fibre angles from an arrested canine LV (Omens et al., 1991). Fibre angles for the canine measured -37°, 23° and 83° for the epicardium, midwall and endocardium, respectively. Although variation transmurally is similar, fibre angles differ between species and even individuals. Therefore, it was deemed most acceptable to use measured DTMRI from a human heart.

5.1.2. Boundary and Loading Conditions

The boundary conditions applied to the base of the LV were chosen to emulate the stiffening effects of the valves and annuli. At the apex, the boundary conditions were chosen to limit non-physiological deformations of the apical hole included in the mesh (Guccione et al., 1995, Vetter and McCulloch, 2000b).

To build the EDPVR, a linear incremental pressure increase was applied to the internal surface of the LV to build the LV pressure from 0 – 1.35 kPa. An EDP of 1.35 kPa was chosen to mimic the physiology of a healthy human heart (Bovendeerd, 2008). Although the linear pressure increase is unphysiologic, the same method was used in

numerous studies to obtain reasonably realistic results of cardiac function. Previous studies used ED pressures ranging from 0.7 kPa to 2.267 kPa (Walker et al., 2008, Kerckhoffs et al., 2007, Wenk et al., 2011b, Kortsmit et al., 2012a). Therefore, the method of determining the EDPVR was determined to be a valid method of modelling diastolic passive filling.

To build the ESPVR curve, systolic simulations were run with a prescribed initial LV pressure and volume, using the nodal file from the geometry corresponding to the initial pressure obtained from the EDPVR. Active contraction was applied and the volume was held constant until a peak pressure was reached. Similar simulations with differing initial conditions were run until a peak pressure of approximately 13.5 kPa (100 mmHg) and two pressure values bracketing the peak value were achieved. The peak pressures were plotted against the corresponding volumes to build the ESPVR (Kortsmit et al., 2012a). This method provided a simple means of obtaining and calculating cardiac functional parameters such as EF, contractility and EDV. In addition, ED and ES fibre stress and strain could easily be determined from the final ED and ES configurations. External loading on the epicardial surface was assumed to be zero for both diastolic and systolic simulations.

5.1.3. Constitutive and Active Stress Models

A transversely isotropic exponential strain energy function was used to describe the passive component of the LV tissue. Cardiac tissue has also been modelled as an orthotropic material (see Section 2.6.4). However, for this model, a transversely isotropic material model adequately described the behaviour of the tissue and was available within the modelling software *Continuity.* Constitutive parameters applied to the model, including the fibre strain coefficient, cross-fibre strain coefficient and shear strain coefficient were based on a canine heart under anaesthesia (Guccione et al., 1993) since no detailed data on human cardiac stresses and strains *in vivo* were available with which to fit new material model parameters. The parameters used in simulations have been tested and validated in previous studies (Guccione and McCulloch, 1993).

The myocardial tissue was modelled as quasi-incompressible with the use of a penalty function (Doll and Schweizerhof, 2000). Myocardium is practically incompressible due to the water in the tissue and strain energy functions traditionally describe incompressible materials. However, bulk myocardium is slightly compressible under physiological loads (Yin et al., 1996)and incompressible models are unstable and

difficult to converge. A penalty function, however, replaces the constraint of incompressibility with a series of unconstrained problems whose solutions ideally converge to the same solution as an incompressible model.

Active myocardium was modelled as the sum of the passive stress component, derived from the strain energy function, and the active fibre directional component. The fibre directional component was described using a model for active contraction based on the peak isometric tension-sarcomere length relation, the maximum peak intracellular calcium concentration, the stress-free sarcomere length and the sarcomere length at which no tension is developed (Guccione et al., 1993). The active stress model chosen provided for ease of manipulation in order to turn on and off contraction in specific areas of the myocardium in order to model infarct and hydrogel elements. It has been validated with experimental data and used in many previous cardiac computational studies (Walker et al., 2005, Wenk et al., 2011b).

5.1.4. Modelling an Infarction and Hydrogel

The LV was modelled at two time points after infarction: acute (within seconds-minutes of infarction) and fibrotic (7 days post-infarction). In both models, 24 elements in the anterior apical region of the LV model were defined as infarction. The infarct was transmural and accounted for 16% of the total LV wall volume at the initial state geometry. The acute infarct was only modelled as a reduction in stiffness within the infarct area ($C_{AI} = ½ C_H$) and the geometry was left unaltered. The stiffness of the acute infarct was chosen based on previous similar studies (Kortsmit et al., 2012a) as well as the knowledge that structural proteins begin to degrade immediately after infarction, causing a decrease in stiffness (Holmes et al., 2005). The infarcted LV at the fibrotic time point was modelled as a 10 fold stiffness increase in the infarct region due to the scar formation in the infarct region (Sun et al., 2009). In addition, the fibrotic infarct was modelled with wall thinning. In both the acute and fibrotic infarcts, the fibre angles were set to 0° and the material was assigned isotropic material properties with equal stiffness in the fibre and cross-fibre directions ($b_{ff} = b_{xx} = 18.5$, $b_{fx} = 1.63$) (Gupta et al., 1994).

The hydrogel was modelled as two different distributions within the myocardium: layered and bulk. The two distributions were chosen based on histological images of injected PEG hydrogel into infarcted rat myocardium at the acute and fibrotic time points (Kadner et al., 2012). Injected at acute ischaemia, the gel stratified into layers within the myocardium. Whereas when injected after the scar tissue had formed, the

gel appeared as a bolus of gel within the centre of the myocardium. Therefore, these two distributions were compared to determine the mechanical effect of different gel distributions. New LV model geometries were developed to incorporate wall thickening due to simulated hydrogel injection. Previous FE studies investigating the inclusion of biomaterial injection modelled the infarct region as homogenous (i.e. with no distinction between infarcted myocardium and hydrogel) (Wall et al., 2006, Wenk et al., 2011b). Although the two modelled distributions used in this study are quite simple, it is a small step toward modelling a realistic distribution of gel within infarcted myocardium.

The hydrogel was also modelled using the transversely isotropic exponential strain energy function. Based on unpublished experimental data, the hydrogel was modelled with half the stiffness of healthy myocardium. Without more experimental data on the PEG material, a more adequate material model could not be applied.

5.2. Validation of Finite Element Models

The constitutive and active stress models used in this FE analysis were previously validated with experimental data (Guccione and McCulloch, 1993, Guccione et al., 1993). However, the healthy LV FE model was further validated by comparing the fibre strain at ED and ES time points in the cardiac cycle to values from literature. The mean LV fibre strain at ED showed little variation transmurally. The fibre strains were, however, smaller at the apex due to the boundary conditions imposed in the model. Similar to ED fibre strains measured experimentally in rabbit hearts, modelled mean ED LV fibre strain was 0.109 (Omens et al., 1991).

The model predicted a mean ED LV fibre stress of 2.69 kPa. This value was compared with a similar model using the same transversely isotropic exponential strain energy function to describe passive filling which predicted an mean ED LV fibre stress of 2.91 kPa (Vetter and McCulloch, 2000a). The small difference could be due to the difference in stress scaling coefficient used in each constitutive model.

At ES, experimental fibre strains were higher than those predicted by the model, by almost a factor of five. The reason for this discrepancy is probably due to the fact that the unloaded state was used as the reference state to determine strain values at ES rather than the ED state. The unloaded geometry differs considerably from the ED geometry; therefore ES strain values are not representative of physiological strains. However, they are deemed acceptable to use for model comparison in this study. Calculated ES fibre stresses, however, are in close agreement with predicted fibre

stresses found in other studies using the same active stress model (Guccione et al., 1995, Wenk et al., 2011b). Disregarding the small stress values around the apical hole due to imposed boundary conditions, mean predicted ES fibre stress in the healthy LV model was 28.2 kPa compared to 29.4 predicted by Wenk et al. (Wenk et al., 2011b).

The ED and ES volumes predicted by the model are smaller than normal physiological measurements. However, they are in agreement with the patient MRI. With this information, the model was deemed sufficiently accurate for relative comparison of fibre stress and strains between the healthy LV, infarcted LV and infarcted LV with hydrogel layer models.

5.3. Comparison of Healthy, Infarcted and Infarcted with Hydrogel LV Models

5.3.1. Cardiac Functional Parameters

The EDV increased from the healthy (111.65 mL) to the acute infarct case (113.46 mL) due to the decrease in stiffness in the infarct region. The decrease in stiffness allowed the infarct region to distend greater than normal during diastolic filling, increasing the overall EDV. Similarly, the fibrotic infarct, ten times stiffer than the healthy tissue, reduced expansion of the myocardium in the infarct region, causing a decrease in EDV (108.39 mL) from the healthy case. Hydrogel layers were incorporated into the acute and fibrotic infarct models and were modelled as a substantial increase in infarct wall thickness associated with the volume of the hydrogel. This increase in thickness caused a large reduction in EDV in both the acute infarct (6.9% and 6.1% reduction for layered and bulk gel, respectively) and fibrotic infarct (2.5% reduction for both layered and bulk gel). There are multiple reasons for the reduction in EDV. Firstly, the increased wall thickness resulted in a smaller initial cavity volume (50.06 mL) compared to the healthy case (53.41 mL) since the thickness was increased by manipulating both the endocardial and epicardial surfaces. Secondly, the models with simulated hydrogel injection and thicker wall in the infarct region resulted in a significant decrease in strain or tissue stretching in the infarct region, leading to a reduction in EDV for both the acute and fibrotic cases with hydrogel injection, compared to the infarct cases without hydrogel injectate.

From the ESPVR for each model, the contractility was determined for each case. The contractility decreased from the healthy (0.236 kPa/mL) to the acute infarct (0.195 kPa/mL) and fibrotic infarct (0.202 kPa/mL) cases. The decrease in contractility is

ascribed to the passive behaviour of the infarct area. In the healthy LV model, all areas of the myocardium actively contract whereas the infarct area in both the acute and fibrotic infarct models only behaves passively. Therefore, contractility of the overall LV decreased with incorporation of an infarct. Inclusion of the hydrogel layers caused an additional decrease in the contractility. Hydrogel layers, like the infarcted tissue, are also non-contractile. Therefore, addition of passive material will not improve the contractility of the overall LV. The layered gel caused a greater decrease in contractility (0.178 kPa/mL and 0.181 kPa/mL for acute and fibrotic models, respectively) than the bulk gel injection (0.184 kPa/mL and 0.200 kPa/mL for acute and fibrotic models, respectively).

EF (=SV/EDV) for the healthy LV model was 41.23%, well below the normal EF for an average human (Schlosser et al., 2005) and below the EF measured from MRI LV volumes (52.3%). The discrepancy between modelled and physiologic EF is due to the fact that the active model parameters are based on a canine under anaesthesia which lowers the contractility of the LV (Guccione and McCulloch, 1993). Therefore, the lower EF, although not physiologically representative for humans, is admissible. Both infarct models exhibited a reduction in EF to 28.53% and 32.97% for the acute and fibrotic infarct cases, respectively. This was expected due to the implementation of the non-contractile infarct region, reducing the efficiency of LV contraction. The addition of hydrogel layers into the acute infarct model caused a slight increase in EF to 30.56% (change: 7.11%) and 30.85% (change: 8.12%) for the layered and bulk gel model, respectively. Conversely, the inclusion of layered and bulk hydrogel in the fibrotic infarct model caused a decrease in EF to 30.76% (change: -6.71%) and 30.71% (change: -6.88%), respectively. The decrease in EDV due to simulated hydrogel injection alone, previously discussed above, would cause an increase in EF, which can explain the change in the EF in the acute model due to hydrogel injection. Since a decrease in EF was observed in the fibrotic model due to hydrogel inclusion, the change may be explained by a reduction EDV as well as in SV. The stroke volume decreased from 35.74 mL in the fibrotic model to 32.49 mL (change: -9.09%) and 32.44 mL (change: -9.24%) for the layered and bulk hydrogel injection models, respectively. The reduction in stroke volume can be explained by the simultaneous decrease in contractility with the inclusion of hydrogel discussed previously.

5.3.2. Stress and Strain Comparison

The Cauchy stress tensor was used to compare stresses of each model since it expresses the true stress of the model. Cauchy stress is a measure of the force acting on

an element of area in the deformed configuration. The Green-Lagrangian strain tensor was used to compare strain between each model since large deformations occur between the undeformed and deformed cases. Physiologically, these strains can be as large as 30% (Bovendeerd, 2008). Large strain theory, also known as finite strain theory, deals with deformations in which both rotations and strains are arbitrarily large, invalidating the assumptions inherent in infinitesimal strain theory. Therefore, the Green-Lagrangian strain tensor which describes strain for large deformations was used to compare ED and ES strain from each model.

5.3.2.1. End-diastolic Stress

ED fibre stress averaged over the entire LV increased only slightly in the acute and fibrotic models compared to the healthy. Looking more closely at the mean fibre stress in the infarct region only, the acute infarct caused a slight decrease in mean fibre stress whereas the mean ED infarct fibre stress in the fibrotic infarct more than doubled. The significant increase in fibre stress within the fibrotic infarct is primarily due to the decrease in infarct wall thickness. The effect of the wall thickness on ED fibre stress can be explained by the equation for circumferential stress in a thick-walled cylinder with an applied internal pressure.

$$\sigma_\theta = P_i \frac{{r_O}^2 + {r_i}^2}{{r_O}^2 - {r_i}^2} \tag{5.1}$$

Where P_i is the applied internal pressure; r_O is the radius to the outer surface; and r_i is the radius to the inner surface. If the radius to the inner surface and the applied internal pressure remain the same while the outer radius is reduced, the stress will increase. In this way, the thick-wall cylinder can explain the increase in stress in the thinned fibrotic infarct model.

The stress is also dependent on the stiffness of the material. A material with greater stiffness will exhibit greater stress and a less stiff material will have lower stress. Therefore, if the strain remains constant and the stiffness increases, stress will also increase. Likewise, if the stiffness decreases, as was the case for the acute infarct, the stress decreases. The mean ED infarct fibre stress in the acute infarct model decreased by 5.9% from the healthy LV model. Conversely, the mean infarct fibre stress in the fibrotic infarct model increased drastically by 189.5%. Changes in material properties of the infarct region also affected the stress in the BZ region surrounding the infarct. BZ fibre stress increased a minimal amount in the acute infarct model and decreased slightly in the fibrotic infarct model. An increase in infarct tissue stiffness, therefore,

caused a reduction in fibre stress in adjacent tissue. Likewise, a decrease in tissue stiffness in the acute infarct model caused an increase in fibre stress in the BZ. These changes are due to the fact that infarcted tissue affects tissue deformation in the adjacent BZ.

Addition of hydrogel layers caused a decrease in ED fibre stress averaged over the entire LV due to the increase in infarct wall thickness. Mean ED LV fibre stress in the acute infarct model decreased by 12.5% and 11.1% for the layered and bulk hydrogel injections, respectively. Similarly, mean LV fibre stress in the fibrotic infarct model decreased by 13.6% with a layered gel distribution and 14.2% with a bulk gel distribution. Reductions in fibre stress were much more pronounced in the infarct region where hydrogel injection caused a 65.3% and 58.5% decrease in infarct fibre stress in the acute infarct model for the layered and bulk hydrogel, respectively. In the fibrotic model, hydrogel injection had a somewhat smaller effect, reducing fibre stress in the infarct region by 38.7% and 35.6% for the layered and bulk gel distributions, respectively. The mean fibre stress in the BZ region for the acute infarct model was reduced by 6.8% and 4.2% for the layered and bulk gel distributions, respectively. Within the fibrotic model, the layered and bulk gel injection reduced fibre stress by 3.2% and 3.4% in the BZ region, respectively. The fibre stress in the infarct and BZ was affected less by hydrogel injection in the fibrotic infarct model than the acute infarct model since the prominent property of the fibrotic infarct was the stiffness, being 10 times that of the healthy tissue and 20 times that of the hydrogel for the fibrotic infarct whereas the acute infarct stiffness was half of that of healthy tissue and equal to the stiffness of the hydrogel. Therefore, in the acute model, the increase in thickness was the prominent factor affecting ED fibre stresses.

5.3.2.2. End-diastolic Strain

Mean ED LV fibre strain decreased slightly by 0.9% from the healthy to the acute infarct model. The mean ED LV fibre strain decreased by 12.3% from the fibrotic infarct model compared to the healthy LV model due to the increase in infarct stiffness. In the infarct region, the mean ED fibre strain increased by 27.2% in the acute infarct model and decreased by 58.8% in the fibrotic infarct model compared to the healthy case. The mean ED BZ fibre strain increased slightly by 1.4% compared to the healthy case due to the acute infarct and decreased by 3.7% with inclusion of the fibrotic infarct. ED fibre strain is only a result of passive stretching due to the internally applied pressure. Despite the material changes in the infarct region, the effect on passive strain in the BZ was not great.

The addition of hydrogel into the acute infarct model caused a decrease in mean LV, infarct and BZ fibre strain. As previously discussed in relation to EDV, an increase in wall thickness will cause in a decrease in fibre strain. Therefore, addition of hydrogel into the fibrotic infarct model resulted in a decrease in ED fibre strain in the LV, infarct and BZ regions. Although the magnitude of fibre strain reduction due to hydrogel was much less in the fibrotic infarct model than in the acute infarct model, the relative reduction was similar for both cases. The acute infarct fibre strain decreased by 11.2% and 10.0% for the layered and bulk gel injections, respectively, while the hydrogel injection reduced the fibrotic infarct fibre strain by 10.3% with a layered distribution and 16.5% with a bulk gel distribution. It is interesting to observe that for the acute infarct, the layered gel distribution has a slightly more pronounced effect in reduction of the ED fibre strain compared to the bulk distribution of the gel while the opposite is the case for the fibrotic infarct case.

Addition of hydrogel decreased mean ED BZ fibre strain by 8.4% and 7.2% for the layered and bulk distributions, respectively, in the acute infarct model and by 6.8% and 7.6%, respectively, in the fibrotic model. Similar to the observation for the fibre strain in the infarct region, the layered gel distribution elicited a larger reduction in BZ strain in the acute infarct model. In the fibrotic infarct model, the bulk gel distribution had a larger impact on ED fibre strain. The difference in the effect of the layered and bulk gel distributions on ED strain should be investigated further.

5.3.2.3. End-systolic Stress

Mean LV ES fibre stress increased by 17.5% in the acute case and 29.3% in the fibrotic infarct case compared to the healthy LV model. The acute infarct caused a small decrease in mean ES infarct fibre stress (10.0%) while the stiff fibrotic infarct caused an immense increase in ES infarct fibre stress (189.5%). During systole, stress is a combination of the passive stress and the stress due to active contraction of the myocardial fibres. Since both the acute and fibrotic infarcts were non-contractile, the stress in the infarct area was solely due to the passive component. Therefore, the decrease in infarct stiffness in the acute model caused the decrease in mean ES infarct fibre stress. Likewise, the 10-fold increase in tissue stiffness as well as the wall thinning applied to the fibrotic infarct model caused the increase in mean infarct fibre stress at ES. The BZ fibre stress increased by 45.3% and 34.9% for the acute and fibrotic infarct models, respectively, compared to the healthy case.

Each ESPVR was developed by simulating active contraction until an ES pressure of 13.5 kPa was reached. Therefore, in order to achieve the same pressure with an area of infarcted, i.e. non-contractile, myocardium, the healthy tissue must contract more in order to achieve the same pressure and potentially also account for passive stretching if the infarct region in this process. This explains the increase in mean LV and BZ fibre stress at ES.

The addition of hydrogel lowered the ES fibre stress in the infarct and BZ regions. In the acute infarct model, a layered hydrogel distribution caused a 74.3% reduction in ES infarct fibre stress while the bulk hydrogel distribution caused a 66.0% reduction. Hydrogel inclusion in the fibrotic infarct model caused a 59.7% and 60.6% reduction in ES infarct fibre stress with the layered and bulk gel distributions, respectively. According to the same principle as discussed above, an increase in infarct wall thickness due to the hydrogel increases the cross-sectional area over which the force is applied. This thickening led to a reduction in infarct fibre stress at ES.

The impact of hydrogel inclusion was somewhat smaller in the BZ region. In the acute infarct model, the layered gel injection reduced ES BZ fibre stress by 9.8% and the bulk gel by 8.0%. Layered and bulk gel included in the fibrotic infarct model reduced ES BZ fibre stress by 8.5% and 8.4%, respectively.

5.3.2.4. End-systolic Strain

ES fibre strain in the healthy LV model was negative since myocardium was contracting. However, the acute and fibrotic infarcts, comprising 16% of the LV wall volume, were non-contractile and therefore, underwent passive stretching, i.e. positive strain, during systolic contraction. The infarct fibre strain increased so drastically that it caused the fibre strain averaged over the entire LV to become positive in the acute and fibrotic models. Compared to the healthy LV, the mean ES LV fibre strain increased by 183.7% and 135.1% in the acute and fibrotic infarct model, respectively. The increases in fibre strain were even more prominent when considering the infarct region only:388.3% for the acute infarct case and 280.2% for the fibrotic infarct case. The acute infarct had a greater effect on the ES fibre strain since it is not only non-contractile, but also less stiff than the healthy myocardium. Therefore, the less stiff material will undergo greater distension and exhibit larger strains. Similarly, the stiffer fibrotic infarct will inhibit stretching and reduce strain. However, although the stiffness of the fibrotic infarct increased 10-fold compared to the healthy tissue, the infarct area was non-contractile, which led to positive strain although smaller than in the acute

infarct case. The mean fibre strain in the BZ also increased as a result of the non-contractile infarct region. The acute infarct caused the mean BZ fibre strain to increase by 107.0% and the fibrotic infarct exhibited an 99.3% increase. Although less than the changes in fibre strain in the infarct region, these increases are not negligible. The BZ tissue remains fully contractile but appears to be inhibited by the adjacent non-contractile tissue.

The inclusion of hydrogel layers in the acute infarct model lowered mean fibre strain in the LV, infarct region and BZ. The mean LV fibre strain was reduced by 9.4% and 6.4% for the layered and bulk gel distributions, respectively. Hydrogel layers had an even greater effect in reducing ES mean infarct fibre strains (26.5% and 28.5% for the layered and bulk distributions, respectively). Addition of hydrogel layers reduced ES fibre strain in the BZ region in both the acute and fibrotic infarct models. Although these changes are extremely small in the acute model, the mean ES strain in BZ area changed from a positive value (i.e. stretching) to a negative value associated with active contraction. The ES mean BZ fibre strain in the fibrotic infarct reduced drastically, indicating better overall contraction in the BZ region with inclusion of hydrogel into the infarct region. The reduction in fibre strain in each region is due to the increased thickness of the infarct region. As previously discussed, the increase in cross-sectional area over which a force is applied will reduce the resulting strain. Therefore, increasing the wall thickness in the infarct area caused a slight reduction in fibre strain in the LV, infarct and BZ regions.

In the fibrotic model, mean ES LV fibre strain decreased by 71.8% and 43.9% with the layered and bulk gel distributions, respectively. The inclusion of hydrogel layers had opposite similar effect on mean ES fibre strain in the infarct region alone. Layered and bulk gel caused infarct fibre strain to decrease by 35.1% and 36.0%, respectively, compared to the fibrotic infarct without hydrogel injection. In the BZ region, both layered and bulk gel distributions altered the mean BZ fibre strain from 0.0 in the fibrotic infarct without hydrogel to -0.017, improving the contractility of the BZ region.

5.3.3. Comparison of Hydrogel Injection Results to Literature

Similar reductions in ED and ES fibre stress were observed in previous computational studies on post-MI hydrogel injection. Wenk et al. (2011) observed a 51.2% and 92.8% decrease in fibre stress in the infarct region at the ED and ES time points, respectively. No results in BZ fibre stress were given. EF increased from 35% to 53% due to the increased infarct wall thickness and subsequent reduction in LV dilation. Similarly,

injection of hydrogel into the BZ caused a reduction in ES LV fibre stress as well as a slight improvement in EF (Wall et al., 2006). In a third study, inclusion of hydrogel caused a 25% and 3% decrease in mean ED LV fibre stress for the acute and fibrotic infarct models, respectively. Similarly, hydrogel layers in an acute infarct model caused a 29% reduction in ES LV fibre stress and hydrogel layers in a fibrotic infarct caused a 2.1% decrease in ES LV fibre stress (Kortsmit et al., 2012a). This Masters research reproduced the results seen in previous computational studies of hydrogel injection therapy but also provided further insight into of the effect of the *in situin situ* distribution of the therapeutic injectate, dependent on time of injection, on cardiac mechanics.

5.4. Significance

There are six general ways in which an infarct can inhibit ventricular pump function(Holmes et al., 2005). An infarct may rupture if the stresses in the infarct region become too high. Significantly elevated myofibre stress in the infarct region was shown in this FE study as a result of the fibrotic infarct. The inclusion of hydrogel into the fibrotic infarct model elicited a 35% and 36% decrease in mean infarct fibre stress for the layered and bulk injections, respectively. This reduction in ES infarct fibre stress could potentially limit the chance of infarct rupture during healing post-MI.

Secondly, infarct stretching wastes energy generated by healthy myocardium, reducing systolic pump function dramatically (Holmes et al., 2005). At ES, the FE model showed that infarct fibre strain is positive, indicating stretching, whereas the healthy tissue exhibits negative strain, signifying that the tissue is actively contracting. Both acute and fibrotic infarcts showed infarct stretching at ES, thereby reducing systolic pump function. When hydrogel layers were added to each infarct model, infarct fibre strain was reduced. Although infarct stretching was not inhibited entirely, the reduction in infarct fibre stretching may recover some systolic functionality of the LV, thereby slowing the progression towards HF.

A stiff infarct can limit diastolic function of the remaining healthy myocardium (Holmes et al., 2005). In this study, the fibrotic infarct was modelled as ten times the stiffness of the healthy myocardium. At ED, the fibrotic infarct reduced overall mean LV fibre strain by 12.3%. This reduction in global LV ED fibre strain is an indication of impaired diastolic function. The addition of hydrogel, however, continues to reduce diastolic function by additionally limiting mean LV fibre strain. Therefore, addition of hydrogel

may not provide a benefit in preserving diastolic function during later stages of infarct healing after the stiff scar has formed.

Infarct expansion and cavity dilation increase wall stress throughout the LV. Neither of these was addressed in this study as there was no induced cavity dilation and the infarct was assumed to be the same size at both the acute ischaemic and fibrotic time point. However, the influence of cavity dilation on the therapeutic effect of the injectates was investigated in a related study (Kortsmit et al., 2012b).

Coupling to the infarct may limit deformation of adjacent myocardium in the BZ (Holmes et al., 2005). This effect was clearly shown in the results from this FE study. Both mean BZ fibre stress and fibre strain at ES increased as a result of the acute and fibrotic infarcts. ES fibre strain values changed from negative (contractile shortening) to positive (non-contractile extension) in the acute case. Therefore, tethering to the infarct had a significant effect on the deformation of the adjacent myocardium, preventing normal contraction. With the inclusion of hydrogel in the infarct region, the ES fibre strain decreased in the acute model from positive (non-contractile) to negative (contractile), signifying that the adjacent BZ tissue regained some functionality. ES fibre strain in the fibrotic infarct also became more negative with inclusion of hydrogel. ES fibre stress in the BZ decreased by 8-10% depending on the distribution of gel and the phase of the infarct, acute or fibrotic. Although the fibre stresses and strains did not return to normal levels seen in the healthy model, the reductions signify that hydrogel injection could help to preserve function of healthy adjacent myocardium.

And finally, the infarct leads to volume-overload ventricular hypertrophy and remodelling of healthy tissue (Holmes et al., 2005). Post-MI, stress and strain the non-infarcted myocardium are largely determined by the material properties of the infarct. This study showed slight changes in ED fibre stress and strain averaged over the entire LV due to the acute and fibrotic infarcts. However, greater differences were seen at ES where mean LV fibre stress increased by 17.5% and 29.3% in the acute and fibrotic infarcts, respectively. Similarly, mean LV fibre strain at ES increased by 183.7% in the acute infarct and 135.1% in the fibrotic infarct. Therefore, the material changes and passive behaviour of the infarcted tissue had a global effect on the fibre stress and fibre strain in the entire LV. Simulated injection of hydrogel reduced mean LV fibre stress and fibre strain at both the ED and ES time points by varying degrees depending on distribution and the time point of injection. Global reduction of fibre stress and fibre strain, through optimal biomaterial injection, could then prevent volume-overload

hypertrophy and remodelling of healthy myocardium. To verify this, further analysis should be done on the fibre stress and strain in only the remote myocardium.

5.5. Limitations and Recommendations

One limitation of the model is that it represents a human LV and does not account for the effects of the RV or either atria on the mechanics of the LV. The RV and LV act as two pumps in series which are mechanically coupled by the lungs. Since they are aligned in series, a perturbation in the mechanical events of one ventricle will influence the behaviour of the other. The septum between the ventricles and the thin pericardium surrounding the heart further promote the mechanical interplay (Fogel et al., 1995). Although the LV wall is much thicker and generates higher ES pressures, the RV can affect LV pressure generation (Santamore et al., 1988). In addition, omitting the RV can allow greater distension of the LV septal wall. A biventricular model would produce more accurate results since it would take into account the mechanical interactions between the right and left ventricles. Despite the interventricular interaction, many cardiac computational studies have previously been carried out modelling only the LV (Wall et al., 2006, Wenk et al., 2009, Wenk et al., 2010, Wenk et al., 2011a, Guccione et al., 1995). And more specifically, the only prior computational studies investigating the effect of biomaterial injection into infarcted myocardium also did not include the RV. Disregarding the RV simplifies the FE model, reducing the number of elements and consequently, the computational time.

The hydrogel was modelled as several uniform thin layers and one single bulk layer, respectively, within the infarcted myocardium in an attempt to represent *in vivo* observations, as described in Section 3.4. Figure 3-9shows histology images of layered and bulk *in situ* distributions of polyethylene glycol (PEG) hydrogel injectates in infarcted rat myocardium (Kadner et al., 2012). It is apparent that both modelled distributions fall short of representing the true geometry of the injected biomaterial. The coarseness of the mesh prevented modelling the hydrogel injection with more detail. A very fine mesh would have allowed more precise geometrical modelling of the injection, which could lead to a more accurate solution, but would have increased computational time. Nevertheless, the discrete representation of the injectate was an initial step towards the *in situ* distribution of the injectates compared to previous studies in which the presence of biomaterial in the infarcted myocardium was described through local thickening and adjustment of the material properties in the

infarct region while geometrical features of the injectate were not included (Wenk et al., 2011b, Wall et al., 2006).

The coarse mesh also limited the specificity in element-based calculation of stress and strain in the border zone region of the LV. The border zone is typically defined as the region immediately adjacent to the infarcted myocardium. However, due to the size of the elements, the border zone region in the calculations takes up approximately 32% of the LV wall volume whereas the infarct area only takes up 16% of the wall volume. The coarseness of the mesh results in a gross overestimation of the BZ region. A more refined mesh could be used to calculate stresses and strains in the BZ region, although numerical problems were encountered in this study in attempts to use finer meshes. An alternative option may be to determine stress and strain values at selected gauss points of elements surrounding the infarct region rather than the entire elements.

The geometry of the fibrotic infarct model was created by inducing wall thinning observed *in situ*. In a similar manner, the geometry of the LV models with injected hydrogel was created by inducing wall thickening. Amounts of wall thinning and wall thickening were applied with a priori information on infarcted hearts and volumes of injectate used in post-MI hydrogel therapy. However, LV dilation, most prominent in later stages of LV remodelling was not incorporated into the fibrotic infarct model. Therefore, the initial LV cavity volume in the fibrotic infarct model was less than what would be observed *in vivo*. A more accurate means of modelling the LV geometry for the infarcted and treated cases would be to use MRI of an infarcted heart and an infarcted heart with injected hydrogel. Since hydrogel injection is not yet an accepted therapy for post-MI treatment in humans, it is impossible to obtain imaging data of a treated and non-treated human infarcted heart. However, with recently developed in-house small animal MRI, the rat model may potentially be used to obtain cardiac MRI and create FE models with a more accurate geometry representing the infarcted LV and infarcted LV with injected hydrogel.

Another limitation of the present FE models is that the residual stresses in the cardiac wall are not accounted for. Although the LV is continually loaded *in vivo*, a starting mesh of the geometric “unloaded” state is ideal for simulating diastolic filling and systolic contraction in order to approximate accurate stresses and strains at any point in the cardiac cycle. While employing an unloaded configuration of the heart may be desirable, previous researchers have used the ES (Walker et al., 2005) or mid-diastolic (Sermesant and Razavi, 2010) configuration as the reference geometry since the ventricular volumes are closer to the expected unloaded diastolic volume. This model

was created using a near ES configuration as the reference geometry to approximate the LV at after isovolumetric relaxation, as shown in Figure 5-1.

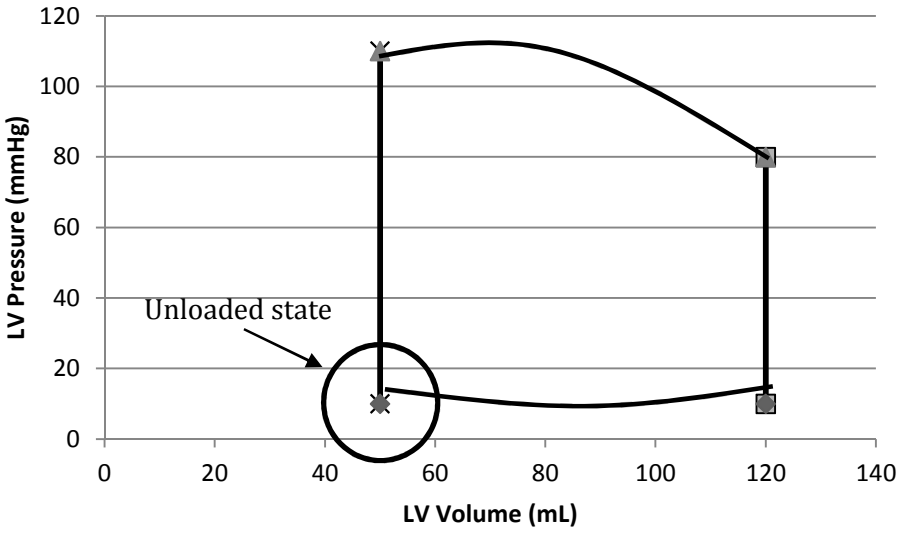

Figure 5-1: Approximate unloaded state of the LV on the PV loop

However, it will be useful in future research to determine the unloaded or reference geometric state of the LV in order to account for residual stresses in the model. One method for determining the unloaded geometry in cardiac ventricles is based on the multiplicative decomposition of the deformation gradient tensor. The objective of the iterative estimation scheme is to find the unloaded reference geometry that minimises the difference between the measured end-diastolic geometry and the computed geometry when the unloaded model is inflated to the measured end-diastolic pressures (Aguado-Sierra et al., 2011). Another method of determining the unloaded geometric state of the LV and the residual stresses is being developed by collaborators at UCT and may be implemented in future cardiac models. In this research, the results are accurate enough as they provide a basis for comparison between healthy, infarcted and treated cases.

The active stress model incorporated into the LV model and the associated parameters were originally used to describe active mechanics of a canine heart. Although canine and human LV mechanics are extremely similar, minute differences may affect the final calculation of stresses and strains. Ideally, mechanical testing should be performed and parameters should be fit to experimental data of human myocardium in order to use a more accurate model for the active stress.

The EDPVR was generated by applying an incremental pressure increase on the endocardial surface of the LV until the EDP of 1.35 kPa was achieved. The ESPVR was

built by allowing the pressure to increase due to the active contraction model until the desired ESP was achieved. The LV was not coupled to a closed-loop circulation model. Ideally, a suitable circulation model, such as a Windkessel model, should be applied to account for pre- and after-load effects of the circulatory system. In a model coupling circulation to LV mechanics, end-diastolic pressure also becomes an output of the model and no longer needs to be prescribed. By coupling to a closed-loop circulation, the introduction of an ischaemic region would shift the PV loop to the right, increasing both ED and ES strain and stress values even more than what was calculated in this study. Other computational studies have, however, circumvented the use of a circulation model by adapting pressure and volume changes within the LV to model the behaviour of passive inflation and active contraction. Many models utilise an internal pressure increase to simulation filling (Vetter and McCulloch, 2000b, Walker et al., 2008). Systole has also been simulated without the use of a circulation model by simply applying an active contraction until the desired ES volume is reached (Walker et al., 2008). Therefore, although a Windkessel or similar circulation model would be ideal to account for pre- and after-load effects, it is not necessary to achieve accurate and meaningful results.

The model also does not incorporate electromechanical coupling. A weakly coupled electromechanical model would simulate electrical activation using the Eikonal model, for example, and then use the time map from the activation model to coordinate mechanical contraction at specific activation times for individual nodes in the mesh. In a strongly coupled model, the electrical and mechanical equations would be solved simultaneously (Nickerson et al., 2005). Despite the apparent usefulness and precision that electromechanical coupling would bring, electromechanics would greatly increase computation time. Many groups have modelled the mechanics of the LV assuming simultaneous contraction of all regions of the LV (Walker et al., 2005, Guccione et al., 1995, Hunter et al., 1992). The results of this simplification have been verified with *in vivo* data and it is apparent that electromechanical coupling isn't necessary when only assessing the mechanics of the LV. To analyse electrical activation, needed for assessing resynchronisation therapies, electromechanical coupling would become necessary.

The hydrogel was modelled using the same constitutive law as was used for the myocardium with values for constitutive parameters of the hydrogel based on unpublished data. Ideally, a constitutive law should be developed to accurately model the mechanical behaviour of the polyethylene glycol (PEG) hydrogel. Similar studies, however, modelled the injection only as an increase in volume and did not model the

gel as a separate material within the myocardium (Wall et al., 2006, Wenk et al., 2011b). Wenk et al. (2011) optimised the parameters of the myocardium with injected medium to produce an akinetic material. Therefore, the constitutive model is based on no experimentally measured material parameters. Recently, micro-indentation testing was performed at Eindhoven University of Technology on the PEG hydrogel used in our *in vivo* studies to provide experimental data with which to fit a constitutive law. Future work will incorporate the PEG hydrogel specific constitutive model.

Based on the current study, it is suggested to expand the investigations to study the amount of biomaterial that is injected, location of injection (infarct or BZ) and material properties of the injectate. By altering the thickened geometry at each, acute and fibrotic phase, the simulated amount of biomaterial injection can be increased or decreased. Similarly, the location of wall thickening can be changed to simulate hydrogel injections in areas other than the infarct. To explore the effect of hydrogel stiffness, the same models could be used but with different material properties for the PEG gel. One benefit previously discussed of synthetic biomaterials is that their material properties can be adapted relatively easily. Therefore, FE modelling could be used to find the optimal material parameters of the hydrogel. Through these expansions of the current FE model, the fibre stresses and strains as well as the cardiac functional parameters can be compared to determine the optimal design parameters of post-MI hydrogel injection therapy. The results can then guide future studies using animal models.

6. Conclusions

Finite element analysis was successfully accomplished using the freely available software *Continuity 6.3b* and the results were validated using strain and stress values from literature. Post-infarct hydrogel injection therapy was evaluated on the efficacy of a) improving cardiac functional parameters, b) reducing elevated myofibre stress in the infarct and BZ regions and c) reducing elevated myofibre strain in the infarct and BZ regions. After a MI, elevated myofibre stresses in the BZ and remote regions of the myocardium lead to volume-overload hypertrophy and remodelling of healthy tissue. One goal of any post-MI therapy is to reduce elevated myofibre stresses. In addition, the efficiency of the heart as a pump decreases significantly due to infarct wall thinning and LV dilation as a result of increased strains in the infarct region. Even small reductions in ventricular wall thickness indicate a poor prognosis and eventual HF. Therefore, infarct fibre strains should also be alleviated to prevent dilation and wall thinning. Fibre stress and fibre strain, therefore, were evaluated to determine the mechanical effects of simulated injected PEG hydrogel on the LV.

The inclusion of hydrogel layers caused a reduction in EDV in both the acute and fibrotic infarct models. Although LV dilation at ED was reduced in the acute infarct model, the addition of hydrogel caused a significantly lower EDV, below that recorded in the healthy model. Therefore, there was neither an advantage nor disadvantage on EDV due to hydrogel injection. There was no improvement in contractility of the LV due to the layered and bulk injected hydrogel. Ejection fraction (EF) was reduced by the introduction of both the acute and fibrotic infarcts into the LV model. The addition of hydrogel caused a slight increase in EF in the acute model which is most likely attributed to the increase in wall thickness and subsequent decrease in LV cavity volume. There was no positive effect on EF with the inclusion of hydrogel layers in the fibrotic model. Therefore, from analysis of the cardiac functional parameters alone, it is not clear that PEG injection has a beneficial effect on cardiac function.

However, looking at fibre stress and fibre strain in the various regions of the LV at both ED and ES time points, a clearer effect can be noticed. Inclusion of hydrogel caused a reduction in infarct and BZ myofibre stress in the acute and fibrotic infarct models at both ED and ES time points. This reduction in elevated myofibre stress could possibly prevent hypertrophy of the BZ and remote tissue. Reduced ES infarct fibre stress, resulting from hydrogel injection, can limit the possibility of infarct rupture. As well, hydrogel injection reduced ED and ES infarct and BZ fibre strain in the acute and fibrotic infarct models, which could signify a reduction in stretching of the myocardium

which leads to wall thinning and dilation of the LV. ES fibre strain was greatly reduced in the BZ region and mean ES LV fibre strain also improved. Hydrogel injection therefore, has the ability to reduce LV wall thinning and dilation as well as elevated myofibre stresses. In general, the developed models helped explore the mechanics behind biomaterial injection therapy. The results of this research provide a framework for future computational studies addressing some of the limitations addressed previously.

References

AGUADO-SIERRA, J., KRISHNAMURTHY, A., VILLONGCO, C., CHUANG, J., HOWARD, E., GONZALES, M. J., OMENS, J., KRUMMEN, D. E., NARAYAN, S. & KERCKHOFFS, R. C. P. 2011. Patient-specific modeling of dyssynchronous heart failure: a case study. *Progress in Biophysics and Molecular Biology,* 107**,** 147.

AHA 2008. Heart Disease and Stroke statistics: Our guide to current statistics and the supplement to our Heart and Stroke Facts. Dallas: American Heart Association.

ANTMAN, E., BASSAND, J., KLEIN, W., OHMAN, M., LOPEZ SENDON, J., RYDEN, L., SIMOONS, M. & TENDERA, M. 2000. Myocardial infarction redefined--a consensus document of The Joint European Society of Cardiology/American College of Cardiology committee for the redefinition of myocardial infarction: The Joint European Society of Cardiology/American College of Cardiology Committee. *Journal of the American College of Cardiology,* 36**,** 959.

ARTS, T., BOVENDEERD, P., DELHAAS, T. & PRINZEN, F. 2003. Modeling the relation between cardiac pump function and myofiber mechanics. *Journal of Biomechanics,* 36**,** 731-736.

ARTS, T., RENEMAN, R. & VEENSTRA, P. 1979. A model of the mechanics of the left ventricle. *Annals of Biomedical Engineering,* 7**,** 299-318.

ARTS, T., VEENSTRA, P. & RENEMAN, R. 1982. Epicardial deformation and left ventricular wall mechanisms during ejection in the dog. *American Journal of Physiology- Heart and Circulatory Physiology,* 243**,** H379.

AURIGEMMA, G., SILVER, K., PRIEST, M. & GAASCH, W. 1995. Geometric changes allow normal ejection fraction despite depressed myocardial shortening in hypertensive left ventricular hypertrophy. *Journal of the American College of Cardiology,* 26**,** 195-202.

BELIK, M. E., USYK, T. P. & MCCULLOCH, A. D. 2004. Computational methods for cardiac electrophysiology. *In:* AYACHE, N. (ed.) *Computational Models for the Human Body.* Elsevier B.V.

BEYAR, R. & SIDEMAN, S. 1984. A computer study of the left ventricular performance based on fiber structure, sarcomere dynamics, and transmural electrical propagation velocity. *Circulation Research,* 55**,** 358.

BOGEN, D. K., RABINOWITZ, S. A., NEEDLEMAN, A., MCMAHON, T. A. & ABELMANN, W. H. 1980. An analysis of the mechanical disadvantage of myocardial infarction in the canine left ventricle. *Circ Res,* 47**,** 728-41.

BOVENDEERD, P. 2008. Modeling Cardiac Function - 8W160. Eindhoven: University of Technology.

BURKHOFF, D., MIRSKY, I. & SUGA, H. 2005. Assessment of systolic and diastolic ventricular properties via pressure- volume analysis: a guide for clinical, translational, and basic researchers. *American Journal of Physiology: Heart & Circulatory Physiology,* 58**,** H501-H512.

BURTON, R. A. B., PLANK, G., SCHNEIDER, J. E., GRAU, V., AHAMMER, H., KEELING, S. L., LEE, J., SMITH, N. P., GAVAGHAN, D., TRAYANOVA, N. & KOHL, P. 2006. Three-Dimensional Models of Individual Cardiac Histoanatomy: Tools and Challenges. *Annals of the New York Academy of Sciences,* 1080**,** 301-319.

CHEN, J., SONG, S. K., LIU, W., MCLEAN, M., ALLEN, J. S., TAN, J., WICKLINE, S. A. & YU, X. 2003. Remodeling of cardiac fiber structure after infarction in rats quantified with diffusion tensor MRI. *American Journal of Physiology-Heart and Circulatory Physiology,* 285**,** H946.

CHRISTMAN, K. L. & LEE, R. J. 2006. Biomaterials for the treatment of myocardial infarction. *J Am Coll Cardiol,* 48**,** 907-13.

CHRISTMAN, K. L., VARDANIAN, A. J., FANG, Q., SIEVERS, R. E., FOK, H. H. & LEE, R. J. 2004. Injectable fibrin scaffold improves cell transplant survival, reduces infarct expansion, and induces neovasculature formation in ischemic myocardium. *J Am Coll Cardiol,* 44**,** 654-60.

COHN, J. N., FERRARI, R. & SHARPE, N. 2000. Cardiac remodeling--concepts and clinical implications: a consensus paper from an international forum on cardiac remodeling. *Journal of the American College of Cardiology,* 35**,** 569-582.

COHN, J. N. & TOGNONI, G. 2001. A randomized trial of the angiotensin-receptor blocker valsartan in chronic heart failure. *N Engl J Med,* 345**,** 1667-75.

CORCAP CorCap™ Cardiac Support Device Patient Information Booklet. *In:* FDA (ed.).

COSTA, K. D., HOLMES, J. W. & MCCULLOCH, A. D. 2001. Modelling cardiac mechanical properties in three dimensions. *Royal Society of London Philosophical Transactions Series A,* 359**,** 1233-1250.

COSTA, K. D., HUNTER, P. J., ROGERS, J. M., GUCCIONE, J. M., WALDMAN, L. K. & MCCULLOCH, A. D. 1996. A three-dimensional finite element method for large elastic deformations of ventricular myocardium: I--Cylindrical and spherical polar coordinates. *J Biomech Eng,* 118**,** 452-63.

COURANT, R. 1943. Variational methods for the solution of problems of equilibrium and vibrations. *LECTURE NOTES IN PURE AND APPLIED MATHEMATICS***,** 1-1.

DAI, W., WOLD, L. E., DOW, J. S. & KLONER, R. A. 2005. Thickening of the infarcted wall by collagen injection improves left ventricular function in rats: a novel approach to preserve cardiac function after myocardial infarction. *J Am Coll Cardiol,* 46**,** 714-9.

DAVIS, M. E., HSIEH, P. C. H., GRODZINSKY, A. J. & LEE, R. T. 2005. Custom Design of the Cardiac Microenvironment With Biomaterials. *Circ Res,* 97**,** 8-15.

DEMER, L. L. & YIN, F. 1983. Passive biaxial mechanical properties of isolated canine myocardium. *The Journal of physiology,* 339**,** 615.

DOBNER, S., BEZUIDENHOUT, D., GOVENDER, P., ZILLA, P. & DAVIES, N. 2009. A Synthetic Non-degradable Polyethylene Glycol Hydrogel Retards Adverse Post-infarct Left Ventricular Remodeling. *Journal of Cardiac Failure,* 15**,** 629-636.

DOKOS, S., SMAILL, B. H., YOUNG, A. A. & LEGRICE, I. J. 2002. Shear properties of passive ventricular myocardium. *American Journal of Physiology-Heart and Circulatory Physiology,* 283**,** H2650.

DOLL, S. & SCHWEIZERHOF, K. 2000. On the development of volumetric strain energy functions. *Journal of applied mechanics,* 67**,** 17.

FISHBEIN, M. C., MACLEAN, D. & MAROKO, P. R. 1978. The histopathologic evolution of myocardial infarction. *Chest,* 73**,** 843-849.

FITZHUGH, R. 1961. Impulses and Physiological States in Theoretical Models of Nerve Membrane. *Biophysical Journal,* 1**,** 445.

FLATHER, M. D., YUSUF, S., KØBER, L., PFEFFER, M., HALL, A., MURRAY, G., TORP-PEDERSEN, C., BALL, S., POGUE, J., MOYÉ, L. & BRAUNWALD, E. 2000. Long-term ACE-inhibitor therapy in patients with heart failure or left-ventricular dysfunction: a systematic overview of data from individual patients. *The Lancet,* 355**,** 1575-1581.

FOGEL, M. A., WEINBERG, P. M., FELLOWS, K. E. & HOFFMAN, E. A. 1995. A Study in Ventricular–Ventricular Interaction : Single Right Ventricles Compared With Systemic Right Ventricles in a Dual-Chamber Circulation. *Circulation,* 92**,** 219-230.

FOMOVSKY, G. & HOLMES, J. 2010. Evolution of scar structure, mechanics, and ventricular function after myocardial infarction in the rat. *American Journal of Physiology- Heart and Circulatory Physiology,* 298**,** H221.

FRANGI 2001. Three-Dimensional Modeling for Functional Analysis of Cardiac Images: A Review. *IEEE Transactions on Medical Imaging,* 20**,** 24.

FUCHS, S., BAFFOUR, R., ZHOU, Y. F., SHOU, M., PIERRE, A., TIO, F. O., WEISSMAN, N. J., LEON, M. B., EPSTEIN, S. E. & KORNOWSKI, R. 2001. Transendocardial delivery of autologous bone marrow enhances collateral perfusion and regional function in pigs with chronic experimental myocardial ischemia. *Journal of the American College of Cardiology,* 37**,** 1726-32.

GONZÁLEZ BALLESTER, M. Á., ZISSERMAN, A. P. & BRADY, M. 2002. Estimation of the partial volume effect in MRI. *Medical Image Analysis,* 6**,** 389.

GOTTLIEB, S., MCCARTER, R. & VOGEL, R. 1998. Effect of beta-blockade on mortality among high-risk and low-risk patients after myocardial infarction. *New England Journal of Medicine,* 339**,** 489.

GROSSMAN, W., JONES, D. & MCLAURIN, L. P. 1975. Wall stress and patterns of hypertrophy in the human left ventricle. *J Clin Invest,* 56**,** 56-64.

GUCCIONE, J., MCCULLOCH, A. & WALDMAN, L. 1991. Passive material properties of intact ventricular myocardium determined from a cylindrical model. *Journal of biomechanical engineering,* 113**,** 42.

GUCCIONE, J., MOONLY, S., MOUSTAKIDIS, P., COSTA, K., MOULTON, M., RATCLIFFE, M. & PASQUE, M. 2001. Mechanism underlying mechanical dysfunction in the border zone of left ventricular aneurysm: a finite element model study. *The Annals of thoracic surgery,* 71**,** 654-662.

GUCCIONE, J. M., COSTA, K. D. & MCCULLOCH, A. D. 1995. Finite element stress analysis of left ventricular mechanics in the beating dog heart. *J Biomech,* 28**,** 1167-77.

GUCCIONE, J. M. & MCCULLOCH, A. D. 1993. Mechanics of active contraction in cardiac muscle: Part I--Constitutive relations for fiber stress that describe deactivation. *J Biomech Eng,* 115**,** 72-81.

GUCCIONE, J. M., WALDMAN, L. K. & MCCULLOCH, A. D. 1993. Mechanics of Active Contraction in Cardiac-Muscle .2. Cylindrical Models of the Systolic Left-Ventricle. *Journal of Biomechanical Engineering-Transactions of the Asme,* 115**,** 82-90.

GUPTA, K. B., RATCLIFFE, M. B., FALLERT, M. A., EDMUNDS, L. H., JR. & BOGEN, D. K. 1994. Changes in passive mechanical stiffness of myocardial tissue with aneurysm formation. *Circulation,* 89**,** 2315-2326.

HALL, S. A., CIGARROA, C. G., MARCOUX, L., RISSER, R. C., GRAYBURN, P. A. & EICHHORN, E. J. 1995. Time course of improvement in left ventricular function, mass and geometry in patients with congestive heart failure treated with beta-adrenergic blockade. *J Am Coll Cardiol,* 25**,** 1154-61.

HEIBERG, E., ENGBLOM, H., ENGVALL, J., HEDSTRÖM, E., UGANDER, M. & ARHEDEN, H. 2005a. Semi-automatic quantification of myocardial infarction from delayed contrast enhanced magnetic resonance imaging. *Scandinavian Cardiovascular Journal,* 39**,** 267-275.

HEIBERG, E., UGANDER, M., ENGBLOM, H., GÖTBERG, M., OLIVECRONA, G. K., ERLINGE, D. & ARHEDEN, H. 2008. Automated quantification of myocardial infarction from MR images by accounting for partial volume effects: animal, phantom, and human study. *Radiology,* 246**,** 581-588.

HEIBERG, E., WIGSTRÖM, L., CARLSSON, M., BOLGER, A. & KARLSSON, M. 2005b. Time resolved three-dimensional automated segmentation of the left ventricle.

HIRAI, T., SASAYAMA, S., KAWASAKI, T. & YAGI, S. 1989. Stiffness of systemic arteries in patients with myocardial infarction. A noninvasive method to predict severity of coronary atherosclerosis [published erratum appears in Circulation 1989 Dec; 80 (6): 1946]. *Circulation,* 80**,** 78-86.

HODGKIN, A. & HUXLEY, A. 1990. A quantitative description of membrane current and its application to conduction and excitation in nerve. *Bulletin of Mathematical Biology,* 52**,** 25-71.

HOLMES, J. W., BORG, T. K. & COVELL, J. W. 2005. STRUCTURE AND MECHANICS OF HEALING MYOCARDIAL INFARCTS. *Annual Review of Biomedical Engineering,* 7**,** 223-253.

HOLZAPFEL, G. A. & OGDEN, R. W. 2009. Constitutive modelling of passive myocardium: a structurally based framework for material characterization. *Philosophical Transactions of the Royal Society A: Mathematical, Physical and Engineering Sciences,* 367**,** 3445-3475.

HONG, C., BECKER, C. R., HUBER, A., SCHOEPF, U. J., OHNESORGE, B., KNEZ, A., BRÜNING, R. & REISER, M. F. 2001. ECG-gated reconstructed multi-detector row CT coronary angiography: effect of varying trigger delay on image quality. *Radiology,* 220**,** 712-717.

HUMPHREY, J. D., STRUMPF, R. K. & YIN, F. C. 1990. Determination of a constitutive relation for passive myocardium: I. A new functional form. *J Biomech Eng,* 112**,** 333-9.

HUNTER, P., NIELSEN, P., SMAILL, B., LEGRICE, I. & HUNTER, I. 1992. An anatomical heart model with applications to myocardial activation and ventricular mechanics. *Critical reviews in biomedical engineering,* 20**,** 403.

HUNTER, P. J., MCCULLOCH, A. D. & TER KEURS, H. E. 1998. Modelling the mechanical properties of cardiac muscle. *Prog Biophys Mol Biol,* 69**,** 289-331.

JAIN, M., DERSIMONIAN, H., BRENNER, D., NGOY, S., TELLER, P., EDGE, A., ZAWADZKA, A., WETZEL, K., SAWYER, D. & COLUCCI, W. 2001. Cell therapy attenuates deleterious ventricular remodeling and improves cardiac performance after myocardial infarction. *Circulation,* 103**,** 1920.

JANSSENS, S., DUBOIS, C., BOGAERT, J., THEUNISSEN, K., DEROOSE, C., DESMET, W., KALANTZI, M., HERBOTS, L., SINNAEVE, P., DENS, J., MAERTENS, J., RADEMAKERS, F., DYMARKOWSKI, S., GHEYSENS, O., VAN CLEEMPUT, J., BORMANS, G., NUYTS, J., BELMANS, A., MORTELMANS, L., BOOGAERTS, M. & VAN DE WERF, F. 2006. Autologous bone marrow-derived stem-cell transfer in patients with ST-segment elevation myocardial infarction: double-blind, randomised controlled trial. *The Lancet,* 367**,** 113-121.

JOHNSON, T. R. C., NIKOLAOU, K., WINTERSPERGER, B. J., LEBER, A. W., VON ZIEGLER, F., RIST, C., BUHMANN, S., KNEZ, A., REISER, M. F. & BECKER, C. R. 2006. Dual-source CT cardiac imaging: initial experience. *European Radiology,* 16**,** 1409-1415.

KADNER, K., DOBNER, S., FRANZ, T., BEZUIDENHOUT, D., SIRRY, M. S., ZILLA, P. & DAVIES, N. H. 2012. The beneficial effects of deferred delivery on the efficiency of hydrogel therapy post myocardial infarction. *Biomaterials,* 33**,** 2060-2066.

KAUS, M. R., BERG, J. V., WEESE, J., NIESSEN, W. & PEKAR, V. 2004. Automated segmentation of the left ventricle in cardiac MRI. *Medical Image Analysis,* 8**,** 245-254.

KELLY, R., TING, C., YANG, T., LIU, C., MAUGHAN, W., CHANG, M. & KASS, D. 1992. Effective arterial elastance as index of arterial vascular load in humans. *Circulation,* 86**,** 513-521.

KERCKHOFFS, R., MCCULLOCH, A., OMENS, J. & MULLIGAN, L. 2009. Effects of biventricular pacing and scar size in a computational model of the failing heart with left bundle branch block. *Medical Image Analysis,* 13**,** 362.

KERCKHOFFS, R., NEAL, M., GU, Q., BASSINGTHWAIGHTE, J., OMENS, J. & MCCULLOCH, A. 2007. Coupling of a 3D Finite Element Model of Cardiac Ventricular Mechanics to Lumped Systems Models of the Systemic and Pulmonic Circulation. *Annals of Biomedical Engineering,* 35**,** 1-18.

KERCKHOFFS, R. C. P., HEALY, S. N., USYK, T. P. & MCCULLOCH, A. D. 2006. Computational methods for cardiac electromechanics. *Proceedings of the IEEE,* 94**,** 769-783.

KOBER, L., TORP-PEDERSEN, C., CARLSEN, J. E., BAGGER, H., ELIASEN, P., LYNGBORG, K., VIDEBAEK, J., COLE, D. S., AUCLERT, L. & PAULY, N. C. 1995. A clinical trial of the angiotensin-converting-enzyme inhibitor trandolapril in patients with left ventricular dysfunction after myocardial infarction. Trandolapril Cardiac Evaluation (TRACE) Study Group. *N Engl J Med,* 333**,** 1670-6.

KOFIDIS, T., LEBL, D. R., MARTINEZ, E. C., HOYT, G., TANAKA, M. & ROBBINS, R. C. 2005. Novel injectable bioartificial tissue facilitates targeted, less invasive, large-scale tissue restoration on the beating heart after myocardial injury. *Circulation,* 112**,** I173-7.

KONSTAM, M. A. 2005. Reliability of Ventricular Remodeling as a Surrogate for Use in Conjunction With Clinical Outcomes in Heart Failure. *American Journal of Cardiology*.

KORTSMIT, J., DAVIES, N. H., MILLER, R., MACADANGDANG, J. R., ZILLA, P. & FRANZ, T. 2012a. The effect of hydrogel injection on cardiac function and myocardial mechanics in a computational post-infarction model.

KORTSMIT, J., DAVIES, N. H., MILLER, R., ZILLA, P. & FRANZ, T. 2012b. The Mechanical Effects of Layered and Bulk Hydrogel Injectates in the Cardiac Left Ventricle at Early and Late Post-Infarction Stages: A Computational Study. *Journal of Cardiac Failure*.

KRAEHENBUEHL, T. P., ZAMMARETTI, P., VAN DER VLIES, A. J., SCHOENMAKERS, R. G., LUTOLF, M. P., JACONI, M. E. & HUBBELL, J. A. 2008. Three-dimensional extracellular matrix-directed cardioprogenitor differentiation: Systematic modulation of a synthetic cell-responsive PEG-hydrogel. *Biomaterials,* 29**,** 2757-2766.

LAFLAMME, M. A., CHEN, K. Y., NAUMOVA, A. V., MUSKHELI, V., FUGATE, J. A., DUPRAS, S. K., REINECKE, H., XU, C., HASSANIPOUR, M. & POLICE, S. 2007. Cardiomyocytes derived from human embryonic stem cells in pro-survival factors enhance function of infarcted rat hearts. *Nature biotechnology,* 25**,** 1015-1024.

LANDA, N., MILLER, L., FEINBERG, M. S., HOLBOVA, R., SHACHAR, M., FREEMAN, I., COHEN, S. & LEOR, J. 2008. Effect of injectable alginate implant on cardiac remodeling and function after recent and old infarcts in rat. *Circulation,* 117**,** 1388-96.

LARGE, S. 2007. Surgery for heart failure. *Heart,* 93**,** 392-402.

LIN, C. C. & ANSETH, K. S. 2009. PEG hydrogels for the controlled release of biomolecules in regenerative medicine. *Pharmaceutical research,* 26**,** 631-643.

LIU, C., HOFSTETTER, G. & MANG, H. 1994. 3D finite element analysis of rubber-like materials at finite strains. *Engineering computations,* 11**,** 111-128.

LLOYD-JONES, D., ADAMS, R. J., BROWN, T. M., CARNETHON, M., DAI, S., DE SIMONE, G., FERGUSON, T. B., FORD, E., FURIE, K., GILLESPIE, C., GO, A., GREENLUND, K., HAASE, N., HAILPERN, S., HO, P. M., HOWARD, V., KISSELA, B., KITTNER, S., LACKLAND, D., LISABETH, L., MARELLI, A., MCDERMOTT, M. M., MEIGS, J., MOZAFFARIAN, D., MUSSOLINO, M., NICHOL, G., ROGER, V. R. L., ROSAMOND, W., SACCO, R., SORLIE, P., THOM, T., WASSERTHIEL-SMOLLER, S., WONG, N. D. & WYLIE-ROSETT, J. 2010. Heart disease and stroke statistics--2010 update: a report from the American Heart Association. *Circulation,* 121**,** e46-e215.

LORENZ, C. H., WALKER, E. S., MORGAN, V. L., KLEIN, S. S. & GRAHAM, T. P. 1999. Normal Human Right and Left Ventricular Mass, Systolic Function, and Gender Differences by Cine Magnetic Resonance Imaging. *Journal of Cardiovascular Magnetic Resonance,* 1**,** 7-21.

MANGI, A. A., NOISEUX, N., KONG, D., HE, H., REZVANI, M., INGWALL, J. S. & DZAU, V. J. 2003. Mesenchymal stem cells modified with Akt prevent remodeling and restore performance of infarcted hearts. *Nat Med,* 9**,** 1195-201.

MARCHESSEAU, S., HEIMANN, T., CHATELIN, S., WILLINGER, R. & DELINGETTE, H. 2010. Multiplicative Jacobian Energy Decomposition Method for Fast Porous Visco-Hyperelastic Soft Tissue Model.

MAZHARI 1998. Regional Myocardial Perfusion and Mechanics: A Model-Based Method of Analysis. *Annals of Biomedical Engineering,* 26**,** 13.

MCCARTHY, P. M., TAKAGAKI, M., OCHIAI, Y., YOUNG, J. B., TABATA, T., SHIOTA, T., QIN, J. X., THOMAS, J. D., MORTIER, T. J., SCHROEDER, R. F., SCHWEICH, C. J., JR. & FUKAMACHI, K. 2001. Device-based change in left ventricular shape: a new concept for the treatment of dilated cardiomyopathy. *The Journal of Thoracic and Cardiovascular Surgery,* 122**,** 482-490.

MCCULLOCH, A. D. 2005. Cardiac Biomechanics. *In:* BRONZINO, J. D. (ed.) *The Biomedical Engineering Handbook.* 3rd Edition ed. Boca Raton, FL: CRC Press.

MCMURRAY, J. J., OSTERGREN, J., SWEDBERG, K., GRANGER, C. B., HELD, P., MICHELSON, E. L., OLOFSSON, B., YUSUF, S. & PFEFFER, M. A. 2003. Effects of candesartan in patients with chronic heart failure and reduced left-ventricular systolic function taking angiotensin-converting-enzyme inhibitors: the CHARM-Added trial. *Lancet,* 362**,** 767-71.

MEDICINENET. 2004. Available: medicinenet.com.

MIURA, T. & MIKI, T. 2008. Limitation of myocardial infarct size in the clinical setting: current status and challenges in translating animal experiments into clinical therapy. *Basic Research in Cardiology,* 103**,** 501-513.

NAGUMO, J., ARIMOTO, S. & YOSHIZAWA, S. 1962. An Active Pulse Transmission Line Simulating Nerve Axon. *Proceedings of the IRE,* 50**,** 2061-2070.

NAGY, V. 2001. [Left ventricular hypertrophy: pathogenesis, diagnosis and therapy]. *Orvosi Hetilap,* 142**,** 1375-1383.

NELSON, D. M., MA, Z., FUJIMOTO, K. L., HASHIZUME, R. & WAGNER, W. R. 2011. Intra-myocardial biomaterial injection therapy in the treatment of heart failure: Materials, outcomes and challenges. *Acta biomaterialia,* 7**,** 1-15.

NEVO, E. & LANIR, Y. 1989. Structural finite deformation model of the left ventricle during diastole and systole. *J Biomech Eng,* 111**,** 342-9.

NICKERSON, D., SMITH, N. & HUNTER, P. 2005. New developments in a strongly coupled cardiac electromechanical model. *Europace,* 7**,** S118-S127.

NIELSEN, P. M., LE GRICE, I. J., SMAILL, B. H. & HUNTER, P. J. 1991. Mathematical model of geometry and fibrous structure of the heart. *Am J Physiol Heart Circ Physiol,* 260**,** H1365-1378.

NOBLE, D. & RUDY, Y. 2001. Models of cardiac ventricular action potentials: iterative interaction between experiment and simulation. *Philosophical Transactions of the Royal Society A: Mathematical, Physical and Engineering Sciences,* 359**,** 1127-1142.

OHNESORGE, B., FLOHR, T., BECKER, C., KOPP, A. F., SCHOEPF, U. J., BAUM, U., KNEZ, A., KLINGENBECK-REGN, K. & REISER, M. F. 2000. Cardiac imaging by means of electrocardiographically gated multisection spiral CT: initial experience. *Radiology,* 217**,** 564-571.

OKADA, M., PAYNE, T. R., OSHIMA, H., MOMOI, N., TOBITA, K. & HUARD, J. 2010. Differential efficacy of gels derived from small intestinal submucosa as an injectable biomaterial for myocardial infarct repair. *Biomaterials,* 31**,** 7678-7683.

OMENS, J., MAY, K. & MCCULLOCH, A. 1991. Transmural distribution of three-dimensional strain in the isolated arrested canine left ventricle. *American Journal of Physiology- Heart and Circulatory Physiology,* 261**,** H918.

OPIE, L. H., COMMERFORD, P. J., GERSH, B. J. & PFEFFER, M. A. 2006. Controversies in ventricular remodelling. *Lancet,* 367**,** 356-67.

PARAGIOS, N. 2003. A level set approach for shape-driven segmentation and tracking of the left ventricle. *IEEE Transactions on Medical Imaging,* 22**,** 773-776.

PATTEN, R. D. & HALL-PORTER, M. R. 2009. Small Animal Models of Heart Failure. *Circulation: Heart Failure,* 2**,** 138-144.

PFEFFER, M. A. & BRAUNWALD, E. 1990. Ventricular remodeling after myocardial infarction. Experimental observations and clinical implications. *Circulation,* 81**,** 1161-72.

PFEFFER, M. A., BRAUNWALD, E., MOYE, L. A., BASTA, L., BROWN, E. J., JR., CUDDY, T. E., DAVIS, B. R., GELTMAN, E. M., GOLDMAN, S., FLAKER, G. C. & ET AL. 1992. Effect of captopril on mortality and morbidity in patients with left ventricular dysfunction after myocardial infarction. Results of the survival and ventricular enlargement trial. The SAVE Investigators. *N Engl J Med,* 327**,** 669-77.

POTHINENI, K. R., INAMDAR, V., MILLER, A. P., NANDA, N. C., BANDARUPALLI, N., CHAURASIA, P., KIRKLIN, J. K., MCGIFFIN, D. C. & PAJARO, O. E. 2007. Initial Experience with Live/Real Time Three-Dimensional Transesophageal Echocardiography. *Echocardiography,* 24**,** 1099-1104.

RATCLIFFE, M. B., HONG, J., SALAHIEH, A., RUCH, S. & WALLACE, A. W. 1998. The effect of ventricular volume reduction surgery in the dilated, poorly contractile left ventricle: A simple finite element analysis. *The Journal of Thoracic and Cardiovascular Surgery,* 116**,** 566-577.

ROCHA, R. & STIER, C. T. 2001. Pathophysiological effects of aldosterone in cardiovascular tissues. *Trends in Endocrinology and Metabolism,* 12**,** 308-314.

ROHMER, D., SITEK, A. & GULLBERG, G. T. 2007. Reconstruction and visualization of fiber and laminar structure in the normal human heart from ex vivo diffusion tensor magnetic resonance imaging (DTMRI) data. *Investigative radiology,* 42**,** 777.

SABBAH, H. N. 2003. The cardiac support device and the Myosplint: treating heart failure by targeting left ventricular size and shape. *The Annals of thoracic surgery,* 75**,** S13-S19.

SANTAMORE, W. P., CONSTANTINESCU, M., VINTEN-JOHANSEN, J., JOHNSTON, W. E. & LITTLE, W. C. 1988. Alterations in left ventricular compliance due to changes in right ventricular volume, pressure and compliance. *Cardiovascular Research,* 22**,** 768-776.

SCHLOSSER, T., PAGONIDIS, K., HERBORN, C. U., HUNOLD, P., WALTERING, K.-U., LAUENSTEIN, T. C. & BARKHAUSEN, J. 2005. Assessment of Left Ventricular Parameters Using 16-MDCT and New Software for Endocardial and Epicardial Border Delineation. *Am. J. Roentgenol.,* 184**,** 765-773.

SERMESANT, M. & RAZAVI, R. 2010. Personalized Computational Models of the Heart for Cardiac Resynchronization Therapy. *Patient-Specific Modeling of the Cardiovascular System***,** 167-182.

STERGIOPULOS, N., WESTERHOF, B. E. & WESTERHOF, N. 1999. Total arterial inertance as the fourth element of the windkessel model. *Am J Physiol,* 276**,** H81-8.

STREETER JR, D., SPOTNITZ, H., PATEL, D., ROSS JR, J. & SONNENBLICK, E. 1969. Fiber orientation in the canine left ventricle during diastole and systole. *Circulation Research,* 24**,** 339.

SUGA, H. 1990. Energetics of the time-varying elastance model, a visco-elastic model, matches Mommaerts' unifying concept of the Fenn effect of muscle. *Jpn Heart J,* 31**,** 341-53.

SUGA, H. & SAGAWA, K. 1974. Instantaneous pressure-volume relationships and their ratio in the excised, supported canine left ventricle. *Circulation Research,* 35**,** 117-126.

SUN, K., STANDER, N., JHUN, C., ZHANG, Z., SUZUKI, T., WANG, G., SAEED, M., WALLACE, A., TSENG, E. & BAKER, A. 2009. A computationally efficient formal optimization of regional myocardial contractility in a sheep with left ventricular aneurysm. *Journal of biomechanical engineering,* 131**,** 111001.

TAKAGAKI, M., MCCARTHY, P., OCHIAI, Y., DESSOFFY, R., DOI, K., VIDLUND, R., MORTIER, T., SCHWEICH JR, C. & FUKAMACHI, K. 2001. Novel device to change left ventricular shape for heart failure treatment: device design and implantation procedure. *ASAIO journal,* 47**,** 244.

TER KEURS, H. 1983. Calcium and contractility. *Cardiac Metabolism, New York: Wiley***,** 73-99.

TER KEURS, H., RIJNSBURGER, W., VAN HEUNINGEN, R. & NAGELSMIT, M. 1980. Tension development and sarcomere length in rat cardiac trabeculae. Evidence of length-dependent activation. *Circulation Research,* 46**,** 703.

USYK 2002. Computational Methods for Soft Tissue Biomechanics. 84.

USYK, T. P. & MCCULLOCH, A. D. 2003. Computational methods for soft tissue biomechanics. *In:* HOLZAPFEL, G. A. & OGDEN, R. W. (eds.) *Biomechanics of Soft Tissue in Cardiovascular Systems.* Wien: Springer.

VAN DER HORST, I., VOORS, A. & VAN VELDHUISEN, D. 2007. Treatment of heart failure with ACE inhibitors and beta-blockers. *Clinical research in cardiology,* 96**,** 193-195.

VETTER, F. & MCCULLOCH, A. 2000a. Three-dimensional stress and strain in passive rabbit left ventricle: a model study. *Annals of Biomedical Engineering,* 28**,** 781-792.

VETTER, F. J. & MCCULLOCH, A. D. 1998. Three-dimensional analysis of regional cardiac function:a model of rabbit ventricular anatomy. *Progress in Biophysics and Molecular Biology,* 69**,** 27.

VETTER, F. J. & MCCULLOCH, A. D. 2000b. Three-Dimensional Stress and Strain in Passive Rabbit Left Ventricle: A Model Study. *Annals of Biomedical Engineering,* 28**,** 12.

WALKER, J., RATCLIFFE, M., ZHANG, P., WALLACE, A., HSU, E., SALONER, D. & GUCCIONE, J. 2008. Magnetic resonance imaging-based finite element stress analysis after linear repair of left ventricular aneurysm. *The Journal of Thoracic and Cardiovascular Surgery,* 135**,** 1094-1102.

WALKER, J. C., RATCLIFFE, M. B., ZHANG, P., WALLACE, A. W., FATA, B., HSU, E. W., SALONER, D. & GUCCIONE, J. M. 2005. MRI-based finite-element analysis of left ventricular aneurysm. *Am J Physiol Heart Circ Physiol,* 289**,** H692-700.

WALL, S. T., WALKER, J. C., HEALY, K. E., RATCLIFFE, M. B. & GUCCIONE, J. M. 2006. Theoretical impact of the injection of material into the myocardium - A finite element model simulation. *Circulation,* 114**,** 2627-2635.

WATANABE, H., SUGIURA, S., KAFUKU, H. & HISADA, T. 2004. Multiphysics Simulation of Left Ventricular Filling Dynamics Using Fluid-Structure Interaction Finite Element Method. *Biophys. J.,* 87**,** 2074-2085.

WEISS, J. A., MAKER, B. N. & GOVINDJEE, S. 1996. Finite element implementation of incompressible, transversely isotropic hyperelasticity. *Computer Methods in Applied Mechanics and Engineering,* 135**,** 107-128.

WENK, J., SUN, K., ZHANG, Z., SOLEIMANI, M., GE, L., SALONER, D., WALLACE, A., RATCLIFFE, M. & GUCCIONE, J. 2011a. Regional left ventricular myocardial contractility and stress in a finite element model of posterobasal myocardial infarction. *Journal of biomechanical engineering,* 133**,** 044501.

WENK, J., WALL, S., PETERSON, R., HELGERSON, S., SABBAH, H., BURGER, M., STANDER, N., RATCLIFFE, M. & GUCCIONE, J. 2009. A method for automatically optimizing medical devices for treating heart failure: designing polymeric injection patterns. *Journal of biomechanical engineering,* 131**,** 121011.

WENK, J., ZHANG, Z., CHENG, G., MALHOTRA, D., ACEVEDO-BOLTON, G., BURGER, M., SUZUKI, T., SALONER, D., WALLACE, A. & GUCCIONE, J. 2010. First Finite Element Model of the Left Ventricle With Mitral Valve: Insights Into Ischemic Mitral Regurgitation. *The Annals of thoracic surgery,* 89**,** 1546-1553.

WENK, J. F., ESLAMI, P., ZHANG, Z., XU, C., KUHL, E., GORMAN III, J. H., ROBB, J. D., RATCLIFFE, M. B., GORMAN, R. C. & GUCCIONE, J. M. 2011b. A Novel Method for Quantifying the In-Vivo Mechanical Effect of Material Injected Into a Myocardial Infarction. *The Annals of thoracic surgery,* 92**,** 935-941.

WHELAN, R. S., MANI, K. & KITSIS, R. N. 2007. Nipping at cardiac remodeling. *J Clin Invest,* 117**,** 2751-3.

WHO 2008. WHO: The Atlas of Heart Disease and Stroke. Geneva: World Health Organization.

YIN, F., CHAN, C. & JUDD, R. M. 1996. Compressibility of perfused passive myocardium. *American Journal of Physiology-Heart and Circulatory Physiology,* 271**,** H1864-H1870.

YOO, T., ACKERMAN, M., LORENSEN, W., SCHROEDER, W., CHALANA, V., AYLWARD, S., METAXAS, D. & WHITAKER, R. 2002. Engineering and algorithm design for an image processing API: A technical report on ITK-the Insight Toolkit. *Studies in health technology and informatics***,** 586-592.

YU, J., CHRISTMAN, K. L., CHIN, E., SIEVERS, R. E., SAEED, M. & LEE, R. J. 2009. Restoration of left ventricular geometry and improvement of left ventricular function in a rodent model of chronic ischemic cardiomyopathy. *The Journal of Thoracic and Cardiovascular Surgery,* 137**,** 180-187.

YUSHKEVICH, P., PIVEN, J., CODY, H., HO, S., GEE, J. & GERIG, G. 2005. User-guided level set segmentation of anatomical structures with ITK-SNAP. *Insight Jounral,* 1.

ZISCH, A. H., LUTOLF, M. P. & HUBBELL, J. A. 2003. Biopolymeric delivery matrices for angiogenic growth factors. *Cardiovasc Pathol,* 12**,** 295-310.